MASTERARBEIT / MASTER'S THESIS

Titel der Masterarbeit / Title of the Master's Thesis

Light induced dipole-dipole interactions between optically levitated nanoparticles

verfasst von / submitted by

Livia Egyed, BSc

angestrebter akademischer Grad / in partial fulfilment of the requirements for the degree of

Master of Science (MSc)

Wien, 2022 / Vienna, 2022

Studienkennzahl lt. Studienblatt / degree programme code as it appears on the student record sheet:	UA 066 876
Studienrichtung lt. Studienblatt / degree programme as it appears on the student record sheet:	Masterstudium Physik
Betreut von / Supervisor:	Univ.-Prof. Dr. Markus Aspelmeyer
Mitbetreut von / Co-Supervisor:	Dr. Uroš Delić

Acknowledgments

There are many people involved in enabling me to complete this journey that has been my master thesis. First of all, I would like to thank my supervisor Markus Aspelmeyer for always being supportive and inspiring me and everyone else in the group. Having the possibility to be part of a group working on such a variety of fascinating topics together with so many amazing people has been a real privilege.

Secondly, I want to thank Uroš, for always supporting me and listening to all the big and small problems of everyday labwork. Thanks for always being up to share some your vast pool of knowledge.

A special thanks also goes to Nikolai Kiesel, who believed in me and gave me the opportunity to first join the group.

Also thanks to Mel and Anton for being such great lab partners and helping me keep my sanity while rebuilding the setup for the hundredth time. Thanks to Aisling, Iurie, Mel, Kahan and Ayub, who taught me almost everything I know about building an optical setup and are constantly open to talk about any of my questions or concerns. Thanks to the whole group and especially the cavity-crew for always being welcoming, eager to help, open minded and just fun to be around.

Finally, I would like to thank my family, my boyfriend and my friends for the infinite support I received from you, enabling me to follow this path and always having my back.

Abstract

Arrays of coupled mechanical oscillators are a promising field for studies of collective mechanical effects such as non-reciprocal phonon transport or the realization of multipartite entanglement. Using optically trapped particles in distinct tweezers allows for high force sensitivity due to their isolation from the environment as well as high tunability of the interacting system when using their dipole radiation as a mediator. We present a theoretical derivation of the optical interaction forces between two trapped nanoparticles in traps with individually tunable position, amplitude and phase. Furthermore, we present an experimental setup which allows for vast tunability of all the parameters in order to create and control multiparticle dynamics. Finally, we present first preliminary results that explore the theoretically derived effects.

Zusammenfassung

Matrizen aus gekoppelten, mechanischen Oszillatoren sind ein vielversprechendes Feld um kollektive mechanische Effekte wie nicht-reziproken Phononen-transport zu untersuchen oder die Verschränkung mehrerer Teilchen zu realisieren. Die Verwendung von optisch gefangenen Teilchen in unterschiedlichen Fallen ermöglicht eine hohe Sensibilität beim messen von Kräften aufgrund der starken Isolation von ihrer Umwelt sowie viel Freiheit in der Wahl der Parameter des interagierenden Systems, wenn ihre Dipol-Abstrahlung zum koppeln verwendet wird. Wir präsentieren eine theoretische Herleitung der Kraft zwischen zwei gefangenen Dipolen die optisch miteinander interagieren, wobei die Position, Amplitude und Phase der Fallen individuell variierbar ist. Des Weiteren präsentieren wir ein Experiment, das breite Veränderungen in allen Parametern erlaubt, sodass Mehrteilchen-Dynamiken erschaffen und kontrolliert werden können. Schlussendlich präsentieren wir erste, vorläufige Ergebnisse, die die theoretisch hergeleiteten Effekte überprüfen.

Contents

1 Introduction

In the last decades, the field of optomechanics, describing the interaction between light and matter, has opened the doors to a large variety of novel, groundbreaking experiments, enhancing our knowledge and understanding about the constituents of the world around us. Within these systems, levitated optomechanics has proven to be a good platform for testing quantum mechanical properties of nanometer sized objects, since they offer high quality factors due to their strong isolation from the environment [1–4]. While most of these experiments focus on single objects interacting with light via radiation pressure and gradient force [5], the study of many collective optomechanical effects requires control over multiple particles at once. Therefore, the prospect of expanding this system to multiple trapped particles, interacting not only with an optical field but also with each other, has recently gained increasing interest in the community [6–8].

One frequently studied interaction occurs due to the light scattered from an optically trapped micro- or nanometer sized particle onto its neighbours, effectively modifying the trapping field and creating an attractive or repulsive force, the so called *optical binding force*. When many particles are brought into vicinity of each other, this force can also cause them to self-assemble, creating sort of crystalline structures referred to as *optical matter* [9]. There has been extensive theoretical studies of the optical binding force of wavelength- and sub-wavelength sized objects [6, 7, 10]. However, experimental realizations of optical binding between particles in the Rayleigh-regime [10] have fallen short so far, since decreasing particle sizes increase the effects of thermal fluctuations and Brownian motion on the particles which makes it harder to obtain a stable system in which the optical binding force can be observed [11]. All optical binding studies using nanoparticles, with radii much smaller than the wavelength of the trapping beam, have so far been realised with metallic particles, making use of the surface plasmons in order to enhance the trapping stability and binding forces [12–14]. Additionally, studies of optical binding have so far been restricted to the case of equal phase of the two trapping beams (e.g. [6, 7]), covering only the special case of conservative, resonant interaction between the particles, thus failing to describe the full, non-conservative system dynamics.

In this thesis, the dynamics of two optically trapped nanoparticles in the Rayleigh-regime will be studied theoretically and experimentally. In the second Chapter, we start by giving an overview of the forces involved in optical trapping of single particles as well as the methods used to study their motion in the linear regime.

In the third Chapter, the study gets expanded onto two coupled particles. We first examine the general behaviour of two classical, conservatively coupled harmonic oscillators. Then we look deeper into different methods of coupling. First, we examine the role that charges on the particles play for the coupling as a function of distance between them, when no optical interaction is present. The main body, however, concentrates on the optical interaction between two levitated nanoparticles. We derive the force between two optically trapped particles with variable phases and distances between them in the dipole approximation and for the case of lateral binding, meaning that the particle connection axis is orthogonal to the optical axis, but include small fluctuations due to the particles oscillations in their traps. We simplify for the case of large distances between the particles with respect to the wavelength λ and investigate the resulting, non-reciprocal equations of motions for a variety of different relations between the conservative and non-conservative coupling rates.

Chapter four is dedicated to the experimental setup built within the scope of this thesis. The optical and electronics paths are discussed in detail, as well as the experimental methods used to calibrate and characterize the setup.

Finally, first results obtained on the setup are presented in Chapter five, where we reproduce both the conservative as well as the non-conservative coupled system dynamics experimentally that are predicted theoretically in this thesis.

2 Principles of optical tweezing

Optical tweezers are a powerful tool used to trap nano- or micrometer sized particles in air or liquid without mechanical contact. They have been invented and realized experimentally for the first time in the 70's by Arthur Ashkin [15, 16] who has discovered that microscopic dielectric particles can be three-dimensionally trapped by a tightly focused laser beam. Since then, they have been of great importance in many natural sciences, ranging from quantum optics to biophysics or cell biology, since optical tweezers are useful in a very versatile range of applications spanning from force sensing to the manipulation of molecules or investigating material properties [17–19].

In this work, optical tweezers will be used for trapping multiple nanoparticles since they both provide the tunability needed for this setup as well as an optical coupling mechanism between the particles through their coherently scattered dipole radiation, as will be explained in the following Chapter.

2.1 Gaussian beams

Optical tweezers typically consist of a focused Gaussian beam that form the trapping potential. The most important properties of focused Gaussian beams will thus be listed and discussed here.

We consider the three dimensional electric field of a linearly polarized Gaussian beam propagating in $+z$-direction with electric field amplitude $\boldsymbol{E}_0 = E_0\boldsymbol{e}_y$, polarized in y-direction and wavenumber $k = \frac{2\pi}{\lambda}$, where λ is the wavelength.

$$\boldsymbol{E}(x,y,z) = \boldsymbol{E}_0 \frac{w_0}{w(z)} e^{-\frac{x^2+y^2}{w^2(z)}} e^{i\left(kz-\eta(z)+k\frac{x^2+y^2}{2R(z)}\right)} \tag{1}$$

Here, the following abbreviations were used:

$$\text{beam waist:} \quad w(z) = w_0\sqrt{1+z^2/z_0^2} \quad \text{with} \quad w_0 \ldots \text{minimal beam waist} \tag{2}$$

$$\text{Rayleigh range:} \quad z_0 = \frac{kw_0^2}{2} \tag{3}$$

$$\text{Gouy phase shift:} \quad \eta(z) = \arctan\left(\frac{z}{z_0}\right) \tag{4}$$

$$\text{wavefront curvature:} \quad R(z) = z\left(1+\frac{z_0^2}{z^2}\right) \tag{5}$$

The Rayleigh range z_0 is defined as the distance from the focus of the beam (here at $z = 0$) at which the waist of the beam has increased to $\sqrt{2}w_0$. The beam waist is usually defined by the $1/e$ width, meaning the transverse position after which the beam has decreased to $1/e$ of its original value. In the focal spot the beam has its minimal waist w_0 [20].

The field intensity I is given by

$$I(x,y,z) = \frac{1}{2}c\varepsilon_0|\boldsymbol{E}|^2 = \frac{2P}{\pi w^2(z)} e^{-\frac{2(x^2+y^2)}{w^2(z)}}, \tag{6}$$

where $P = \pi w_0^2 \varepsilon_0 c|\boldsymbol{E_0}|^2/4$ is the optical power with c being the speed of light and ε_0 the vacuum permeability [21].

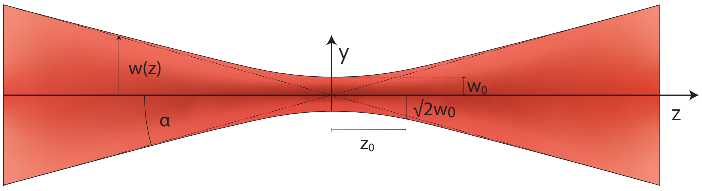

Figure 1: Sketch of a weakly focused Gaussian beam. The z-axis is chosen such that it coincides with the optical axis and the focal plane, where the beam waist $w(z)$ reaches its smallest size w_0, coincides with the x-y-plane. α indicates the divergence angle of the beam and z_0 corresponds to the Rayleigh range.

To focus a Gaussian beam it is sent through a lens with a characteristic *numerical aperture* (NA), which is a dimensionless number characterizing the angular range (see Figure 1) over which an object can absorb or emit light. Using the angle α that defines the divergence of the beam starting at w_0 ($\alpha = 2/kw_0$) one then obtains an expression for the numerical aperture of the beam $\mathrm{NA} = n \cdot \sin(\alpha)$ [20]:

$$\mathrm{NA} = n \cdot \sin\left(\frac{2}{kw_0}\right). \tag{7}$$

Here, n corresponds to the index of refraction of the propagating medium.

For a collimated Gaussian beam the approximation NA≈0 is well justified. For small numerical apertures NA$\ll$ 1 and $\sin(\alpha) \approx \alpha$ an analytical expression for the refracted beam can be obtained using the paraxial solution, which is obtained when assuming that the beam only consist of transverse electromagnetic components (TEM beam) [20].

For lenses of high NA however, such as considered in this work (NA = 0.77), the resulting beam is no longer Gaussian around the focal plane thus one mostly resorts to numerical methods [22–24] to describe the electric field profile. Following the considerations of [20], a semi-analytical expression for a tightly focused Gaussian beam close to the focus can be formulated when solving the integrals in the angular spectrum representation of the focal field:

$$\boldsymbol{E}(r,\varphi,z) = \frac{ikfe^{-ikf}}{2\pi}\int_0^{\theta_{max}}\int_0^{2\pi}\boldsymbol{E}_\infty(\theta,\varphi)e^{ikz\cos(\theta)}e^{ikr\sin(\theta)\cos(\phi-\varphi)}\sin(\theta)\,d\phi\,d\theta, \tag{8}$$

where f is the focal length of the lens, $r = \sqrt{x^2+y^2}$, $\phi = \arctan(\mathrm{y/x})$, $\theta = \arccos(\mathrm{z/r})$, $\theta_{max} = \arcsin(NA/n)$ and $\boldsymbol{E}_\infty$ corresponds to the field refracted at the surface of the lens evaluated in the far-field limit w.r.t. the focus.

The numerical solution of eq. 8 yields bigger waist sizes along the axis of polarization than perpendicular to it due to the vector nature of the electric field [20]. Hence, in order to obtain an analytic expression for the focal field of a tightly focused Gaussian beam, one needs to fit the numeric solution with an expression of the form:

$$I(x,y,z) = \frac{2P}{\pi w^2(z)}e^{-\frac{x^2}{w_x^2(z)}-\frac{y^2}{w_y^2(z)}}, \tag{9}$$

where the waist now has different values in $x-$ and $y-$direction $w_x(z)$, $w_y(z)$ [25].

2.2 Mechanics of levitated nanoparticles

2.2.1 The dipole approximation

A particle illuminated by an optical field with wavelength $\lambda \gg r$, where r is the radius of the particle, can in good approximation be considered a point dipole. This dipole then oscillates with the same frequency as the incident field and hence emits light with the same frequency and phase (if $n_2 > n_1$, where $n_{1/2}$ is the refractive index of the particle and surrounding medium, respectively). This is the so-called *Rayleigh approximation*, which is a simplification of the full, extensive Mie-Scattering theory of light scattered by extended objects.[21].

Since dielectric particles have no static dipole moment, in the linear regime the particles dipole moment corresponds to its polarizability α times the strength of the electric field that induces it [26]:

$$\boldsymbol{d} = \alpha(\omega)\boldsymbol{E}, \qquad U = -\frac{1}{2}\boldsymbol{d}\cdot\boldsymbol{E}, \tag{10}$$

$$\text{with} \qquad \alpha(\omega) \approx \alpha_0 + i\frac{|\alpha_0|^2 k^3}{6\pi\varepsilon_0\varepsilon_1} \qquad \text{and} \qquad \alpha_0 = 4\pi\varepsilon_0 R^3 \frac{\varepsilon_2(\omega) - \varepsilon_1(\omega)}{\varepsilon_2(\omega) + 2\varepsilon_1(\omega)}. \tag{11}$$

Here, ε_0 is the vacuum permittivity, $\varepsilon_1, \varepsilon_2$ the relative permittivity of the surrounding medium and the particle, respectively and R is the particles radius [5]. The relative permittivity relates to the reflective index of a medium by $\varepsilon = n^2$ (for relative permeability $\mu \approx 1$). A complex permittivity implies an absorptive medium and hence α_0 is generally also complex. Splitting the complex polarizability into real and imaginary part yields

$$\alpha(\omega) = \alpha'(\omega) + i\alpha''(\omega) \approx \mathrm{Re}(\alpha_0) + i\left(\mathrm{Im}(\alpha_0) + \frac{|\alpha_0|^2 k^3}{6\pi\varepsilon_0\varepsilon_1}\right), \tag{12}$$

where $\alpha'(\omega)$ corresponds to the dispersive part of the polarizability and $\alpha''(\omega)$ to its dissipative part. The electric field scattered by a dipole can be obtained using the dyadic Greens function

$$\boldsymbol{E}(\boldsymbol{r}, t)_{dip} = \frac{\omega^2}{c^2}\boldsymbol{G}(\boldsymbol{r}, \boldsymbol{r}_0), \tag{13}$$

with

$$\boldsymbol{G}(\boldsymbol{r}, \boldsymbol{r}_0) = \frac{1}{4\pi\varepsilon_0\varepsilon_m R} e^{ikR}\left[\left(1 + \frac{ikR - 1}{k^2R^2}\right)\boldsymbol{I} + \frac{3 - 3ikR - k^2R^2}{k^2R^2}\frac{\boldsymbol{R}\otimes\boldsymbol{R}}{R^2}\right], \tag{14}$$

where $\boldsymbol{I}$ is the unit tensor and $\boldsymbol{R} = \boldsymbol{r} - \boldsymbol{r}_0$. Eq. 14 follows from the differential equation

$$\boldsymbol{G}(\boldsymbol{r}, \boldsymbol{r}_0) = (\boldsymbol{I} + \nabla\nabla)\, G(\boldsymbol{r}, \boldsymbol{r}_0), \qquad G(\boldsymbol{r}, \boldsymbol{r_0}) = \frac{e^{i\boldsymbol{k}|\boldsymbol{r} - \boldsymbol{r}_0|}}{4\pi|\boldsymbol{r} - \boldsymbol{r}_0|}, \tag{15}$$

where $G(\boldsymbol{r}, \boldsymbol{r_0})$ is the scalar Green's function for a field at position $\boldsymbol{r}$ emitted by a point source at position $\boldsymbol{r}_0$ [20].

In a spherical coordinate system with $\boldsymbol{d} = d\boldsymbol{e}_y$ and θ chosen such that $\theta = 0$ coincides with the direction of the induced dipole moment $\boldsymbol{d}$ and hence axis of polarization of the incident field (see Figure 2) the electric field of a dipole scatterer in the far field ($R \gg \lambda$ and thus keeping only terms $\mathcal{O}(1/R)$) then looks like

$$\boldsymbol{E}_{dip}(\boldsymbol{r}) \approx E_\theta \boldsymbol{e}_\theta = -\frac{|\boldsymbol{d}|\sin(\theta)}{4\pi\varepsilon_0\varepsilon_m}\frac{k^2}{r}e^{ikr}. \tag{16}$$

The electric field in the far field thus only has components in direction of θ, with increasing field strength for increasing angular distance to the dipole axis. When calculating the magnetic dipole field in a similar manner ($\boldsymbol{H}_{dip}(\boldsymbol{r}, t) = -i\omega\boldsymbol{d}(\nabla \times \boldsymbol{G})$), one obtains that it only has components in φ-direction. The Poynting vector, giving the direction of energy transport of the electromagnetic field is then given by [20]

$$\boldsymbol{S}(t) = \boldsymbol{E}_{dip}(t) \times \boldsymbol{H}_{dip}(t) = \frac{1}{16\pi^2\varepsilon_0\varepsilon_m} \frac{\sin^2(\theta)}{r^2} \frac{n^3\omega^4\boldsymbol{d}^2}{c^3}\boldsymbol{e}_r. \tag{17}$$

Eq. 17 shows, that the particle doesn't radiate in the direction of its induced dipole moment $\boldsymbol{d}$ and maximally radiates perpendicular to it (see Figure 2). From eq. 10 one can furthermore see that $\boldsymbol{d}$ oscillates with the same frequency ω as the incident field which causes the emitted field to also have the same frequency ω and phase (as long as $n_1 < n_2$) [5].

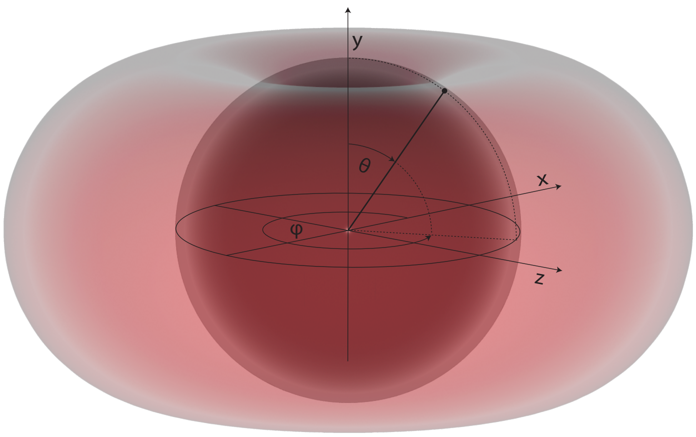

Figure 2: Sphere emitting dipole radiation. The radiation is zero along the dipole axis which coincides with the y-axis in this case and maximal perpendicular to it. The distance from the dipole axis is given by the angle $\theta = \arctan(x/y)$ and distances perpendicular to it are described by the angle $\varphi = -\arctan(z/x)$.

2.2.2 Forces in an optical trap

When looking at the forces that act on a particle in a harmonic trapping potential it makes sense to consider time-averages, since the light field oscillates much faster than the particle is able to follow due to its moment of inertia. The resulting force consists of two components: A term arising due to the electromagnetic field being scattered off the particle which induces a momentum change on the field and the Lorentz force acting on a moving charge in a spatially inhomogeneous field. After some manipulations using Maxwells equations [21] one then arrives at the following expression:

$$\langle \boldsymbol{F} \rangle = \frac{1}{2}\mathrm{Re}\left\{d_i^* \nabla E_i\right\}. \tag{18}$$

Inserting eq. 10 into eq. 18 and separating the complex polarizability α into its real and imaginary part: $\alpha = \alpha' + i\alpha''$ then leads to the final, well known expression for the force of a dielectric particle in an optical tweezer in the Rayleigh regime:

$$\langle \boldsymbol{F} \rangle = \frac{\alpha'}{4}\nabla|\boldsymbol{E}|^2 + \frac{\alpha''}{2}|\boldsymbol{E}|^2\nabla\varphi = \boldsymbol{F}_{grad} + \boldsymbol{F}_{scat}. \tag{19}$$

The first component in eq. 19 corresponds to the so called *gradient force*, proportional to the real (dispersive) part of the polarizability α' and the gradient of the field intensity ($\langle I \rangle \propto \langle |\boldsymbol{E}|^2 \rangle$). It accelerates dielectric particles into the direction of maximal field intensity and hence can trap a particle in the focal spot of a tightly focused beam.

The second component in eq. 19 corresponds to the so called *scattering force*, proportional to the imaginary (dissipative) part of the polarizability α'', the intensity of the field as well as its direction of propagation (since $\nabla\varphi = \nabla(\boldsymbol{kr}) = \boldsymbol{k}$, with $\boldsymbol{k}$ being the fields wavevector). Therefore, $\boldsymbol{F}_{scat}$ can be understood as the momentum transfer from the light field to the particle, pushing the particle away from the trap center. The scattering force is non-conservative since the light field constantly pumps energy onto the particle in the form of radiation pressure.

The equilibrium position of an optically trapped particle is therefore reached for $F_{grad} = -F_{scat}$. For $\alpha'' \neq 0$ it is thus positioned behind the focus in direction of propagation of the beam. Consequently, the focus of the trap must be tight enough in order for the particle not to be pushed out of the trap by radiation pressure (see Figure 3).

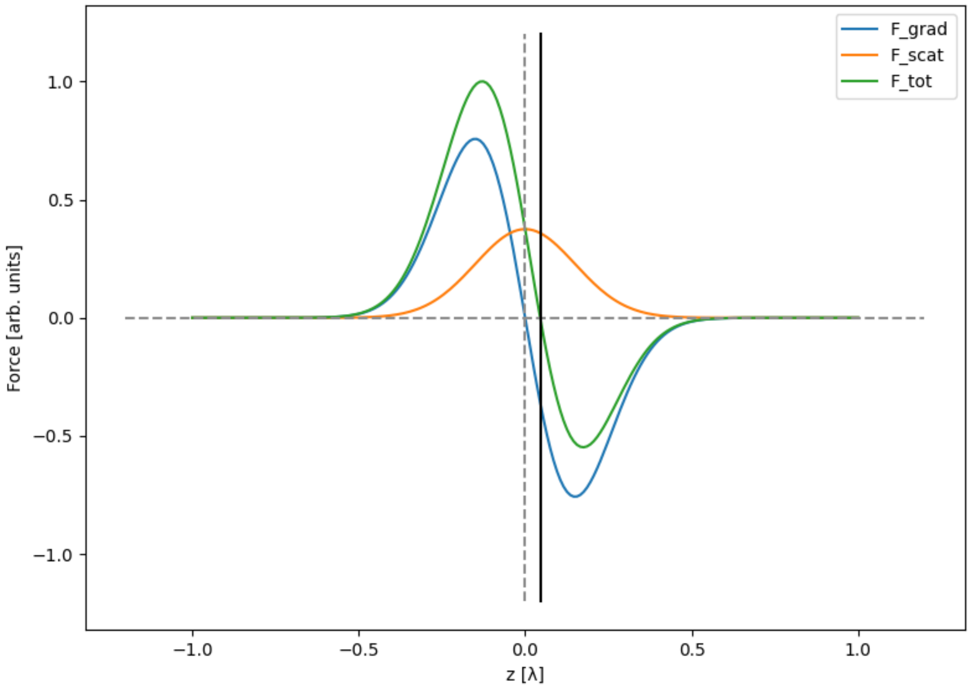

Figure 3: F_{grad} (blue) and F_{scat} (orange) for a dielectric nanoparticle trapped in an optical tweezer. One can see that due to the radiation pressure the position where the total force $F_{tot} = F_{grad} + F_{scat}$ (green) on the particle vanishes is shifted away from the focal point at $z = 0$ along the optical axis (black line).

2.2.3 Equations of motion

The scattering force is only acting in the direction of propagation, therefore the force in x and y direction is conservative [25]. One can assume the scattering force F_{scat} to be constant and therefore only causing a constant displacement of the equilibrium position of the particle inside the trap in z-direction ($z' = z + F_{scat}/(m\Omega_z^2)$), but not changing the shape of the potential (see Figure 3). The equations of motions of the particle thus stay the same when substituting z' for z.

Using $\boldsymbol{F} = -\boldsymbol{\nabla} U$, we can define the optical potential depth as:

$$U(x, y, z) = \frac{\alpha'}{2c\varepsilon_0} I(x, y, z). \tag{20}$$

For small displacements of the particle w.r.t. the trap center, the gradient force (see eq. 19) can be Taylor expanded to the first order, yielding a harmonic trap potential:

$$\boldsymbol{F}_{grad}(x, y, z) \approx \frac{\alpha'}{c\varepsilon_0} \frac{4P}{\pi w^2(z)} \left(\frac{x}{w_x^2} \boldsymbol{e}_x + \frac{y}{w_y^2} \boldsymbol{e}_y + \frac{z}{z_0^2} \boldsymbol{e}_z \right). \tag{21}$$

The oscillation frequencies are given by:

$$\begin{aligned} \Omega_{0,x}^2 &= \frac{\alpha'}{c\varepsilon_0} \frac{4P}{\pi w^2(z)} \frac{1}{w_x^2}, \\ \Omega_{0,y}^2 &= \frac{\alpha'}{c\varepsilon_0} \frac{4P}{\pi w^2(z)} \frac{1}{w_y^2}, \\ \Omega_{0,z}^2 &= \frac{\alpha'}{c\varepsilon_0} \frac{4P}{\pi w^2(z)} \frac{1}{z_0^2}. \end{aligned} \tag{22}$$

The Langevin equations of motion of this system are those of a thermally driven, damped harmonic oscillator. Using index notation ($x_{i=1,2,3} = x, y, z$) one obtains:

$$m\ddot{x}_i + m\gamma_{th}\dot{x}_i + m\Omega_{0,i}^2 x_i = F_{th,i}, \tag{23}$$

where $\gamma_{th} = 6\pi\eta r$ corresponds to the particle damping due to collisions with the surrounding gas molecules, with η being the viscosity of the surrounding medium and r the particles radius. F_{th} corresponds to a random force noise acting on the particle due to Brownian motion with autocorrelation function R_{FF}[27]:

$$R_{FF} = \langle F_{th}(t) F_{th}(t') \rangle = 2m\gamma_{th} k_B T \delta(t - t'). \tag{24}$$

2.2.4 Power spectral density

First, lets consider a **damped harmonic oscillator without driving force**.
Eq. 23 changes to

$$m\ddot{x}_i + m\gamma_{th}\dot{x}_i + m\Omega_{0,i}^2 x_i = 0, \tag{25}$$

which is easily solvable by choosing the exponential Ansatz. The solution for positions x_i and momenta p_i has the form:

$$x_i(t) = e^{-\frac{\gamma_{th}}{2} t} x_{0,i} \cos(\Omega_i t + \phi), \tag{26}$$

$$p_i(t) = e^{-\frac{\gamma_{th}}{2} t} x_{0,i} \left(-\frac{\gamma_{th}}{2} \cos(\Omega_i t + \phi) + \Omega_i \sin(\Omega_i t + \phi) \right), \tag{27}$$

where x_0, p_0 are the maximal amplitudes of position and momentum, $\Omega_i^2 = \Omega_{0,i}^2 - \left(\frac{\gamma_{th}}{2}\right)^2$ and ϕ is an arbitrary phase shift.

Here, one usually considers three limiting cases. The first one is called the *overdamped regime*, in case $\gamma_{th}/2 > \Omega_{0,i}$. Here, the oscillatior amplitued goes directly to zero and does not complete any oscillations.

The regime is called *critically damped*, if $\gamma_{th}/2 = \Omega_{0,i}$. Here, the amplitude of the oscillator reaches zero precisely after one oscillation.

Finally, the *underdamped regime* occurs when $\gamma_{th}/2 < \Omega_{0,i}$. In this regime, the harmonic oscillator undergoes multiple oscillations before it is damped to zero amplitude. This is the regime we are interested in when analysing the motion of dielectric particles in an optical tweezer potential. In case that $\Omega_0, i \gg \gamma_{th}$ one can make the approximation $\Omega_i \approx \Omega_{0,i}$ which is justified in the considered case (see Chapter 5) [28].

The **energy** of the damped undriven harmonic oscillator, consisting of the potential energy V and kinetic energy T can be expressed as:

$$E = V + T = \frac{1}{2} m\Omega_{0,i}^2 x_i^2 + \frac{1}{2} m\dot{x}_i^2 \tag{28}$$

$$\approx \frac{m\Omega_{0,i}^2}{2} e^{-\gamma_{th} t} \left(x_{0,i}^2 \cos^2(\Omega_i t + \phi) + x_{0,i}^2 \sin^2(\Omega_i t + \phi) \right)$$

$$= \frac{m\Omega_{0,i}^2 x_{0,i}^2}{2} e^{-\gamma_{th} t}. \tag{29}$$

A measure commonly used in this context is the **quality factor** Q. It is defined as

$$Q = 2\pi \frac{E}{\Delta E}, \tag{30}$$

where ΔE is the energy dissipated per oscillation cycle $\tau_i = \frac{2\pi}{\Omega_{0,i}}$. It can hence be written as

$$\Delta E = \frac{m\Omega_{0,i}^2 x_{0,i}^2}{2} e^{-\gamma_{th} t} - \frac{m\Omega_{0,i}^2 x_{0,i}^2}{2} e^{-\gamma_{th}(t+\tau)}, \tag{31}$$

leading to an expression for the quality factor of the form:

$$Q = 2\pi \frac{1}{1 - e^{-\gamma_{th}\tau_i}} \approx 2\pi \frac{1}{1 - (1 - \gamma_{th}\tau_i)} = \frac{\Omega_{0,i}}{\gamma_{th}}, \tag{32}$$

where $\gamma_{th}\tau \ll 1$ was assumed. From eq. 32 one can see, that Q can also be understood as the ratio of mechanical frequency to damping and hence the higher Q, the more oscillations will be performed before the oscillator arrives at its steady state [28].

Now, lets consider what happens in the case of a **damped harmonic oscillator with driving force**.
In order to solve the equations of motion including the external, thermal driving force of eq. 23, one has to change into Fourier space. The Fourier transform $\tilde{x}(\omega)$ of a variable $x(t)$ is defined as:

$$\tilde{x}(\omega) = \mathcal{F}[x(t)] = \int_{-\infty}^{\infty} x(t)\, e^{i\omega t} dt, \tag{33}$$

$$x(t) = \mathcal{F}^{-1}[\tilde{x}(\omega)] = \frac{1}{2\pi} \int_{-\infty}^{\infty} \tilde{x}(\omega)\, e^{-i\omega t} d\omega. \tag{34}$$

Eq. 34 implies that $\mathcal{F}(\dot{x}(t)) = \tilde{\dot{x}}(\omega) = -i\omega\tilde{x}(\omega)$ and $\mathcal{F}(\ddot{x}(t)) = \tilde{\ddot{x}}(\omega) = -\omega^2\tilde{x}(\omega)$. This can now be used to bring eq. 23 into frequency space:

$$-m\omega^2\tilde{x}_i - im\gamma_{th}\omega\tilde{x}_i + m\Omega_{0,i}^2\tilde{x}_i = \tilde{F}_{i,th},$$

$$\longrightarrow \tilde{x}_i\left(\Omega_{0,i}^2 - \omega^2 - i\gamma_{th}\omega\right) = \frac{\tilde{F}_{i,th}}{m}. \tag{35}$$

Eq. 35 can now be expressed in terms of the mechanical susceptibility $\chi(\omega)$ and $\tilde{f} = \frac{\tilde{F}_{i,th}}{m}$:

$$\chi_i(\omega) = \frac{1}{\Omega_{0,i}^2 - \omega^2 - i\gamma_{th}\omega}, \tag{36}$$

$$\tilde{x}_i(\omega) = \chi_i(\omega)\tilde{f}(\omega) = \frac{\tilde{f}(\omega)}{\Omega_{0,i}^2 - \omega^2 - i\gamma_{th}\omega}. \tag{37}$$

In order to transform $F_{i,th}$ into Fourier space, one can decompose the thermal force into a sum of sinusoidal driving forces with different frequencies ω_i:

$$F_{i,th}(t) = \sum_{j=0}^{\infty} F_{ij}\sin(\omega_j t + \phi) \tag{38}$$

and therefore

$$S_{FF} = \mathcal{F}(R_{FF}) = \langle\tilde{F}_{i,th}(\omega)\tilde{F}_{i,th}(\omega')\rangle = 2m\gamma_{th}k_BT\delta(\omega - \omega'). \tag{39}$$

Here, we have introduced the **power spectral density** (PSD) $S_{aa}(\omega)$ of a variable $a(t)$. According to the Wiener-Khintschin theorem it is defined as the Fourier transform of the autocorellation function $R_{aa}(t)$ in the limit of $T \to \infty$, where T corresponds to the measurement time [1]

$$R_{aa}(t) = \lim_{T\to\infty}\frac{1}{T}\int_{-\infty}^{\infty} a(t')\,a(t + t')dt'. \tag{40}$$

Furthermore, according to the convolution theorem:

$$S_{aa}(\omega) = \mathcal{F}(R_{aa}(t)) = \lim_{T\to\infty}\frac{1}{T}|\tilde{a}(\omega)|^2 = \langle|\tilde{a}(\omega)|^2\rangle. \tag{41}$$

Additionally, since $R_{aa}(t = 0) = \langle a^2(t)\rangle$, one finds the relation

$$\langle a^2(t)\rangle = \frac{1}{2\pi}\int_{-\infty}^{\infty} S_{aa}(\omega)d\omega = \frac{1}{\pi}\int_0^{\infty} S_{aa}(\omega)d\omega. \tag{42}$$

The last step of eq. 42 is justified since the classical PSD is an even function of frequency ω. Eq. 42 shows that the PSD is a measure for the time average of the squared amplitude $\langle x^2(t)\rangle$ of our oscillator [28].

Combining eq. 37 and eq. 39, one can find an analytical expression for $S_{xx}(\omega)$:

$$S_{xx,i}(\omega) = |\chi_i(\omega)|^2\,\frac{S_{FF}}{m^2} = \frac{2\gamma_{th}k_BT}{m\left((\Omega_{0,i}^2 - \omega^2)^2 + \gamma_{th}^2\omega^2\right)}. \tag{43}$$

For small γ, one can approximate $\Omega_{0,i} \approx \omega$ and hence $(\Omega_{0,i}^2 - \omega^2) \approx 2\Omega_{0,i}(\Omega_{0,i} - \omega)$ which then yields the well known Lorentzian line shape

$$S_{xx,i}(\omega) \approx \frac{\gamma_{th} k_B T}{2m\Omega^2} \frac{\gamma_{th}}{\left(\Omega_{0,i} - \omega\right)^2 + (\gamma_{th}/2)^2}. \tag{44}$$

Alternatively, one could have also obtained an analytic expression for S_{xx} by making use of the fluctuation-dissipation theorem. It relates the response of a system in thermal equilibrium when subjected to noise to its dissipative properties:

$$S_{xx,i}(\omega) = \frac{2k_B T}{\omega} \mathrm{Im}\left(\chi_i(\omega)\right). \tag{45}$$

Since the energy of the oscillator is also proportional to $\langle x^2 \rangle$ (see eq. 29), integrating over the PSD in thermal equilibrium yields (according to the equipartition theorem [1]):

$$\langle x_i(t)^2 \rangle = \frac{1}{\pi} \int_0^\infty S_{xx,i}(\omega) d\omega = \frac{k_B T}{m\Omega_0^2}. \tag{46}$$

3 Dynamics of coupled particles

Single particles in optical tweezers are well studied and have opened the door to novel reasearch areas with milestone experiments such as the groundstate cooling of a nanometer sized particles motion [2–4], enhanced force sensing for the search of forces beyond the standard model e.g. [29], or the behaviour of thermodynamical processes far from equilibrium [30, 31].

However, observing only a single particle interacting with off resonant radiation leads to simplified dynamics that are non-sufficient for describing many important phenomena occurring e.g. in many body physics. Studying the dynamics of two particles trapped in vicinity to each other can give us insights into collective effects such as nonreciprocal phonon transport and topological phase transitions in phononic metamaterials [32, 33], or even stationary multipartite entanglement [34].

3.1 Two coupled harmonic oscillators

Most kinds of optomechanical interaction can be boiled down to the study of coupled harmonic oscillators. In cavity optomechanics the cavity field and the particle motion are described as two harmonic oscillators. Strong optomechanical interaction ($g \geq \kappa/2$, κ being the cavity linewidth), which is mostly achieved by enhancement via cavity (see e.g. [35]), gives rise to two normal modes that consist of a combination of the motion of the two oscillators and are typically referred to as polaritons [1].

Therefore, I firstly want to derive the most important dynamics that appear when considering conservatively coupled harmonic oscillators. This will establish a terminology that can later be used in sec. 3.2 and 3.3.

Constant, equal coupling rates

Lets consider the one-dimensional problem of two spheres of equal size and mass connected to walls with springs with equal spring constants $k = m\Omega^2$ and to each other with a second spring with spring constant $\tilde{k} = m\tilde{\Omega}^2$ (see Figure 4). In analogy to eq. 23 their equations of motions are

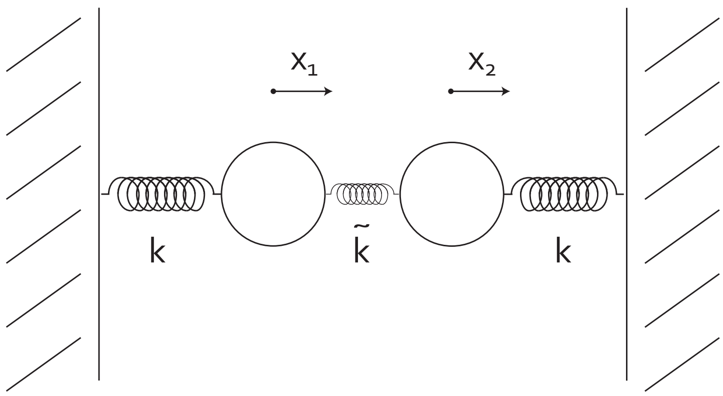

Figure 4: Two harmonic oscillators coupled to walls with equal spring constants $k = m\Omega^2$ and also to each other via spring constant $\tilde{k} = m\tilde{\Omega}^2$.

therefore of the form

$$m\ddot{x}_1 + m\gamma\dot{x}_1 + kx_1 + \tilde{k}(x_1 - x_2) = F_1, \tag{47}$$

$$m\ddot{x}_2 + m\gamma\dot{x}_2 + kx_2 + \tilde{k}(x_2 - x_1) = F_2. \tag{48}$$

By taking the sum and difference of eq. 47 and 48 and substituting $\tilde{x}_1 = x_1 + x_2$ and $\tilde{x}_2 = x_1 - x_2$ one than obtains

$$m\ddot{\tilde{x}}_1 + m\gamma\dot{\tilde{x}}_1 + k\tilde{x}_1 = \frac{F_1 + F_2}{2}, \tag{49}$$

$$m\ddot{\tilde{x}}_2 + m\gamma\dot{\tilde{x}}_2 + (k + 2\tilde{k})\tilde{x}_2 = \frac{F_1 - F_2}{2}. \tag{50}$$

We've now created two uncoupled equations of motion, with $\tilde{x}_1 = x_1 + x_2$ and $\tilde{x}_2 = x_1 - x_2$ being the eigenmodes of the coupled harmonic oscillators and $\tilde{\Omega}_1^2 = \frac{k}{m}$, $\tilde{\Omega}_2^2 = \frac{k+2\tilde{k}}{m}$ being their eigenfrequencies. $\tilde{x}_1$ and $\tilde{x}_2$ are often referred to as *center of mass mode* and *breathing mode*, since $\tilde{x}_1$ follows the center of mass motion of the two oscillators and $\tilde{x}_2$ their motional distance. Only the breathing mode is then modified through coupling as can be seen from eq. 50, while the center of mass mode continues to oscillate with the eigenfrequency of the uncoupled modes (see eq. 49). The frequency of the breathing mode is increased with respect to the center of mass mode for $\tilde{k} > 0$ and decreased for $\tilde{k} < 0$.

Non-degenerate frequencies

Of course, for more complex relationships between the two oscillators, the system of equations becomes harder to solve and one has to solve the eigenvalue problems using a more general approach (see e.g. [35, 36]). In this derivation we will ignore the thermal driving force for simplicity reasons, since this Chapter is meant to give a general understanding of the dynamics of coupled particles and the thermal driving force just adds an inhomogeneous term to the coupled equations of motion. Say, for example, that we have two distinct, time dependent spring constants $k_1(t)$ and $k_2(t)$ as well as again our inter-oscillator coupling constant $\tilde{k}$. One can rewrite the equations of motion in matrix form:

$$\begin{bmatrix} m\frac{d^2}{dt^2} + m\gamma\frac{d}{dt} + k_1 + \tilde{k} & -\tilde{k} \\ -\tilde{k} & m\frac{d^2}{dt^2} + m\gamma\frac{d}{dt} + k_2 + \tilde{k} \end{bmatrix} \cdot \begin{bmatrix} x_1 \\ x_2 \end{bmatrix} = \begin{bmatrix} 0 \\ 0 \end{bmatrix}. \tag{51}$$

In order to facilitate the following equations, lets define $k_1 = k + \Delta k$ and $k_2 = k - \Delta k$. We can then rewrite our system of equations as

$$\underbrace{\begin{bmatrix} m\frac{d^2}{dt^2} + m\gamma\frac{d}{dt} + k + \tilde{k} & 0 \\ 0 & m\frac{d^2}{dt^2} + m\gamma\frac{d}{dt} + k + \tilde{k} \end{bmatrix}}_{\boldsymbol{A}} \cdot \begin{bmatrix} x_1 \\ x_2 \end{bmatrix} + \underbrace{\begin{bmatrix} \Delta k & -\tilde{k} \\ -\tilde{k} & -\Delta k \end{bmatrix}}_{\boldsymbol{B}} \cdot \begin{bmatrix} x_1 \\ x_2 \end{bmatrix} = \begin{bmatrix} 0 \\ 0 \end{bmatrix}. \tag{52}$$

We already know the solution to the equation $\boldsymbol{AX} = \boldsymbol{0}$, where $\boldsymbol{X} = (x_1, x_2)^T$. It just consists of two uncoupled harmonic oscillators (see eq. 25). One way of solving the coupled system of equations is to calculate the eigenvalues of matrix $\boldsymbol{B}$.

The eigenvalues λ of $\boldsymbol{B}$ are

$$\lambda_{1,2} = \pm\sqrt{\Delta k^2 + \tilde{k}^2} = \pm\kappa$$

and the corresponding eigenvectors $\tilde{\boldsymbol{X}}$ solve the following system of equations:

$$(\boldsymbol{B} - \lambda \boldsymbol{I}) \cdot \tilde{\boldsymbol{X}} = \boldsymbol{0} \qquad \longrightarrow \qquad \tilde{\boldsymbol{X}}_{1,2} = \frac{1}{\sqrt{1 + \left(\frac{-\Delta k \pm \kappa}{\tilde{k}}\right)^2}} \begin{bmatrix} 1 \\ \frac{-\Delta k \pm \kappa}{\tilde{k}} \end{bmatrix}.$$

Since $\boldsymbol{B}$ is symmetric, there exists an orthogonal basis transformation $\boldsymbol{S}$, such that $\boldsymbol{S}^{-1}\boldsymbol{B}\boldsymbol{S} = \boldsymbol{D}$, where $\boldsymbol{D}$ is a diagonal matrix. This means that

$$\boldsymbol{S}^{-1} \cdot \begin{bmatrix} \Delta k & -\tilde{k} \\ -\tilde{k} & -\Delta k \end{bmatrix} \cdot \boldsymbol{S} = \begin{bmatrix} \kappa & 0 \\ 0 & -\kappa \end{bmatrix}. \tag{53}$$

with eigenvectors $\tilde{\boldsymbol{X}} = \boldsymbol{S}\boldsymbol{X}$. Therefore,

$$\boldsymbol{A}\boldsymbol{X} + \boldsymbol{B}\boldsymbol{X} = \boldsymbol{A}\boldsymbol{S}^{-1}\tilde{\boldsymbol{X}} + \boldsymbol{B}\boldsymbol{S}^{-1}\tilde{\boldsymbol{X}} = \boldsymbol{0}, \tag{54}$$

when multiplied with $\boldsymbol{S}$ this gives

$$\boldsymbol{A}\tilde{\boldsymbol{X}} + \underbrace{\boldsymbol{D}}_{\boldsymbol{S}\boldsymbol{B}\boldsymbol{S}^{-1}} \tilde{\boldsymbol{X}} = \boldsymbol{0}. \tag{55}$$

This means, that eq. 52 is now a decoupled system of equations dependent on normal modes $\tilde{\boldsymbol{X}} = (\tilde{x}_1, \tilde{x}_2)^T = \boldsymbol{S}\boldsymbol{X}$

$$\underbrace{\begin{bmatrix} m\frac{d^2}{dt^2} + m\gamma\frac{d}{dt} + k + \tilde{k} & 0 \\ 0 & m\frac{d^2}{dt^2} + m\gamma\frac{d}{dt} + k + \tilde{k} \end{bmatrix}}_{\boldsymbol{A}} \cdot \begin{bmatrix} \tilde{x}_1 \\ \tilde{x}_2 \end{bmatrix} + \underbrace{\begin{bmatrix} \kappa & 0 \\ 0 & -\kappa \end{bmatrix}}_{\boldsymbol{D}} \cdot \begin{bmatrix} \tilde{x}_1 \\ \tilde{x}_2 \end{bmatrix} = \begin{bmatrix} 0 \\ 0 \end{bmatrix}, \tag{56}$$

with eigenfrequencies

$$\tilde{\Omega}_{1,2}^2 = \frac{k + \tilde{k} \pm \kappa}{m} = \Omega^2 \pm \sqrt{\Delta\Omega_0^4 + \Omega_c^4}. \tag{57}$$

Here, $\Omega^2 = \frac{k+\tilde{k}}{m}$ is the modified frequency without detuning, $\Delta\Omega_0^2 = \frac{\Delta k}{m}$ is the variable detuning of the individual oscillator frequencies and $\Omega_c^2 = \frac{\tilde{k}}{m}$ corresponds to the frequency changes due to coupling. One can see that for $k_1 = k_2 = k$ the term $\Delta\Omega_0$ of eq. 57 becomes zero and one recovers the same solutions as we obtained for eq. 49 and 50.

The system Hamiltonian (see eq. 28) in the new coordinate basis then takes the form

$$H_{1,2} = \frac{\dot{\tilde{x}}_{1,2}^2}{2m} + \frac{m\tilde{\Omega}_{1,2}^2\tilde{x}_{1,2}^2}{2} = \frac{\dot{\tilde{x}}_{1,2}^2}{2m} + \frac{m\left(\Omega^2 \pm \sqrt{\Delta\Omega_0^4 + \Omega_c^4}\right)\tilde{x}_{1,2}^2}{2}. \tag{58}$$

From this, one can immediately see that the eigenenergies of the normal modes will never overlap and hence, H_1 will always be greater than H_2 (see Figure 5). This phenomenon is called normal mode splitting. However, it only becomes visible when the coupling is strong enough for the minimal splitting (commonly referred to as g) to be larger then the mechanical linewidth [37]:

$$\Delta\tilde{\Omega}(\Delta k = 0) = 2g = \left(\sqrt{\Omega^2 + \Omega_c^2}\right) - \left(\sqrt{\Omega^2 - \Omega_c^2}\right) \approx \frac{\Omega_c}{\Omega} > \frac{\gamma}{2}, \tag{59}$$

where the approximation $\Omega_c \ll \Omega$ was made.

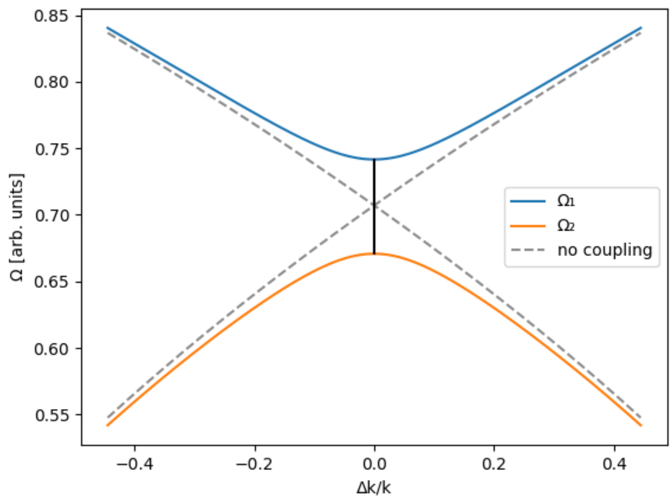

Figure 5: Frequency spliting between the two normal modes of two coupled harmonic oscillator with relative coupling strength $\tilde{k}/k \approx 0.1$ as a function of detuning $\Delta k = m\Delta\Omega^2$ between the two oscillators.

3.2 Coulomb coupling

Optically levitated particles are able to hold positive or negative charges, which in the past has been exploited to control or even cool their motion to the groundstate [3, 4, 38]. This means, that two particles can couple via electrostatic interaction. This interaction will be studied in this Chapter.

The Coulomb potential V_C is given by [20]

$$V_C(r) = \frac{1}{4\pi\varepsilon_0}\frac{q_1 q_2}{r}, \tag{60}$$

where, $q_{1,2}$ are the charges of particle 1 and 2, respectively, and $r = \sqrt{(R_0 + x_1 - x_2)^2}$ is their distance. We consider two particles trapped in two optical tweezers at a mean distance R_0 from each other (see Figure 6). We assume small displacements $x_1 - x_2$ along the x-axis. Expanding the potential V_C up to the second order yields [39]

$$V_C = \frac{1}{4\pi\varepsilon_0}\frac{q_1 q_2}{\sqrt{R_0^2 + (x_1 - x_2)^2}} \approx \frac{1}{4\pi\varepsilon_0}\frac{q_1 q_2}{R_0}\left(1 - \frac{(x_1 - x_2)^2}{2R_0^2}\right). \tag{61}$$

Since we are interested in the system dynamics we neglect he constant offset term in V_C. The electrostatic coupling leads to two effects. A modified spring constant

$$\Omega = \sqrt{\frac{k - \tilde{k}}{m}} = \sqrt{\Omega_0^2 - \frac{1}{4\pi\varepsilon_0 m}\frac{q_1 q_2}{R_0^3}} \tag{62}$$

as well as a coupling of the x-motions of the two particles. Using the modulated frequency Ω for the particles motion, we can write the equations of motion after the Taylor expansion in analogy to eq. 51 to find the coupling rate g between the two oscillators as well as the new eigenfrequencies $\tilde{\Omega}_{1,2}$:

$$m\ddot{x}_1 + m\gamma\dot{x}_1 + \underbrace{m(\Omega^2 + \Delta\Omega^2)}_{k+\Delta k} x_1 - \underbrace{\frac{1}{4\pi\varepsilon_0}\frac{q_1 q_2}{R_0^3}}_{-\tilde{k}}(x_1 - x_2) = F_{1,th}, \tag{63}$$

$$m\ddot{x}_2 + m\gamma\dot{x}_2 + \underbrace{m(\Omega^2 - \Delta\Omega^2)}_{k-\Delta k} x_2 - \underbrace{\frac{1}{4\pi\varepsilon_0}\frac{q_1 q_2}{R_0^3}}_{-\tilde{k}}(x_2 - x_1) = F_{2,th}. \tag{64}$$

Using the relation $\Delta\tilde{\Omega}(\Delta k = 0) = \tilde{\Omega}_2 - \tilde{\Omega}_1 = 2g$ for $\tilde{\Omega}_1, \tilde{\Omega}_2 \gg g$ [1], together with eq. 57, one then obtains

$$\tilde{\Omega}_{1,2}(\Delta k = 0) = \sqrt{\frac{k + \tilde{k}}{m} \pm \frac{\tilde{k}}{m}}$$

$$\approx \sqrt{\frac{k}{m}} + \frac{1}{2}\sqrt{\frac{m}{k}}\left(\frac{1}{m} \pm \frac{1}{m}\right)\tilde{k} = \Omega + \frac{1}{2\Omega}\left(\frac{\tilde{k}}{m} \pm \frac{\tilde{k}}{m}\right)$$

for $\tilde{k} \to 0$, leading to a coupling rate

$$g = \frac{\tilde{\Omega}_2 - \tilde{\Omega}_1}{2} \overset{\Delta k=0}{\approx} \frac{\tilde{k}}{2\Omega m}. \tag{65}$$

The system Hamiltonian for the case of minimal splitting can then be written as:

$$H = \frac{m\dot{x}_1^2}{2} + \frac{m\dot{x}_2^2}{2} + \frac{m\Omega^2 x_1^2}{2} + \frac{m\Omega^2 x_2^2}{2} + g x_1 x_2, \tag{66}$$

with

$$\Omega^2 = \Omega_0^2 - \frac{1}{4\pi\varepsilon_0 m}\frac{q_1 q_2}{R_0^3}, \qquad g = -\frac{1}{8\pi\varepsilon_0 m}\frac{q_1 q_2}{R_0^3 \Omega}. \tag{67}$$

The Coulomb coupling between two harmonic oscillators hence depends on the product of the number of charges they carry and decreases with $\propto r^{-3}$.

3.3 Optical interaction

Another coupling mechanism present between dielectric levitated particles occurs due to the interaction of their trapping fields with the dipole radiation fields and is commonly referred to as *optical binding* [7, 8, 10, 11, 40, 41]. Intuitively, one can understand the coupling mechanism the following way:

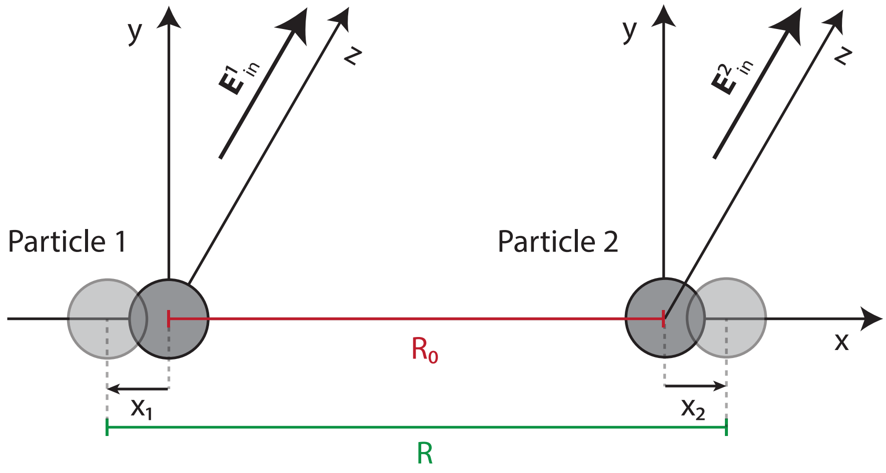

Figure 6: Coordinate system chosen for two particles trapped along the x-axis. The z-axes coincide with the tweezer axes. The origin of their individual coordinate systems is chosen to correspond to their mean distance from each other R_0. The total distance R is then given by the absolute value of their mean distance R_0 plus the difference of their positions relative to their respective coordinate origins $R = \sqrt{(R_0 + x_1 - x_2)^2}$

.

Consider two particles with radius r much smaller than the wavelength of the trapping field inside the propagating medium λ ($r \ll \lambda$), optically trapped next to each other and radiating light that is phase coherent with their trapping field. The laser induced dipole radiation on particle 1 (see Chapter 2.2) will alter the potential that particle 2 experiences. Two distinct effects come into play: Firstly, the field radiated off particle 1 will interact with the dipole induced in particle 2 through the incident electric field $\mathbf{E}^I(\mathbf{r_2}, t)$ at the position of particle 2. Secondly, the light scattered from particle 1 will also induce a dipole moment in particle 2 that then interacts with the incident field at the position of particle 2 [7]. Of course, this would in theory lead to infinite scattering events. However, one can assume that for sufficiently small particles (and hence small polarizabilities) one can neglect those self induced scattering events. This is called the *first Born approximation* [26].

For the remainder of this Chapter the Einstein notation will be used, meaning that an index appearing twice in a term indicates summation over all the terms of that index ($\alpha_i x_i = \sum_{i=1}^{3} \alpha_i x_i$).

The particle can then be assumed to be a point dipole and the electric field will be locally approximated as a monochromatic Gaussian beam propagating in z-direction $\mathbf{E}(\mathbf{r}, t) \approx \mathbf{E_0}\ e^{i(k(1-z/z_0)z+\omega t+\phi)}$, where k is the wavenumber, ω the frequency of the light field, z_0 the Rayleigh length and t the time. For simplicity reasons I will neglect the time dependency of the electric field for the following derivations and just consider the spatial dependence $\mathbf{E}(\mathbf{r})$.

The dipole moments $d_i(\mathbf{r}_1)$ and $d_i(\mathbf{r}_2)$ have the form described in eq. 10:

$$d_i(\boldsymbol{r}_{1,2}) = \alpha_{1,2} \cdot E_i(\boldsymbol{r}_{1,2}),$$

where $\boldsymbol{E}(\boldsymbol{r}_{1,2})$ corresponds to the total electric field at position of particle 1, 2. The dipole then oscillates with the same frequency as the incident field creating a radiation field that interacts with the second particle. The total electric field at the position of particle 2 hence consists of the following terms:

$$E_i(\boldsymbol{r}_2) = E_i^{I_2}(\boldsymbol{r}_2) + G_{ij}(R) \cdot \alpha_1 \cdot E_j(\boldsymbol{r}_1). \tag{68}$$

Here, $E_i^{I_2}(\boldsymbol{r})$ corresponds to the incident electric field at the position of particle 2, $G_{ij}(R)$ is the retarded dipole-dipole field propagator as a function of the distance between the two particles $R = |\boldsymbol{R}|$ with $\boldsymbol{R} = \boldsymbol{r}_2 - \boldsymbol{r}_1$ (see Chapter 2.2.1 for more details on the dyadic Greens function). In index notation it takes the form

$$G_{ij}(R) = \frac{1}{4\pi\varepsilon_0\varepsilon_m R^3} e^{ikR} \left[\left(3 - 3ikR - k^2R^2\right) \frac{R_i R_j}{R^2} + (k^2R^2 + ikR - 1)\delta_{ij} \right], \tag{69}$$

where δ_{ij} corresponds to the Kronecker-Delta.

In eq. 14 three different terms appear that are either $\propto R^{-1}$, $\propto R^{-2}$ or $\propto R^{-3}$. The term that dominates depends on whether one considers the near field $R \ll \lambda$, intermediate field $R \approx \lambda$ or the far field $R \gg \lambda$.

One can now rewrite eq. 68 in terms of the incident fields $\boldsymbol{E}^{I_1}, \boldsymbol{E}^{I_2}$ and the tensor Λ_{ij}:

$$E_i(\boldsymbol{r}_2) = E_i^{I_2}(\boldsymbol{r}_2) + \Lambda_{ij} G_{jk}(R) \cdot \alpha_1 \cdot E_k^{I_1}(\boldsymbol{r}_1),$$

where Λ_{ij} corresponds to the change in the field due to the multiple scattering events. However, these can be neglected in the considered scenario when taking the first Born approximation, which results in $\Lambda_{ij} = \delta_{ij}$ and eq. 68 becomes

$$E_i(\boldsymbol{r}_2) = E_i^{I_2}(\boldsymbol{r}_2) + G_{ij}(R) \cdot \alpha_1 \cdot E_j^{I_1}(\mathbf{r}_1). \tag{70}$$

According to eq. 18 in Chapter 2.2, a dielectric particle irradiated by a monochromatic light wave experiences the time averaged force

$$\langle \boldsymbol{F}(\boldsymbol{r}) \rangle = \frac{1}{2} \mathrm{Re} \left\{ d_i^* \boldsymbol{\nabla} E_i(\boldsymbol{r}) \right\}.$$

With the relation

$$\begin{aligned} \partial_i E_j(\boldsymbol{r})\Big|_{\boldsymbol{r}=\boldsymbol{r}_1} = \partial_i^1 E_j(\boldsymbol{r}_1) =& \partial_i^1 \left(E_j^{I_1}(\boldsymbol{r}_1) + G_{jk}\alpha_2 E_k^{I_2}(\boldsymbol{r}_2) \right) \\ =& \partial_i^1 (E_j^{I_1}(\boldsymbol{r}_1)) + \partial_i^1 (G_{jk})\alpha_2 E_k^{I_2}(\boldsymbol{r}_2) + G_{jk} \underbrace{\partial_i^1 (\alpha_2 E_k^{I_2}(\boldsymbol{r}_2))}_{0}, \end{aligned}$$

where eq. 70 was used, the force acting on particle 1 can hence be written as:

$$\begin{aligned} \langle F_i(\boldsymbol{r_1}) \rangle =& \frac{1}{2} \mathrm{Re} \left\{ \alpha_1^* E_j^*(\boldsymbol{r}_1) \partial_i^1 E_j(\boldsymbol{r}_1) \right\} \\ =& \frac{1}{2} \mathrm{Re} \left\{ \alpha_1^* \left(E_j^{I_1 *}(\boldsymbol{r}_1) + G_{jk}^* \alpha_2^* E_k^{I_2 *}(\boldsymbol{r}_2) \right) \left(\partial_i^1 E_j^{I_1}(\boldsymbol{r}_1) + \partial_i^1 (G_{jk}) \alpha_2 E_k^{I_2}(\boldsymbol{r}_2) \right) \right\}. \end{aligned}$$

Since we here consider the case of two identical, isotropic spheres, the polarizability of both particles is the same and hence we can write $\alpha_1 = \alpha_2 = \alpha$. Additionally, α scales with the volume and since $r^3 \ll r$, for $r \ll 1$ it is justifies neglecting terms of order $\mathcal{O}(V^3)$, obtaining the simplified expression:

$$\langle F_i(\boldsymbol{r}_1)\rangle = \frac{1}{2}\mathrm{Re}\Big\{\underbrace{\alpha^* E_j^{I_1*}(\boldsymbol{r}_1)\partial_i^1 E_j^{I_1}(\boldsymbol{r}_1)}_{F_i^{OP}} + \underbrace{(\alpha^*)^2 G_{jk}^* E_k^{I_2*}(\boldsymbol{r}_2)\partial_i^1 E_j^{I_1}(\boldsymbol{r}_1)}_{F_i^{int,1}} + \underbrace{|\alpha|^2 E_j^{I_1*}(\boldsymbol{r}_1)\partial_i^1 (G_{jk}) E_k^{I_2}(\boldsymbol{r}_2)}_{F_i^{int,2}}\Big\}. \tag{71}$$

Here, F^{OP} corresponds to the optical force acting on a single dipole irradiated by a monochromatic field as described in Chapter 2.2. $F^{int,1}$ describes the interaction between the incident field $\boldsymbol{E}^{I_1}(\boldsymbol{r}_1)$ illuminating particle 1 and the part of the dipole induced in particle 1 by the radiated dipole field of particle 2 at position of particle 1. $F^{int,2}$, on the other hand, accounts for the interaction between the part of the dipole induced in particle 1 by the incident field $\boldsymbol{E}^{I_1}(\boldsymbol{r}_1)$ and the dipole field of particle 2.
The force acting on particle 2 can be obtained by changing all indices ($1 \to 2$ and $2 \to 1$) of eq. 71.

A full solution of eq. 71 can be found in appendix 6. Here, we'll apply the developed formalism on the specific experimental situation of parallel optical tweezers, which is typically referred to as *lateral optical binding*.

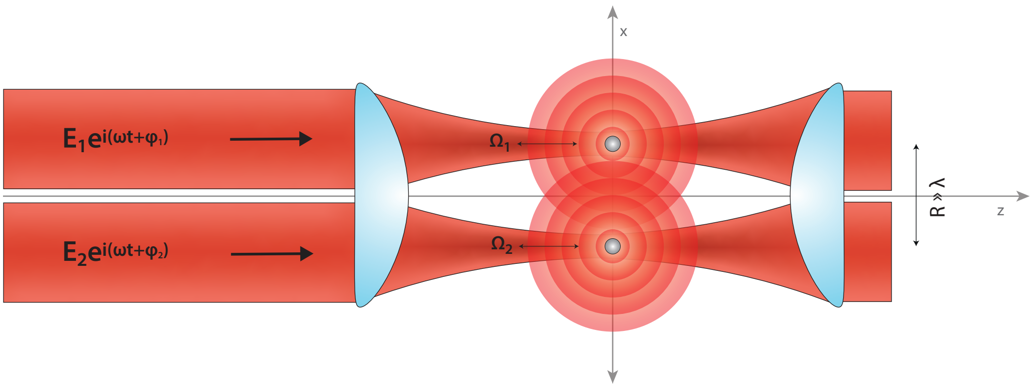

Figure 7: Sketch of the system under consideration. Two parallel, collimated Gaussian beams with individual amplitude, phase are focused by the same trapping lens. They form two parallel optical traps in a distance $d \gg \lambda$, each trapping a dielectric nanoparticle that can be approximated as a point dipole which radiates light with the same frequency and phase as the incoming field towards each other. Furthermore, they each oscillate with their individual eigenfrequencies, depending on the power and shape of the trapping potential.

3.3.1 Lateral optical binding

We consider the case of two parallel optical tweezers with foci seperated by the distance $R \gg \lambda$. In order to simplify the calculations, the coordinate system was chosen in such a way that the incident plane wave propagates in the z-direction and is polarized in the y-direction. Furthermore, the position of particle 2 was chosen to coincide with the origin of the coordinate system (see fig 8). We first analyze the simplified dynamics in the plane perpendicular to the optical axis, such that the distance vector $\boldsymbol{R}$ showing in direction of particle 1 can be written as $\boldsymbol{R} = -\boldsymbol{r}_1 =$

$R(\sin(\varphi),\, \cos(\varphi),\, 0)$, with $R = \sqrt{x_1^2 + y_1^2 + z_1^2}$ and $\varphi = \arctan(x_1/y_1)$.

After some calculation (given in Appendix: 6), one arrives at the following expressions for the forces on particle 1 in the far field:

$$\begin{aligned}\langle F_r(\boldsymbol{r}_1)\rangle =& \frac{|\alpha|^2 E_{0,1}E_{0,2}k^2}{8\pi\varepsilon_0\varepsilon_m R}\Big[k\sin(kR+\phi)\left(\cos^2(\varphi)-1\right)\\ &+\frac{2}{R}\cos(kR+\phi)\left(2\cos^2(\varphi)-1\right)\Big],\end{aligned} \tag{72}$$

$$\langle F_\varphi(\boldsymbol{r}_1)\rangle = \frac{|\alpha|^2 E_{0,1}E_{0,2}k^2}{8\pi\varepsilon_0\varepsilon_m R^2}\sin(2\varphi)\cos(kR+\phi), \tag{73}$$

$$\begin{aligned}\langle F_z(\boldsymbol{r}_1)\rangle =& \frac{1}{2}\tilde{k}\alpha''|E_{0,1}|^2 + \frac{E_{0,1}E_{0,2}}{8\pi\varepsilon_0\varepsilon_m R}\big[\tilde{k}k^2\sin^2(\varphi)\big(2\alpha'\alpha''\cos(kR+\phi)\\ &+\left(\alpha'^2-\alpha''^2\right)\sin(kR+\phi)\big)\big],\end{aligned} \tag{74}$$

with $\tilde{k} = k - 1/z_0$ and $\phi = \phi_2 - \phi_1$ is the relative phase between the two light fields at the position of the particles.

For the forces on particle 2, particle 1 is positioned in the coordinate origin, such that $\boldsymbol{R} = \boldsymbol{r}_2 = R(\sin(\varphi),\, \cos(\varphi),\, 0)$. This leads to:

$$\begin{aligned}\langle F_r(\boldsymbol{r}_2)\rangle =& \frac{|\alpha|^2 E_{0,1}E_{0,2}k^2}{8\pi\varepsilon_0\varepsilon_m R}\Big[k\sin(kR-\phi)\left(\cos^2(\varphi)-1\right)\\ &+\frac{2}{R}\cos(kR-\phi)\left(2\cos^2(\varphi)-1\right)\Big],\end{aligned} \tag{75}$$

$$\langle F_\varphi(\boldsymbol{r}_2)\rangle = \frac{|\alpha|^2 E_{0,1}E_{0,2}k^2}{8\pi\varepsilon_0\varepsilon_m R^2}\sin(2\varphi)\cos(kR-\phi), \tag{76}$$

$$\begin{aligned}\langle F_z(\boldsymbol{r}_2)\rangle =& \frac{1}{2}\tilde{k}\alpha''|E_{0,2}|^2 + \frac{E_{0,1}E_{0,2}}{8\pi\varepsilon_0\varepsilon_m R}\big[\tilde{k}k^2\sin^2(\varphi)\big(2\alpha'\alpha''\cos(kR-\phi)\\ &+\left(\alpha'^2-\alpha''^2\right)\sin(kR-\phi)\big)\big].\end{aligned} \tag{77}$$

The term $\frac{\tilde{k}}{2}\alpha''|E_0|^2$ in eq. 74 and 77 corresponds to the radiation pressure force that is acting on a single particle in a plane wave. The relation $\alpha = \alpha' + i\alpha''$ was used. The other term corresponds to the radiation pressure force change due to the interference between the scattered field of particle 2 and the incident field.

Eq. 72 shows, that the dominant term $\propto 1/R$ is maximal for $\varphi = \pm\pi/2$ and vanishes for $\varphi = 0, \pi$. This is due to the fact that a dipole always radiates maximally in the direction orthogonal to its polarization, while its radiation along the axis of polarization vanishes for $R \gg \lambda$ (see Chapter 2.2). This term corresponds to the radiated dipole field of particle 2 acting on the dipole induced in particle 1 due to the incident field. The behaviour is illustrated in Figure 9a.

For R orthogonal to the axis of polarization, and hence $\varphi = \pm\pi/2$, the force changes sinusoidaly with respect to kR. Assuming equal phase, the equilibrium position is found for $\sin(kR_0) = 0$. If the particles move away from that equilibrium position and hence $R > R_0$, the optical binding force is an attractive force pushing the particles back together. If they come closer, then eq. 72 and eq. 75 change their sign and the binding force becomes repulsive. Additionally, we can deduce from eq. 73 and eq. 76 that whenever $F_r(\boldsymbol{r}_1)$ doesn't dominate the dynamics, hence the particle is in a stable position with $\sin(kR) = 0$, $F_\varphi(\boldsymbol{r}_1)$ becomes relevant, pushing the particle towards the x-axis (perpendicular to the polarization axis) as is depicted in Figure 9b.

One interesting aspect of this result is, that for $\Delta\phi \neq 0, \pi$, the force is non-conservative. To see this, lets take a look at the force in x-direction. It corresponds to $\langle F_r(\boldsymbol{r}_{1,2})\rangle$ for $\varphi = \pm\pi/2$. Taking the Taylor Series of $\langle F_x(\boldsymbol{r}_{1,2})\rangle$ up to the first order together with the first order approximation $R = \sqrt{(R_0 + x_2 - x_1)^2 + (y_2 - y_1)^2 + (z_2 - z_1)^2} \approx R_0 \pm (x_1 - x_2)$ for $|x_1 - x_2|/R_0 \ll 1$ yields

$$\langle F_x(\boldsymbol{r}_1)\rangle \approx -\frac{|\alpha|^2 E_{0,1}E_{0,2}k^3}{8\pi\varepsilon_0\varepsilon_m R}\left[\sin(kR_0 + \phi_0) + k\cos(kR_0 + \phi_0)(x_1 - x_2)\right], \tag{78}$$

$$\langle F_x(\boldsymbol{r}_2)\rangle \approx -\frac{|\alpha|^2 E_{0,1}E_{0,2}k^3}{8\pi\varepsilon_0\varepsilon_m R}\left[\sin(kR_0 - \phi_0) + k\cos(kR_0 - \phi_0)(x_2 - x_1)\right]. \tag{79}$$

One obtains a displacement force and a force term depending on the oscillatory phase between the two particles. Neglecting the displacement term, since we are interested in the system dynamics, one can write the position dependent force in x-direction as

$$\begin{aligned}\langle F_x(\boldsymbol{r}_1)\rangle &\approx A \cdot \frac{\alpha^2 k^4}{R_0}(x_2 - x_1)\left[\cos(kR_0)\cos(\phi_0) - \sin(kR_0)\sin(\phi_0)\right],\\ \langle F_x(\boldsymbol{r}_2)\rangle &\approx A \cdot \frac{\alpha^2 k^4}{R_0}(x_1 - x_2)\left[\cos(kR_0)\cos(\phi_0) + \sin(kR_0)\sin(\phi_0)\right],\end{aligned} \tag{80}$$

with $A = E_{0,1}E_{0,2}/(8\pi\varepsilon_0\varepsilon_m)$. We can now split eq. 80 into a term with conservative coupling $\propto \cos(kR_0)\cos(\phi_0)$ and a non-conservative force term $\propto \sin(kR_0)\sin(\phi_0)$. These nonreciprocal system dynamics occur in all directions (except when the optical interaction is completely suppressed by polarization), but will in the following be investigated under more detail for the force in z-direction, which is the direction under consideration for the experimental part of this system.

3.3.2 Interaction along the optical axis

In the last Chapter we considered only the system dynamics of a particle fixed along the optical axis. Lets now consider the more realistic scenario of two particles trapped in optical tweezers and hence with non-vanishing motion in z-direction. The full derivation can again be found in appendix 6.

The dominant term of $\langle F_z(\boldsymbol{r})\rangle$ for $R \gg \lambda$ is given by:

$$\langle F_z^{int}(\boldsymbol{r}_1)\rangle \approx \frac{E_{0,1}E_{0,2}\tilde{k}k^2}{8\pi\varepsilon_0\varepsilon_m R}\alpha^2\sin^2(\varphi)\sin(kR + \phi), \tag{81}$$

$$\langle F_z^{int}(\boldsymbol{r}_2)\rangle \approx \frac{E_{0,1}E_{0,2}\tilde{k}k^2}{8\pi\varepsilon_0\varepsilon_m R}\alpha^2\sin^2(\varphi)\sin(kR - \phi). \tag{82}$$

For small differences $|z_2 - z_1|$ w.r.t. their mean distance R_0, the z-dependent part of the force induced by the interaction between the particles dipole fields and the trapping beam can be written as:

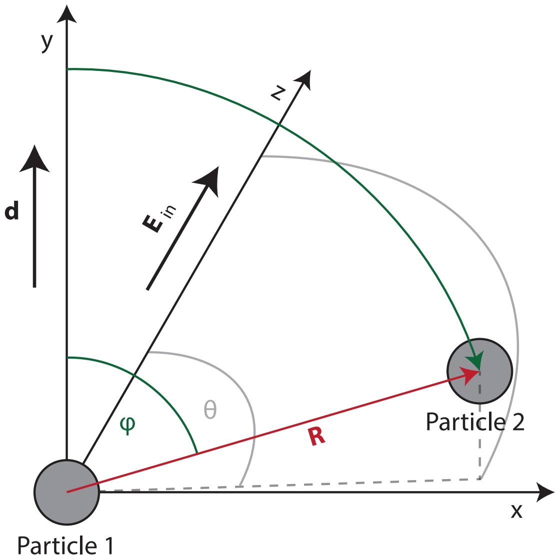

Figure 8: Coordinate system for calculating the force on particle 2, with particle 1 being positioned in the coordinate origin. The tweezer fields $\boldsymbol{E}_{in}$ are propagating parallel to the z-axis and the particles dipole moment $\boldsymbol{d}$ is oriented parallel to the y-axis. The angle between the polarization axis and the position of particle 2 is given by φ and the angle between the optical axis and particle 2 is given by θ. The coordinate system used to obtain particle 1 is in complete analogy to this one, with particle 2 instead positioned at the coordinate origin. In the results for the lateral binding $\theta = \pi/2$ has been chosen.

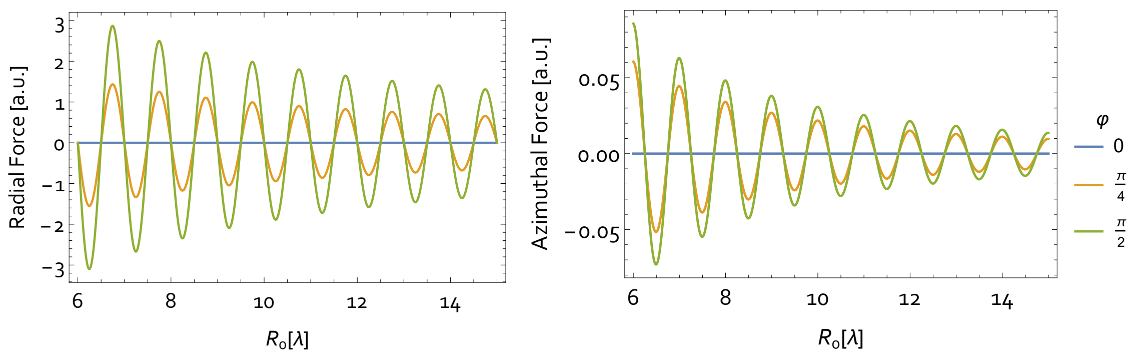

(a) Radial force $\langle F_r(\boldsymbol{r}_1)\rangle$ acting on particle 1 as a function of distance R_0 between the two particle in arbitrary units.

(b) Azimuthal force $\langle F_\varphi(\boldsymbol{r}_1)\rangle$ acting on particle 1 as a function of distance R_0 between the two particle in arbitrary units.

Figure 9: $\langle F_r(\boldsymbol{r}_1)\rangle$ and $\langle F_\varphi(\boldsymbol{r}_1)\rangle$ acting on particle 1 in the same arbitrary units, plotted for different angles φ between the particle connection axis and the polarization axis.

$$\langle F_z^{int}(\boldsymbol{r}_1)\rangle\Big|_{|z_1-z_2|\to 0} \approx A\cdot\frac{\alpha^2k^2}{R_0}\cos(kR_0+\phi_0)\left(k-\frac{1}{z_0}\right)^2(z_2-z_1), \tag{83}$$

$$\langle F_z^{int}(\boldsymbol{r}_2)\rangle\Big|_{|z_2-z_1|\to 0} \approx A\cdot\frac{\alpha^2k^2}{R_0}\cos(kR_0-\phi_0)\left(k-\frac{1}{z_0}\right)^2(z_1-z_2). \tag{84}$$

Here, $A = \sin^2(\varphi)E_{0,1}E_{0,2}/(8\pi\varepsilon_0\varepsilon_m)$ was used. Additionally, just as in Chapter 3.3.1, a displacement term $F_{1,2}^d = A\,k^2\tilde{k}\sin(kR_0 \pm \phi_0)$ alters the equilibrium position of the two particles dependent on the distance and phase between them (see appendix 6), but has been neglected as it doesn't influence the system dynamics. Figure 10 compares the z-dependent part of eq. 81 and eq. 83. We can see, that eq. 83 is a good approximation for $z_2 - z_1 \approx 0.1\lambda$.

Equations 83 and 84 can now be rewritten as

$$\begin{aligned}\langle F_z^{int}(\boldsymbol{r}_1)\rangle &\approx A\cdot\frac{\alpha^2k^2}{R_0}\left(k-\frac{1}{z_0}\right)^2(z_2-z_1)\left[\cos(kR_0)\cos(\phi_0)-\sin(kR_0)\sin(\phi_0)\right],\\ \langle F_z^{int}(\boldsymbol{r}_2)\rangle &\approx A\cdot\frac{\alpha^2k^2}{R_0}\left(k-\frac{1}{z_0}\right)^2(z_1-z_2)\left[\cos(kR_0)\cos(\phi_0)+\sin(kR_0)\sin(\phi_0)\right].\end{aligned} \tag{85}$$

This expression is similar to the interaction force in x-direction obtained in eq. 80, however, it is important to note that here, the relevant term arises from the z-dependent phase of the two oscillators while in the case of eq. 80 it was obtained because the x-axis coincides with the connection axis of the two particles and thus the derivative of R with respect to x did not vanish. However, the coupling rate is inversely proportional to the particle frequency (see eq. 94), thus making the coupling in z-direction easier to see. Using

$$\begin{aligned}k_1 &= A\cdot\frac{\alpha^2k^2}{R_0}\left(k-\frac{1}{z_0}\right)^2\cos(kR_0)\cos(\phi_0),\\ k_2 &= A\cdot\frac{\alpha^2k^2}{R_0}\left(k-\frac{1}{z_0}\right)^2\sin(kR_0)\sin(\phi_0),\end{aligned} \tag{86}$$

one can understand the force in z-direction as a combination of conservative coupling rate k_1 and non-conservative coupling rate k_2 and define the equations of motion of particle 1 and 2 as

$$m\ddot{z}_1 = -\left(m\Omega_{z_1}+k_1-k_2\right)z_1+\left(k_1-k_2\right)z_2, \tag{87}$$

$$m\ddot{z}_2 = -\left(m\Omega_{z_2}+k_1+k_2\right)z_2+\left(k_1+k_2\right)z_1. \tag{88}$$

From eq. 87 and 88 we obtain, that for $k_2 = 0$ the interaction is fully reciprocal and we obtain the same equations of motion as in Chapter 3.1. However, when $k_2 \neq 0$, the force that particle 1 exerts onto particle 2 is different from the force that particle 2 exerts onto particle 1. Therefore, by tuning the phase between the two traps, on can tune the interaction between the particles from fully reciprocal ($k_2 = 0$ when choosing $kR_0 = 0, n\pi$) to fully non-reciprocal ($k_1 = 0$ when choosing $kR_0 = n\pi/2$), where $n \in \mathbb{N}_1$.

In order to obtain the eigenfrequencies of the system, one needs to diagonalize this system of equations in analogy to Chapter 3.1. Using the same terminology as in Chapter 3.1, the eigenfrequencies are given by eq. 57:

$$\tilde{\Omega}_{1,2}^2 = \frac{k+\tilde{k}\pm\kappa}{m},$$

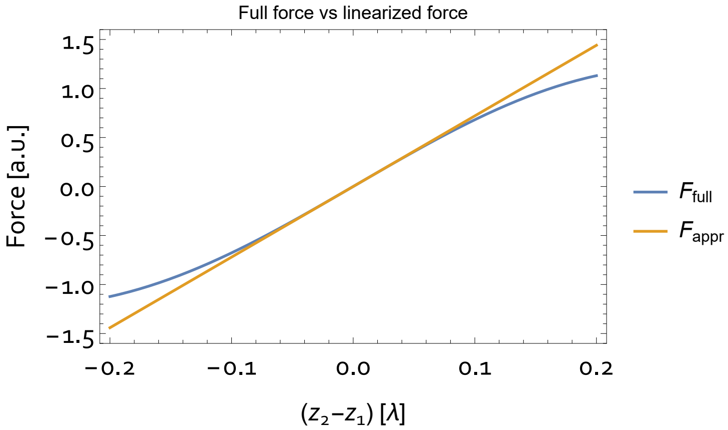

Figure 10: Comparison between the full expression for the force in z-direction in the far-field (blue) and its first order approximation (yellow) obtained for small amplitudes along the optical axis as a function of amplitude difference between the two particles.

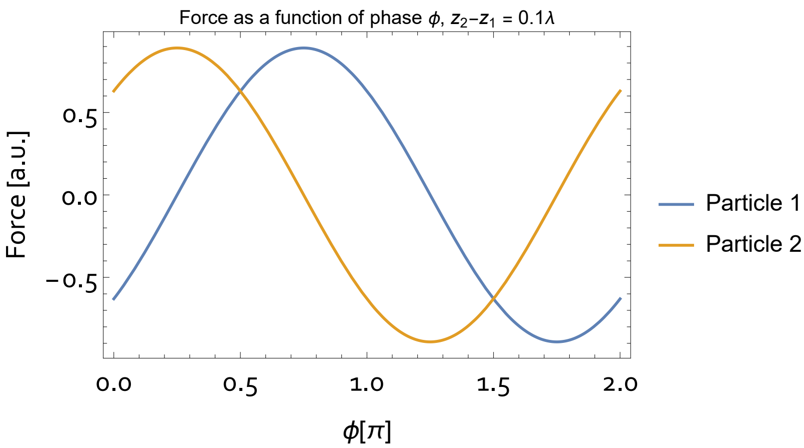

Figure 11: Linearized force in z-direction on particle 1 (blue) and particle 2 (yellow) as a function of phase difference between the two tweezers.

with $\kappa = k + k_1$ being the modified spring constant without interaction and $\kappa = \sqrt{\Delta k^2 + k_1^2 - 2\Delta k k_2}$ is obtained through diagonalisation of matrix $\boldsymbol{B}$ in eq. 52, in this case given by

$$\boldsymbol{B} = \begin{bmatrix} -\Delta k + k_2 & k_1 - k_2 \\ k_1 + k_2 & \Delta k - k_2 \end{bmatrix}. \tag{89}$$

Using $k = \frac{m}{2}\left(\Omega_{z_1}^2 + \Omega_{z_2}^2\right)$ and $\Delta k = \frac{m}{2}\left(\Omega_{z_1}^2 - \Omega_{z_2}^2\right)$ then leads to the normal modes

$$\tilde{\Omega}_{1,2}^2 = \frac{1}{2}\left(\Omega_{z_1}^2 + \Omega_{z_2}^2 + \frac{2k_1}{m} \pm \sqrt{\left(\Omega_{z_1}^2 - \Omega_{z_2}^2\right)^2 + 4\left(\frac{k_1}{m}\right)^2 - 4\left(\Omega_{z_1}^2 - \Omega_{z_2}^2\right)\frac{k_2}{m}}\right). \tag{90}$$

From eq. 90 we see, that the minimal splitting occurs for $\Omega_{z_1}^2 - \Omega_{z_2}^2 = 2k_2/m$. The eigenfrequencies of the system then become

$$\tilde{\Omega}_{1,2|_{\Delta\tilde{\Omega}=\min}} = \sqrt{\Omega_{z_1}^2 + \frac{k_1 - k_2}{m} \pm \sqrt{\frac{k_1^2 - k_2^2}{m^2}}} \approx \Omega_{z_1} + \frac{k_1 - k_2 \pm \sqrt{k_1^2 - k_2^2}}{2m\Omega_{z_1}}, \tag{91}$$

where in the last step, $k_1, k_2 \ll \tilde{\Omega}_{0,z_1}$ was assumed. This corresponds to a minimal splitting of

$$\Delta\tilde{\Omega} \approx \frac{\sqrt{k_1^2 - k_2^2}}{m\Omega_{z_1}}. \tag{92}$$

For $k_2 = 0$, the normal modes become:

$$\tilde{\Omega}_{1,2}^2(k_2 = 0) = \frac{1}{2}\left(\Omega_{z_1}^2 + \Omega_{z_2}^2 + \frac{2k_1}{m} \pm \sqrt{\left(\Omega_{z_1}^2 - \Omega_{z_2}^2\right)^2 + 4\left(\frac{k_1}{m}\right)^2}\right), \tag{93}$$

which, for $\Omega_{z_1} = \Omega_{z_2}$ is equivalent to eq. 57 of Chapter 3.1 and one retrieves the usual, conservative system dynamics for coupled harmonic oscillators with the minimal splitting giving us the conservative coupling rate g:

$$\Delta\tilde{\Omega} \overset{k_2=0}{\approx} \frac{k_1}{m\Omega} = 2g \quad \text{for} \quad k_1 \ll k. \tag{94}$$

However, for $k_2 \geq k_1$ there is no avoided crossing. The normal modes become degenerate since $\sqrt{k_1^2 - k_2^2}$ becomes imaginary if $k_2 > k_1$.

It can be useful to express the intrinsic, uncoupled frequencies Ω_{z_1} and Ω_{z_2} in terms of the trap power in order to show an avoided crossing plot in the fashion of Figure 5, since this is the experimentally tunable parameter in this setup. This can be achieved by rewriting them with regard to a center frequency Ω that corresponds to their uncoupled eigenfrequencies at equal trap power and a power detuning parameter η, such that $\Omega_{z_{1,2}}^2 = \Omega^2(1 \pm \eta)$. Doing this variable substitution changes eq. 90 to

$$\tilde{\Omega}_{1,2}^2 = \Omega^2 + \frac{k_1}{m} \pm \sqrt{\Omega^4\eta^2 + \left(\frac{k_1}{m}\right)^2 - 2\Omega^2\eta\frac{k_2}{m}}. \tag{95}$$

In order to visualize the effect of the conservative and non-conservative coupling rates k_1 and k_2 on the system dynamics, lets investigate eq. 95 under more detail. The minimal splitting is $\tilde{\Omega}_{0,z_1}^2 - \tilde{\Omega}_{0,z_2}^2 = 2\Omega^2\eta$ and hence occurs for $\eta_m = k_2/(m\Omega^2)$. As was discussed in Chapter 3.1, the sign of k_1 now determines whether the breathing mode has a higher ($k_1 > 0$) or lower frequency ($k_1 < 0$) than the center of mass mode. For $k_2 = 0$, the center of mass mode will be equal to Ω at

$\eta = \eta_m = 0$ (see Figures 12a, 12b). As can be seen in Figures 12c, 12d, adding a non-conservative coupling term k_2 shifts η_m to the right (left) for positive (negative) k_2 and decreases the minimal splitting according to eq. 91. In terms of Ω and η, this can be written as

$$\tilde{\Omega}_{1,2|_{\Delta\tilde{\Omega}=\min}} = \sqrt{\Omega^2 + \frac{k_1}{m} \pm \sqrt{\frac{k_1^2 - k_2^2}{m^2}}} \approx \Omega + \frac{k_1 \pm \sqrt{k_1^2 - k_2^2}}{2m\Omega}, \tag{96}$$

with the minimal splitting given by

$$\Delta\tilde{\Omega} \approx \frac{\sqrt{k_1^2 - k_2^2}}{m\Omega}. \tag{97}$$

Eq. 96 shows that for $\eta_m \neq 0$ and hence also $k_2 \neq 0$, the center of mass mode is shifted up (down) with respect to Ω by $k_1 - \mathrm{Re}(\sqrt{k_1^2 - k_2^2})$, depending on the sign of k_1 and the minimal splitting reduces, as can be seen from 97.

For k_2 equal or bigger than k_1, the expression under the route in eq. 95 can become negative for certain η making the normal modes degenerate. The start of the degeneracy η_i and the end η_f are positioned symmetrically around η_m and are given by

$$\eta_{i,f} = \frac{k_2}{m\Omega^2} \mp \sqrt{\left(\frac{k_2}{m\Omega^2}\right)^2 - \left(\frac{k_1}{m\Omega^2}\right)^2}. \tag{98}$$

From eq. 98 it becomes apparent that k_1 determines the beginning of the degeneracy. For $k_1 = 0$, it starts (ends) at $\eta = 0$ for $k_2 > 0$ ($k_2 < 0$) (see Figures 13a, 13b). Increasing the absolute value of k_2 means increasing the optical power difference range in which one obtains degenerate eigenfrequencies. The sign of k_1 again determines whether the degenerecy occurs at a frequency higher or lower than Ω (see Figures 13c, 13d).

This means, that by determining Ω and consequently also calibrating η through the point of crossing of the two eigenfrequencies when there's no interaction, one can determine both the conservative and non-conservative coupling rates k_1, k_2 of the system through the change of the eigenfrequencies at η_m with respect to the uncoupled system.

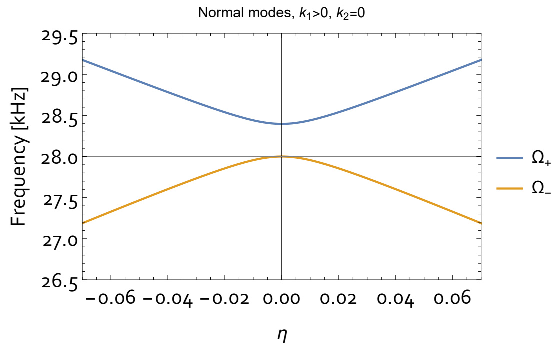

(a) Conservative coupling rate bigger zero and no non-conservative coupling rate. At $\eta_m = 0$ the breathing mode sits above the center of mass mode which precisely coincides with Ω.

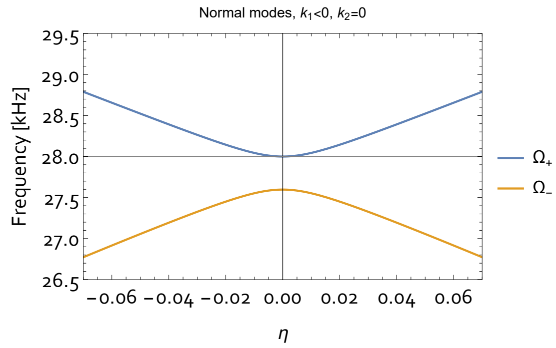

(b) Conservative coupling rate smaller zero and no non-conservative coupling rate. At $\eta_m = 0$ the breathing mode sits below the center of mass mode which precisely coincides with Ω.

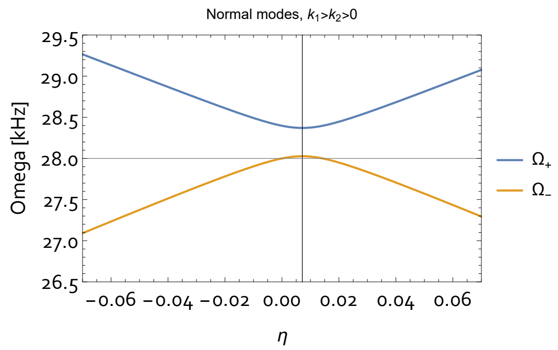

(c) Conservative and non-conservative coupling rates bigger zero. Due to $k_2 > 0$, η_m is shifted to the right. At η_m, the breathing mode sits above the center of mass mode. The modes are shifted towards higher frequencies w.r.t. Ω since $k_1 > 0$ and $k_2 \neq 0$.

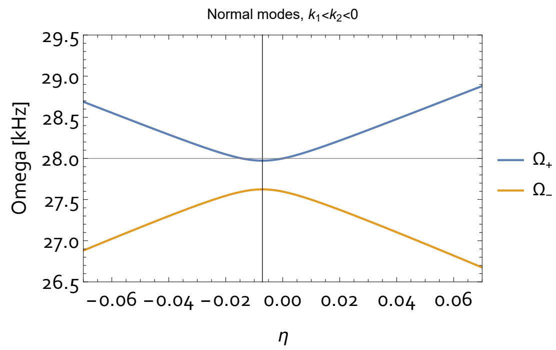

(d) Conservative and non-conservative coupling rates smaller zero. Due to $k_2 < 0$, η_m is shifted to the left. At η_m, the breathing mode sits below the center of mass mode. The modes are shifted towards lower frequencies w.r.t. Ω since $k_1 < 0$ and $k_2 \neq 0$.

Figure 12: Frequencies of the coupled systems normal mode as a function of trap power detuning η for different conservative and non-conservative coupling rates k_1 and k_2 for $k_1^2 - k_2^2 > 0$. The horizontal line indicates $\Omega = \sqrt{\left(\Omega_1^2 + \Omega_2^2\right)/2}$. The vertical line corresponds to the position of minimal splitting $\eta_m = k_2 / \left(m\Omega^2\right)$

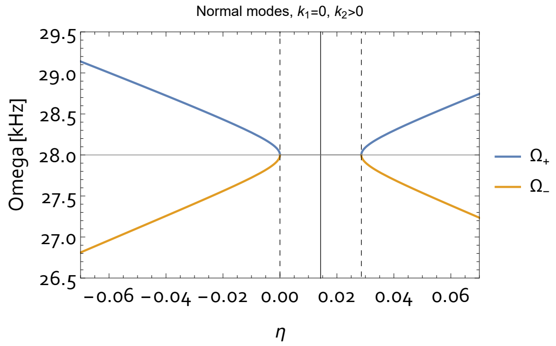

(a) Non-conservative coupling rate bigger zero and no conservative coupling rate. At $\eta = \eta_i = 0$, the normal modes become degenenerate with eigenfrequency Ω until $\eta = \eta_f$. η_m is shifted to the right since $k_2 > 0$.

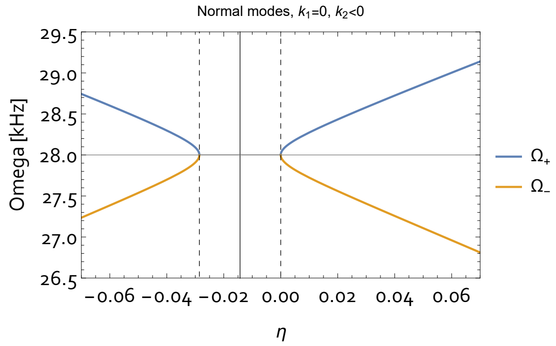

(b) Non-conservative coupling rate smaller zero and no conservative coupling rate. At $\eta = \eta_i$, the normal modes become degenenerate with eigenfrequency Ω until $\eta = \eta_f = 0$. η_m is shifted to the left since $k_2 < 0$.

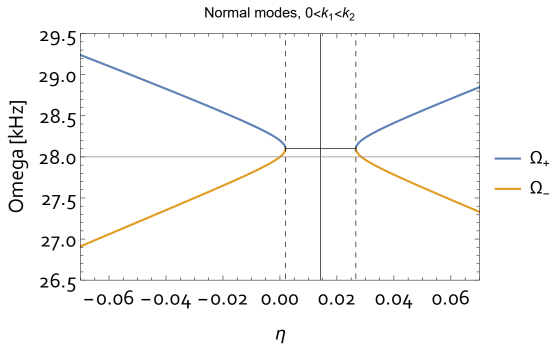

(c) Non-conservative and conservative coupling rates bigger zero. The center of the degeneracy, η_m, is shifted to the right because $k_2 > 0$. Since $k_1 > 0$, the start of the degeneracy η_i is shifted to the right, the region of degeneracy is decreased and the shared eigenfrequency is higher than Ω.

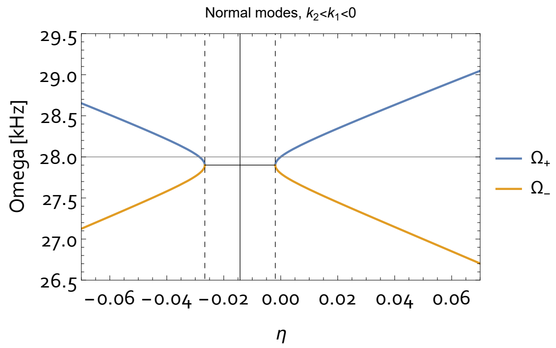

(d) Non-conservative and conservative coupling rates smaller zero. The center of the degeneracy, η_m, is shifted to the left because $k_2 < 0$. Since $k_1 < 0$, the end of the degeneracy η_i is shifted to the right, the region of degeneracy is decreased and the shared eigenfrequency is lower than Ω.

Figure 13: Frequencies of the coupled systems normal mode as a function of trap power detuning η for different conservative and non-conservative coupling rates k_1 and k_2 for $k_1^2 - k_2^2 < 0$. The horizontal line indicates $\Omega = \sqrt{\left(\Omega_1^2 + \Omega_2^2\right)/2}$. The black vertical line corresponds to the position of minimal splitting $\eta_m = k_2/\left(m\Omega^2\right)$, while the dashed vertical lines correspond to the beginning and end of the degeneracy η_i and η_f.

4 Experimental Setup

In the previous Chapter we have shown that the light induced dipole-dipole interaction leads to non-reciprocal forces between the two particles (see Chapter 3.3). In order to probe the full parameter regime, we needed to build a highly tunable setup. In the following Chapter, the different components of this setup will be explained in detail as well as calibrations and characterizations done in order to obtain its current capabilities and limits.

4.1 Setup Overview

First, we will explain the beam path in experimental setup, the optical components used as well as the electronic path in the background. Figure 14 shows a sketch of the optical path of the setup and Figure 15 the electronic path.

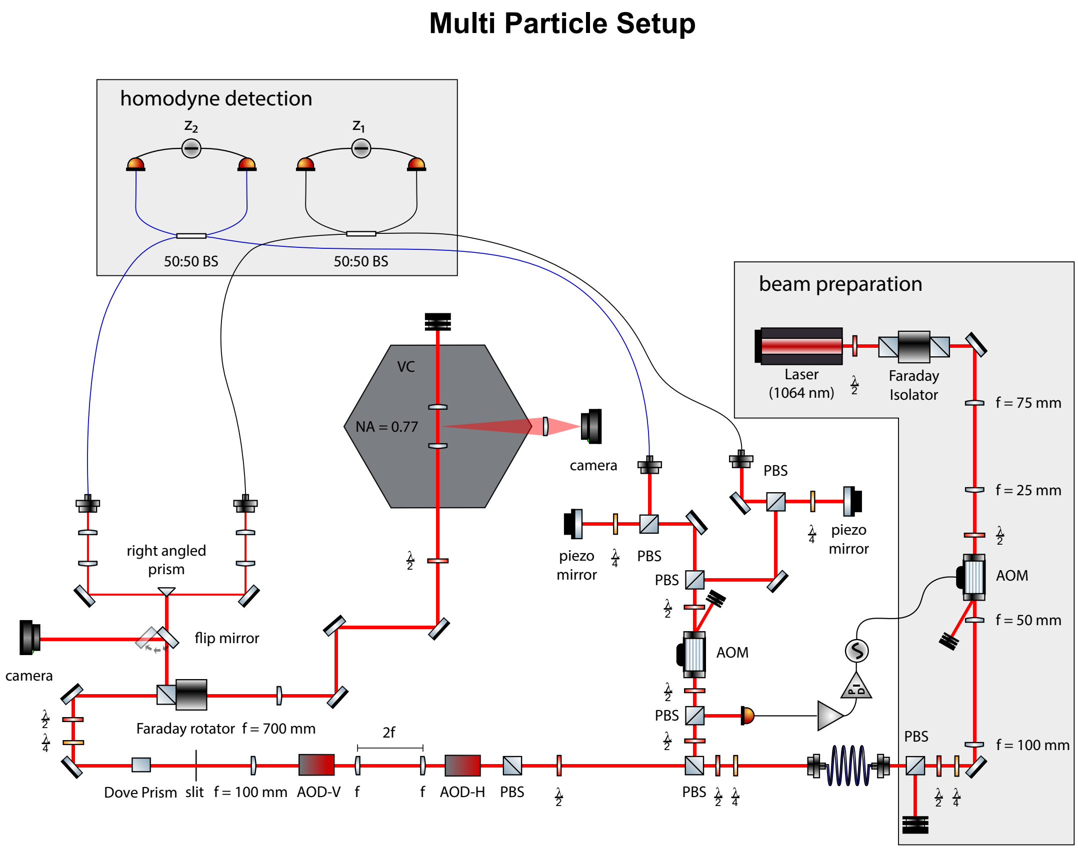

Figure 14: Sketch of the optical path of the experimental setup. In the beam preparation stage the intensity of the beam coming out of the laser head is stabilized via a PID loop. In the main stage, the traps are created using the AODs and projected into the vacuum chamber, where the particles get trapped. The light back-scattered from the particles then gets separated from the incoming beams and sent into the detection stage. There, the traps are reimaged such that the light scattered by the particles can be detected individually. It is fed into a 50:50 beamsplitter fiber and overlapped with a local oscillator that is phase locked to the signal in order to form a balanced homodyne detection.

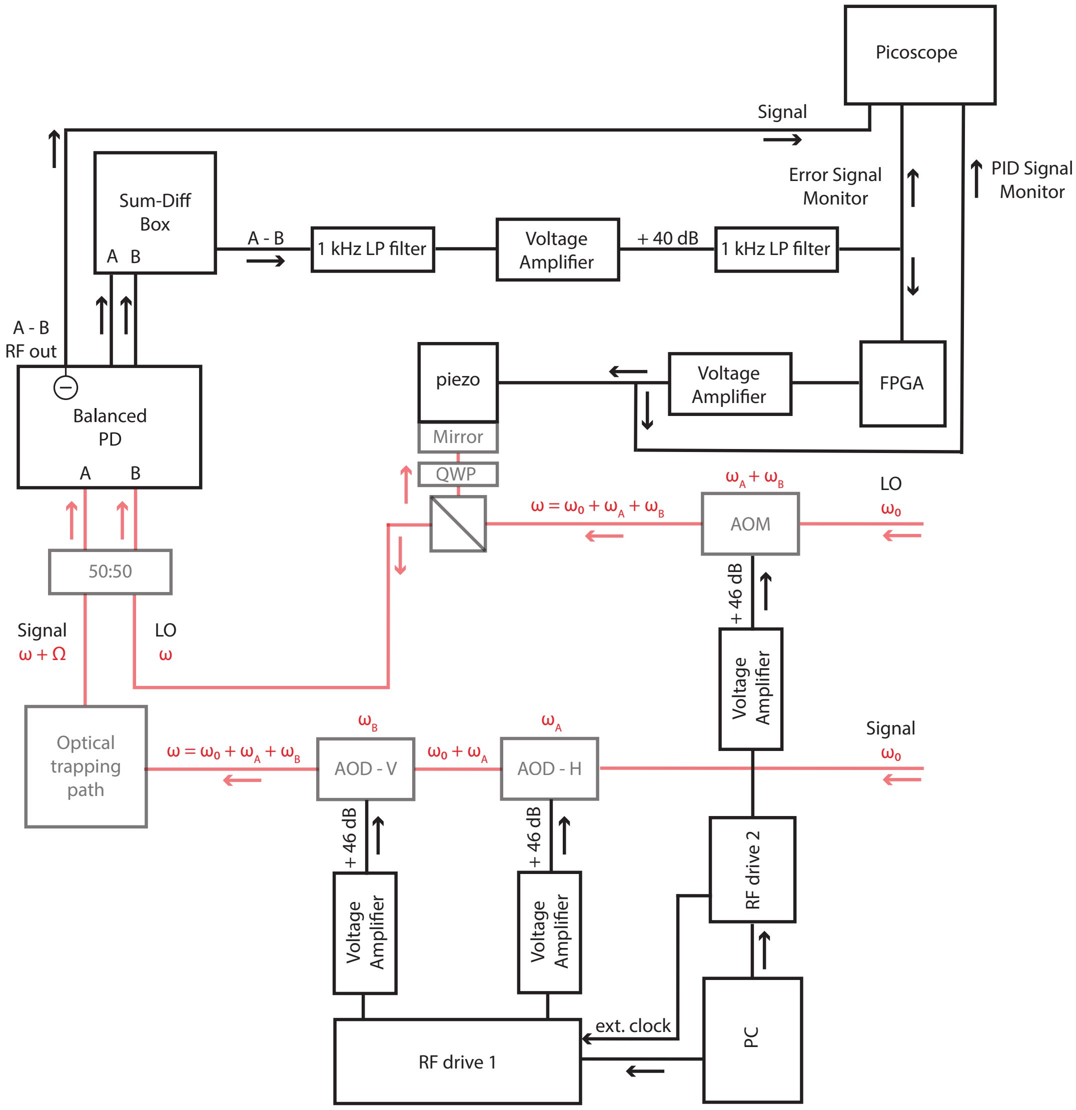

Figure 15: Sketch of the electronic path in the setup needed for the detection of one particle. The path for the second particle works equivalently, only with the frequency shifts ω_A and ω_B exchanged between the two AODs. The black components correspond to electronic parts and connections, the gray components are optical and the red paths correspond to the laser beam. The signal beam enters the drawing with frequency ω_0. Through the two AODs it gets RF frequencies $\omega_A + \omega_B$ imprinted on top. By guiding the local oscillator through an AOM that is driven with RF frequency $\omega' = \omega_A + \omega_B$ RF frequencies $\omega_A + \omega_B$ are added onto its original frequency ω_0 as well, such that the frequencies of the signal and the LO beam are the same if no particle is present. The clock of RF drive 2, that drives the AOM, is also used for the RF drive 1 that drives the two AODs. Signal and LO get combined in a 50:50 fiber beamsplitter and each end is plugged into one of the inputs of the balanced photodetector. The RF output port consists of the AC part of the two signals subtracted from each other. This port is directly connected to the picoscope and used for measurement of our particle signal. The other ports of the balanced PD are connected to the sum-diff box, which subtracts the two signals. After a 1 kHz lowpass filter a voltage amplifier and another1 kHz lowpass filter, the resulting signal gets split into two, in order to obtain an error signal monitor that can be plugged into the picoscope. The actual error signal is connected to an FPGA used as a PID. After another voltage amplifier, the output of the FPGA is then connected to a piezo stack glued onto a mirror of the interferometer in the local oscillator path.

4.1.1 Beam preparation stage

As a light source a 1064 nm coherent laser source (Innolight Mephisto) was used together with a 20 W amplifier (Azur Light ALS-IR-1064-20-A-CC-SF). In the first stage, the laser goes through a half-waveplate and a Faraday isolator, which acts as a light valve, allowing light of a certain polarization to only travel in one direction. This circumvents any back-reflections to be fed back into the laserhead, which could otherwise damage it.

Next, a telescope with magnification $M = 1/3$ decreases the size of the beam to approximately 1 mm such that it fits through the AOM (Gouch & Housego 3110-197). The AOM (Acousto Optic Modulator) modulates part of the beam into its first diffraction order (diffraction efficiency approximately 80% at maximal input power), such that the intensity of the remaining beam can be kept stable through a feedback loop (see Chapter 4.3).

Afterwards, the beam size is increased again with a second telescope ($M = 2$) and sent through a half- and quarter waveplate and a PBS (polarizing beamsplitter) before part of the beam is sent to a beam dump and the rest is coupled through a single mode fiber that leads to the main part of the setup (approximately 3.5 W).

We use the fiber instead of directly connecting the beam preparation stage with the main setup has two reasons. First of all, the laser head outputs a Gaussian mode with some speckles, so the fiber acts as a mode cleaner that cleans the input beam from its speckles that would otherwise modify the trapping potential. Secondly, the output of the laserhead is not collimated but focuses after around 1.5 m. However, the focal length changes with temperature and therefore, one needs to build a telescope that needs constant adjustment in order to have a nicely collimated beam. Introducing a fiber means that the coupling efficiency will decrease if the beam size at the input changes and doesn't match the fiber mode anymore. However, the output mode will always be collimated and aligned with the optics. Changing the telescope to increase the coupling efficiency thus only affects the output power, but not the quality of the collimation or the alignment, in contrast to the free-space case.

The coupling efficiency into the fiber is approximately 65% and another 10% of the total input power is lost since the fiber is connected to a second fiber via a mating sleeve. The reason for the high loss at the input of the fiber stems from the already mentioned Gaussian mode with some added speckles that the laser head puts out. Since single mode fibers are optimized to only let a TEM00 mode pass, this leads to an artificially low coupling rate.

4.1.2 Trap generation

After the beam leaves the fiber through the collimator (Thorlabs F240APC-1064) a fraction of it gets redirected via a quarter and a half waveplate followed by a PBS. Part of the beam is used as a reference for the intensity stabilization (see Chapter 4.3) and the rest is used to create two local oscillators that are phase locked to the light scattered by our particles to create a homodyne detection (see Chapter 4.1.3).
Finally, the remaining beam (approx. 2.3W) is sent first through a horizontally mounted AOD (AA Opto-Electronic DTSXY-400) followed by a 1 : 1 telescope and a vertically mounted AOD (Acousto Optic Deflector) (see Figure 16).

The AODs consist of a TeO_2 crystal and a piezo-electric transducer that converts an electric RF (radio frequency) input signal into an acoustic wave that deflects the incident laserbeam if the wavelength matches the Bragg-condition $2\Lambda\sin(\theta) = n\lambda$, where θ is the angle of incidence, $\Lambda = 2\pi c_s/\omega_s$ corresponds to the acoustical wavelength, λ to the optical, c_s to the speed of sound and $n \in \mathbb{N}_1$ corresponds to the diffraction order. If the beam is deflected, the momentum of the acoustic wave gets imprinted onto the optical wave, changing the frequency of the diffracted beam to $\omega_n = \omega_0 \pm n \cdot \omega_s$, where n is the diffraction order and the sign corresponds to a positive or negative diffraction order (the beam either absorbs or emits a phonon). By varying the input RF tone $\Delta\omega_s$, one changes the grating distance which then modulates the output angle $\Delta\theta$ of the individual diffraction orders according to

$$\sin(\Delta\theta) \approx \Delta\theta = \frac{n\lambda}{2\Delta\Lambda} = \frac{n\lambda\Delta\omega_s}{4\pi c_s}. \tag{99}$$

A horizontally oriented AOD diffracts the input beam in horizontal direction and similarly for a vertically oriented AOD. This means that using horizontally and vertically oriented AODs together allows to diffract the input beam in an arbitrary direction with respect to the optical axis [42]. By driving the AODs with multiple RF tones at once, one can thus create two-dimensional beam arrays (see Figures 17, 16).

In this setup, we drive the first AOD with two RF tones A and B (frequencies ω_A and ω_B) and align it such that we have maximal diffraction efficiency in the first positive order ($\approx 94\%$, see Chapter 4.2.1 for AOD calibration). After the beam has passed the AOD, we remove the unmodulated 0th order with a D-shaped mirror to deflect it away from the beam path and onto a beam dump. We have created two first diffraction orders, horizontally separated by $\Delta x \approx \Delta\theta$, where Δx is the distance from the AOD and $\Delta\theta \ll 1$. By guiding these first diffraction orders through a 1:1 telescope into the second, vertically oriented AOD, the crystal inside the first AOD is imaged into the second one, allowing for maximal diffraction efficiency in both first orders inside the second AOD as well as precise mapping between Δx and $\Delta\theta$ in both spatial dimensions.

We then apply two RF tones, C and D, to the second AOD which creates four diverging beams in the first diffraction order (diffraction efficiency of the second AOD $\approx 92\%$). Each first diffraction order, with frequencies ω_A, ω_B created by deflection in the first AOD, gets deflected by each tone in the second AOD, which results in four output beams with different frequencies

$$\omega_{A,C} = \omega_0+\omega_A+\omega_C, \qquad \omega_{A,D} = \omega_0+\omega_A+\omega_D, \qquad \omega_{B,C} = \omega_0+\omega_B+\omega_C, \qquad \omega_{B,D} = \omega_0+\omega_B+\omega_D.$$

In principle, one can create arbitrarily sized two dimensional arrays. However, in reality one is limited by the laser power, since each trap still needs to have enough power to trap particles (see Chapter 2.2.2). Figure 17 shows a 10x10 array on a detector card positioned in the focal plane behind the AODs and created by driving each AOD with ten different RF tones.

By choosing equal frequencies in both AODs, such that $\omega_A = \omega_C$ and $\omega_B = \omega_D$, the parts of the beam that get diffracted first by A and then by B or vice versa are of equal frequency, since they both get the frequency of each tone added once onto their original frequency. Therefore, by choosing the off-diagonal traps shown in Figure 16 and mapping the AOD crystals onto the trapping lens of the optical tweezer, one can thus create a 1D trap array of equal optical frequencies that are individually movable along the focal plane, with the distance proportional to the change in driving frequency ω_s and the magnification of the telescope. Additionally, by changing the phase and power of the drive frequencies, one can also individually modify the phase and potential depth of each trap, allowing for versatile, programmable interaction between the trapped particles.

In order to map the crystals onto the trapping lens while overfilling it, two lenses with focal length

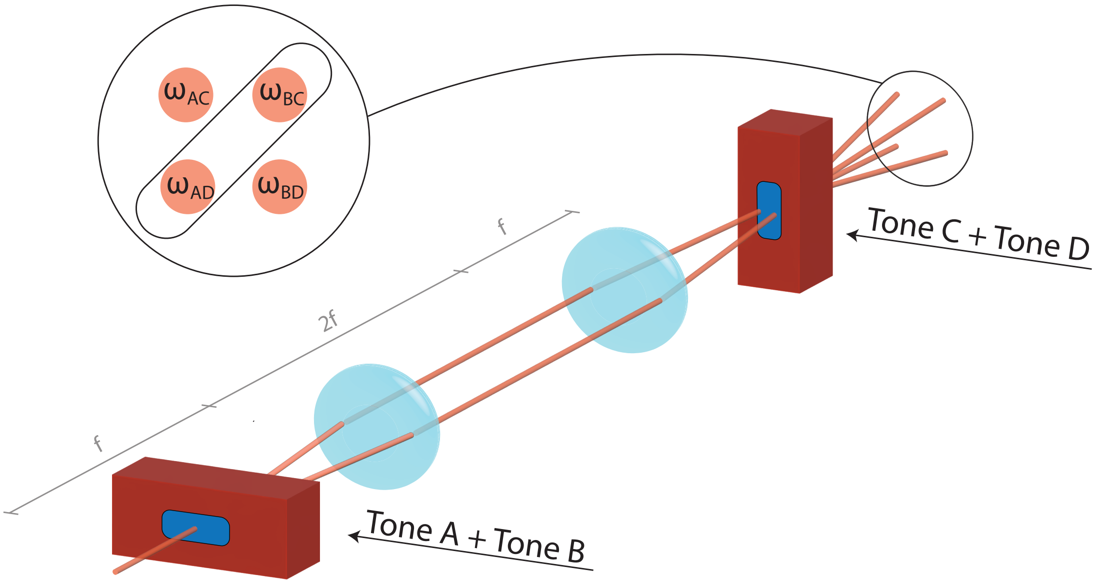

Figure 16: Sketch of the AOD (Acousto Optic Deflector) arrangement used for the trap array generation. The first AOD is driven with two RF tones A, B of different frequencies, creating two first diffraction orders under different angles along the horizontal plane. The zeroth order is not displayed in this sketch. A 1:1 telescope images the created traps into the second AOD after a distance $d = 4f$ ($f = 50$ mm). The second AOD is driven with two RF tones C, D and diffracts both of the input laser beams under two different angles along the vertical plane. If one sets equal frequencies of the RF tones ($\omega_A = \omega_C$ and $\omega_B = \omega_D$) for both AODs, then the trap generated by the diffraction through tones A and D will have the same frequencies as the trap generated by diffraction through tones B and C ($\omega_{A,D} = \omega_{B,C}$). They correspond to the encircled off-diagonal beams in the close up.

Figure 17: Picture of a 10× 10 trap array on a detector card, taken in the focal plane behind AODs. It was created by driving both AODs with ten different RF tones each separated by 1 MHz.

$f_1 = 100$ mm and $f_2 = 750$ mm are positioned in the beam path, with the first being at a distance f_1 to the second AOD and the second lens at a distance $f_1 + f_2$ to the first lens. Positioning the trapping lens (LightPath 355330) $\approx f_2$ behind the second lens means that this system creates a telescope with magnification M = 7.5 that projects the image created inside the AODs onto the trapping lens. In the focal plane of the first lens after the AOD, one can therefore see an amplified image of the traps in the tweezer plane. We use a movable slit in there in order to block the diagonal traps, such that only the off-diagonal traps of equal frequencies remain. A dove prism later in the beam path rotates them by 45°, such that they lie horizontally in the trapping plane.

In front of the trapping lens, another half waveplate allows us to tune the polarization of the linearly polarized input beams, such that the optical interaction of the particles in the trap can be tuned (see Chapter 3.3.2). The trapping lens (NA = 0.77) then focuses the collimated incident beams to two tightly focused beams with beam waist $w_0 \approx 1\,\mu$m. A camera (Thorlabs CS165CU) is mounted outside the vacuum chamber in front of the window orthogonal to the optical axis. It is used to monitor the traps, such that one can not only determine whether one has trapped but also determine the polarization inside the trap. Since a dipole radiates maximally in the axes orthogonal to its polarization, optimizing the amount of light radiated by the particles lets us roughly deduce the polarization in the focal plane.

4.1.3 Detection path

In order to detect the particles motion, we implement a *balanced homodyne detection*. In this scheme, the overlap the light field scattered by the particle $E_s = \mathrm{Re}\left(\xi_s e^{i\omega t}\right)$ and a strong coherent beam of equal frequency, referred to as local oscillator, $E_{LO} = \mathrm{Re}\left(\xi_{LO} e^{i(\omega t + \phi_{LO}))}\right)$, where ϕ_{LO} corresponds to the phase difference between local oscillator and signal beam, on a 50:50 beamsplitter. The complex output amplitudes of the two beamsplitter ports then are

$$\xi_{out,1} = \frac{1}{\sqrt{2}}\left(\xi_s e^{i\omega t} + \xi_{LO} e^{i(\phi_{LO}+\omega t)}\right),$$

$$\xi_{out,2} = \frac{1}{\sqrt{2}}\left(\xi_s e^{i\omega t} - \xi_{LO} e^{i(\phi_{LO}+\omega t)}\right).$$

The signal measured on the photodetectors then corresponds to

$$I_1 = \eta \cdot |\xi_{out,1}|^2 = \frac{\eta}{2}\left(|\xi_s|^2 + |\xi_{LO}|^2 + \xi_s \xi_{LO}^* e^{-i\phi_{LO}} + \xi_s^* \xi_{LO} e^{i\phi_{LO}}\right),$$

$$I_2 = \eta \cdot |\xi_{out,2}|^2 = \frac{\eta}{2}\left(|\xi_s|^2 + |\xi_{LO}|^2 - \xi_s \xi_{LO}^* e^{-i\phi_{LO}} - \xi_s^* \xi_{LO} e^{i\phi_{LO}}\right),$$

where η corresponds to the quantum efficiency of the detected signal. Subtracting the two signals from each other eliminates the terms corresponding to $|\xi_s|^2$ and $|\xi_{LO}|^2$. Making the approximation $\xi_{LO} = |\xi_{LO}|$, which is justified for a strong coherent beam, since its mean amplitude is much higher than its fluctuations, only leaves

$$I_{BH} = I_1 - I_2 = \alpha |\xi_{LO}| \left(\xi_s e^{-i\phi_{LO}} + \xi_s^* e^{i\phi_{LO}}\right) = \alpha\sqrt{2} X(\phi_{LO}, t).$$

Here, $X(\phi_{LO}, t)$ is the angle dependent quadrature of the signal. For $\phi_{LO} = 0$, $X(0, t)$ corresponds to the amplitude quadrature and for $\phi_{LO} = \pi/2$ to the phase quadrature. By tuning the phase difference between the signal and the local oscillator, one can thus measure any arbitrary optical quadrature using a homodyne detection scheme. Additionally, the amplitude of the signal strongly depends on the strength of the local oscillator $|\xi_{LO}|$, thus allowing to measure even very small signals [43].

In our setup, we collect the light that the particles scatter back into the trapping lens which has the particles motion along the z-axis imprinted onto its phase to use as our signal. We chose to collect the back-scattered (and not the forward-scattered) light, because even though a dipole radiates equally in all directions orthogonal to the polarization axis (see Chapter 2.2), the information content about the z-motion (optical axis) of the light collected in the backplane is about 90% of the total information on the particles position along this axis [44]. We use a Faraday rotator and a PBS to split off the back-scattered light from the beam path and into the detection arm (see Figure 14).

A right-angled prism, positioned such that it is in the image plane of the traps, splits the light scattered from the two particles and directs them towards single-mode 50:50 fiber beamsplitters. The beamsplitter fiber tips are aligned in a 4f configuration with the right-angled prism and mounted on a 3-axis translation stage in order to optimally mode-match the imaged dipole field inside the trap with the fiber mode [3]. This is a fiber based adaptation of a confocal detection scheme [45] which filters out back-scattered reflections from the optical components along the beam path, thus allowing us to increase the information content of the collected light over the detection background. The collected back-scattered light is then overlapped in the fiber beamsplitter with a local oscillator of equal frequency in order to form a balanced homodyne detection.

To create the local oscillator, we pick off a part of the laser light after the beam preparation stage with a half-waveplate and a PBS (see Figure 14). Since the optical frequencies given by the RF tones ω_A and ω_B in the AODs are added on top of the laser frequency ω_0 (see Chapter 4.1.2), we need to add these frequencies onto the local oscillator as well if we wish to create a homodyne detection. To this end, we drive an AOM (Gouch & Housego 3110-197) with the sum of the two RF tones $\omega_A + \omega_B$ and use the first diffraction order as our local oscillator (diffraction efficiency $\approx 80\%$). The RF sources used to drive this AOM and the AODs share the same clock (generated by the AOM RF source Tabor Electronics LS3084R 13GHz), as can be seen in Figure 15, thus ensuring that the output frequencies are equal. Then, the beam gets split again since we need two local oscillators in order to have a homodyne detection for each of our two particles motions. We modulate the phase of each oscillator with a piezo-driven mirror (Thorlabs PK44M3B8P2) in order to phase lock the local oscillators to the particle signals (see Figure 14). Finally, the local oscillators both get coupled into one end of the single mode fiber 50:50 beamsplitters, where they get overlapped with the signals collected from the particles. The two outputs of each 50:50 beamsplitter are plugged into a balanced photodetector (Thorlabs PDB425C-AC). The RF output port of the balanced photodetector subtracts the AC components of the two beamsplitter outputs. This port is directly connected to a data acquisition card (PicoScope 5444D) to store the particle motion on a computer. The other output ports of the balanced PD correspond to the detected signals of the two inputs and are also subtracted using homebuilt electronics. The resulting signal is then sent through a 1 kHz lowpass filter, followed by a voltage amplifier (Femto DHPVA) and a second 1 kHz lowpass filter. This ensures that unwanted high frequency noise doesn't compromise the locking quality. The signal is split into two, with one arm serving as a monitor for the error signal. The second arm is connected to an FPGA (Red Pitaya 125-14) that is programmed as a PID. The output of the FPGA is amplified and connected to the piezo stack in the interferometer arm of the local oscillator. Figure 15 shows the locking scheme as described above. For details about the detection characterization, see Chapter 4.2.3.

Additionally, before the right angled prism splits the two emitted light fields, a flip mirror allows us to instead image the trapping sites into a second camera (Thorlabs CS165CU). We use it to resolve the number of trapped particles, since this is impossible to do with the previously mentioned camera (see Chapter 4.1.2) and with the spectrum of the particle motion at high pressure. Figure 18 shows an image of four trapped particles, which was possible as the slit was open.

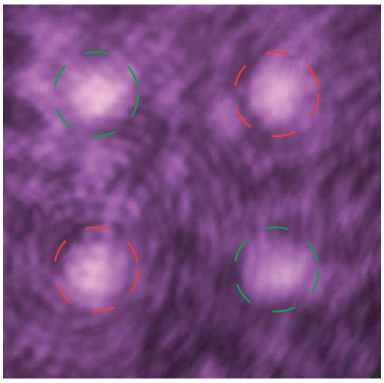

Figure 18: Camera image of 2x2 particles trapped. The camera collects the light back-scattered from the particles. It is positioned such that the trap image is focused onto the camera sensor. The two particles encircled in green are trapped in the diagonal traps which have different trap frequencies, while the particles encircled in orange are trapped in the off-diagonal traps of equal trap frequencies.

4.2 Calibration and characterization

4.2.1 Calibration of the AOD input and output

The AODs (AA Opto-Electronic DTSXY-400) are essential in creating the individually tunable traps that we need in order to generate programmable interactions between our particles. Therefore, calibrating them such that we know exactly what response to expect from tuning each parameter is crucial. The three parameters needed to calibrate are

- amplitude of the RF output
- phase relative phase between the RF outputs
- diffraction efficiency of the AODs as a function of the RF drive.

To drive the AODs, an Arbitrary Waveform Generator (AWG) featuring a PCIe interface (Spectrum Instrumentation M4i.6631-x8) is used. It has a 16-bit resolution and allows for a streaming speed of up to 2.8 GB/s and 1.25 GS/s per channel. Its Application Programming Interface (API) can be accessed and programmed using various programming languages, in this case the control script was written in Python. The control program (previously provided) allows for tuning the number of RF tones per channel (each channel is used to drive one AOD), their frequencies, amplitudes and phases. Additionally, the frequencies of each channel can automatically be moved using arbitrary step sizes. This is an important tool in order to move the traps without losing the particles or having to set each step by hand.

In the scope of this thesis a couple of extensions were added to the program such as the ability to also do automatic amplitude and phase sweeps in arbitrary step sizes. Furthermore, the possibility to adjust the delay between each step was added. Also, the frequencies, amplitudes and phases can now be moved individually, while previously it was only possible to change them all by the same absolute amount. Finally, the option to automatically acquire data while scanning any of the above parameters has been implemented.

Amplitude calibration

We monitor the output of the AWG with an oscilloscope and observe that there is an amplitude difference between the set and the actual output voltage which increases with increasing amplitude. We record output of the AWG for a certain input over several milliseconds and fit it with

$$A \cdot \sin(\omega t + \varphi) + c, \tag{100}$$

from which we extract the amplitude A. We vary amplitudes from 60 mV to 120 mV in steps of 20 mV and frequencies between 70 MHz and 76 MHz in steps of 1.5 MHz. The frequency and amplitude steps have been chosen such that they cover the region in which we later want to use the AODs. Note that the maximum diffraction efficiency for the AODs is given at an input of 130 mV if driven with one tone.

Figure 19a shows the relative amplitude difference $(A_{in} - A_{out})/A_{in} = \Delta A/A_{in}$ as a function of frequency. It shows a decrease in output amplitude depending on the input amplitude and frequency, with a minimal relative amplitude difference of $\Delta A_{min}/A_{in} > 17\%$ within the measured range. At a fixed frequency, the relative amplitude difference deviates only up to $\pm 2\%$ from its mean value $\langle \Delta A/A_{in} \rangle$ when changing the input amplitude. That is why the average relative amplitude difference per frequency was used for the amplitude deviation fit as a function of frequency. As can be seen from Figure 19b, the increase in relative amplitude vs frequency f is fairly well approximated with a linear function:

$$\frac{A_{in} - A_{out}}{A_{in}} = k(f - f_{min}) + d,$$
$$\text{with} \qquad k = 27 \cdot 10^{-4} \pm 2 \cdot 10^{-4}, \qquad d = 0.17 \pm 1 \cdot 10^{-3}. \tag{101}$$

Using eq. 101 one can then obtain a function transforming an input A_{in} to a corrected input A'_{in} by setting $A_{in} \to A'_{in}$ and $A_{out} \to A_{in}$ in eq. 101:

$$A'_{in} = \frac{A_{in}}{1 - (fk + d)}. \tag{102}$$

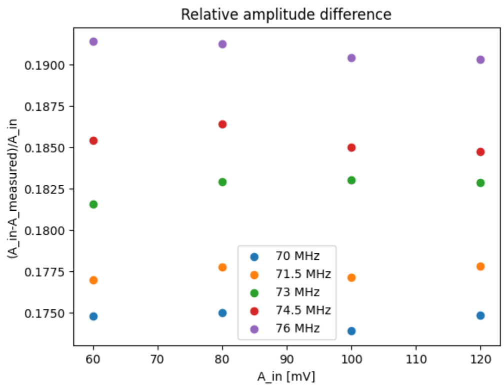

(a) Difference between amplitude set on the AWG A_{in} and the actual amplitude A_{out} of the signal divided by A_{in} without correction. The different colors stand for the different frequencies for which the amplitudes were measured. While the relative deviation of the output signal seems to be independent of the input amplitude, it does depend on the frequency of the sine wave the AWG creates. The errors of the amplitudes extracted from the fits are too small to be resolved.

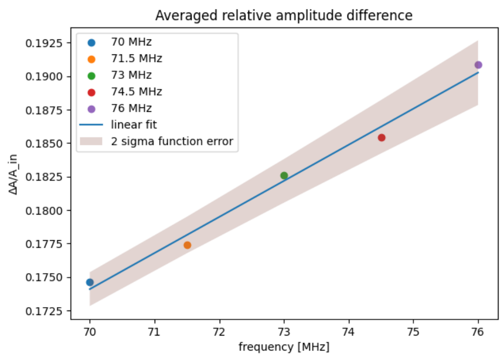

(b) Relative amplitude difference averaged over all amplitudes for each frequency without correction, plotted against the frequency and fitted with a linear function. The higher the frequency, the stronger the deviation from the desired output amplitude. The gray area corresponds to two times the standard deviation of the fit function error.

Figure 19: Relative measured amplitude difference $\Delta A/A_{in} = (A_{in} - A_{out})/A_{in}$ for different A_{in} and frequencies **without correction**.

Figure 20a shows the relative amplitude difference $\Delta A/A_{in}$ as a function of the desired (input) amplitude for the same values as in Figure 19a after the correction factor was added. We can see, that the frequency dependence that was visible in Figure 19a has been suppressed. Taking the average amplitude deviation for each frequency shows that the correction is slightly more successful for higher frequencies than for lower ones. However, the maximal deviation from the desired output has been reduced to $\Delta A_{max}/A_{in} < 0.2\%$.

Phase calibration

In order to make sure that the phase that set by the AWG also corresponds to the phase set in the program, a phase calibration was performed as well. This is important, because the phase of

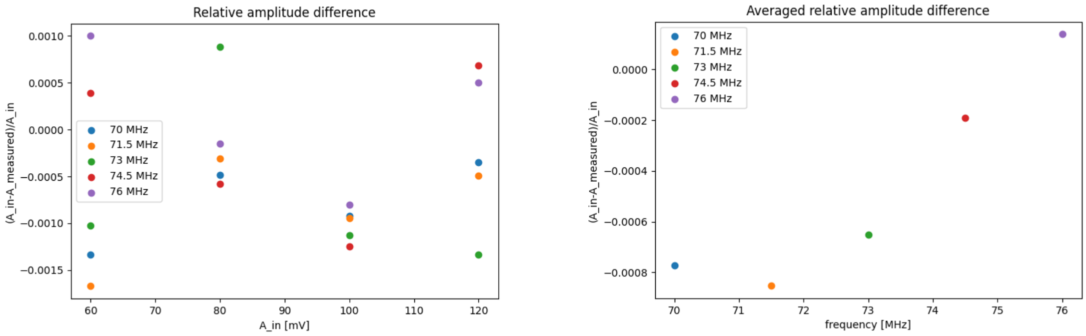

(a) Difference between amplitude set on the AWG A_{in} and the actual amplitude A_{out} of the signal divided by A_{in} after the correction. The different colors stand for the different frequencies for which the amplitudes were measured. The errors of the amplitudes extracted from the fits are too small to be resolved.

(b) Relative amplitude difference averaged over all amplitudes for each frequency after the correction, plotted against the frequency.

Figure 20: Relative measured amplitude difference $\Delta A/A_{in} = (A_{in} - A_{out})/A_{in}$ for different A_{in} and frequencies **after the correction**.

the RF tone provides a phase offset to the optical phases and hence effectively changes the relative phase between the light coherently scattered off the two trapped particles.

To calibrate the phase difference between the RF tones fed to the two AODs, a phase scan in steps of 20° for three different frequencies (70 MHz, 73 MHz, 76 MHz) has been performed in one of the two channels while leaving the other one unchanged. The results can be seen in Figure 21, revealing a constant change in phase difference $\Delta\phi$ with respect to the input phase that has a slight offset. Since the output phase difference $\Delta\phi_{out}$ is constant with frequency within 0.3% (see Figure 21), the values gathered using the central frequency f = 73 MHz have been used to perform the linear fit seen in Figure 21a. This reveals a response of the AWG according to

$$\begin{aligned} \Delta\phi_{out} &= k\Delta\phi_{in} + d, \\ \text{with} \qquad k &= 1 \pm 1 \cdot 10^{-4}, \qquad d = 7.65° \pm 0.03°. \end{aligned} \tag{103}$$

The output phase change reacts linearly to the input phase ($k = 1 \pm 1 \cdot 10^{-4}$). Removing the constant offset by adding -d to the output phase then yields a 1:1 response of input and output phase difference with a maximal deviation of 0.25° for f = 73 MHz, which corresponds to less than 0.1 % (see Figure 22b). The fitted coefficients after the correction are

$$k = 1 \pm 2 \cdot 10^{-4}, \qquad d = -0.06° \pm 0.04°,$$

which implies that phase changes between the two input Channels can be performed with an accuracy of over a tenth of a degree, which is more than sufficient for the types of experiments that will be performed on this setup.

AOD diffraction efficiency measurement

After assuring that the AWG gives the expected output, the signal is amplified and then connected to the AODs. Since the first diffraction order of the AODs is later used for the trap generation, one wants its diffraction efficiency to be as high as possible over a certain frequency

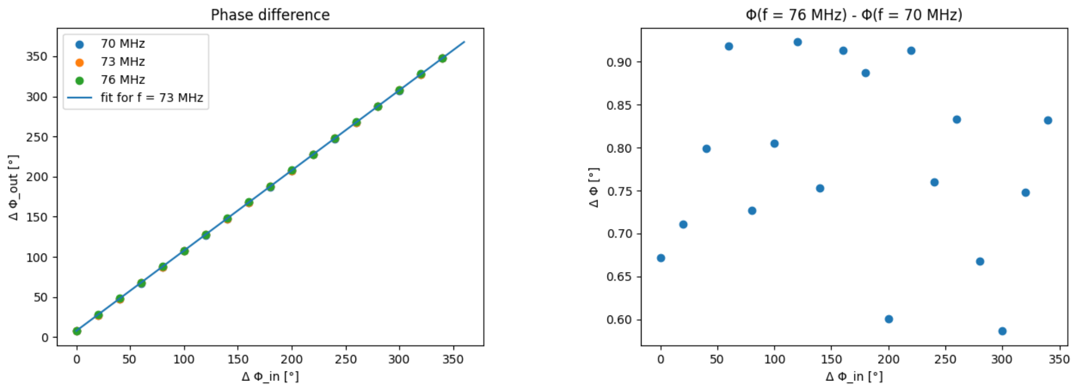

(a) Output phase ϕ_{out} plotted against the desired phase ϕ_{in} and fitted for f = 73 MHz using a linear function. The different colors stand for the different frequencies for which the phases were measured. We observe, that the output phase changes linearly with the input phase, there is only a slight constant offset d = $7.65° \pm 0.3°$. The errors from the phase differences extracted from the fits as well as the error from the fitting function are too small to be resolved.

(b) Output phase difference $\Delta\phi_{out}$ between a signal of f = 76 MHz and f = 70 MHz for variable input phases. The difference between the two outer frequencies have been chosen because ϕ(f = 70 MHz)< ϕ(f = 73 MHz)< ϕ(f = 76 MHz) and hence this serves as an estimate of the maximal frequency dependency of the output phase in the desired region. Even though the offset is higher for higher frequencies, the difference never exceeds 1°, which corresponds to an error of less than 0.3%.

Figure 21: Phase calibration measurement. Output phase difference $\Delta\phi_{out}$ vs. input phase difference $\Delta\phi_{in}$ is plotted for different frequencies **without correction**.

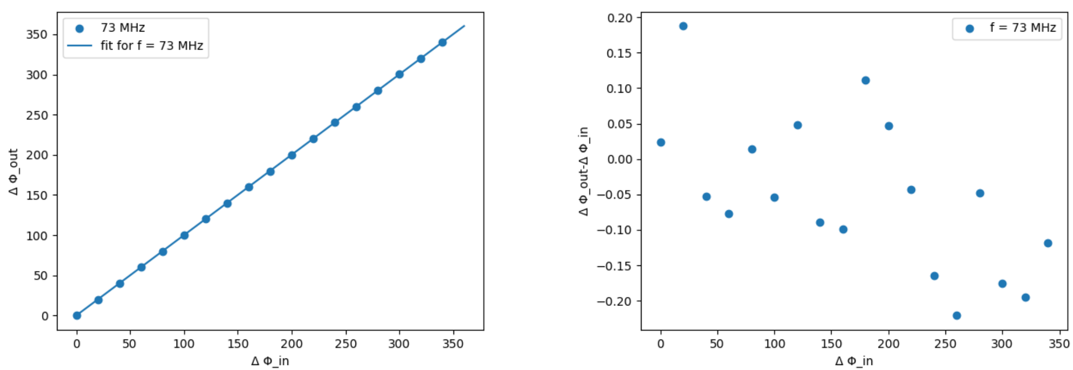

(a) Output phase ϕ_{out} plotted against the desired phase phase ϕ_{in} and fitted for f = 73 MHz using a linear function. The errors from the phase differences extracted from the fits as well as the error from the fitting function are too small to be resolved.

(b) Phase difference between the input and output phase difference at f = 73 MHz. The difference in input vs output is now always smaller than 10^{-3}%.

Figure 22: Phase calibration measurement. Output phase difference $\Delta\phi_{out}$ vs. input phase difference $\Delta\phi_{in}$ is plotted for f = 73 MHz **after the correction**.

range which corresponds to the range in which the traps should be able to move. To characterize how a certain input frequency translates to an optical output intensity, first the diffraction efficiency of the first (horizontal) AOD is measured between 60 MHz and 86 MHz in steps of 500 kHz (see Figure 23a) at 130 mV amplitude, which we found yields the highest diffraction efficiency in the experiment. Then, with the first AOD deflecting light through the central frequency of 73 MHz, the same measurement is done for the second (vertical) AOD (see Figure 23b). Finally, the diffraction efficiency for a beam propagating through both AODs have been measured as a function of frequency difference between the two AODs, tuning the first AOD from from 60 MHz to 86 MHz in steps of 500 kHz while the second one is tuned from 86 MHz to 60 MHz with the same step size. The result can be seen in Figure 24.

When driving the AODs with multiple tones simultaneously, the total power in dBm adds according to

$$P_{dBm} = 10 \cdot \log_{10} \left(\sum_{i=0}^{n} \frac{P_i[W]}{1 \cdot 10^{-3}[W]} \right), \tag{104}$$

where P_i are the powers of the individual signals in Watts and n corresponds to the number of RF tones. This allows for relatively high voltages in each RF tone driving the AODs without damaging them, as a second tone of equal power only adds 3 dB to the total power.

The RF tone amplitude used to determine the diffraction efficiency of the combined AOD system, which will be needed in order to create independently tunable traps (see Chapter 4.1.2) is chosen as 100 mV, which is slightly above the voltage theoretically creating the highest diffraction efficiency if two tones are fed to each AOD (130 mV for one tone correspond to 90 mV per tone for two tones). However, this value led to the highest diffraction efficiency in the experiment.

From Figure 23 we observe that in the interval $f = (73 \pm 10)$ MHz the AOD diffraction efficiency η has a roughly flat response (maximal difference in diffraction efficiency $\Delta\eta < 4\%$) to a change in the driving frequency for both AODs. The overall variation of two AODs and for 100 mV RF voltage is only $\Delta\eta < 8\%$ (see Figure 24).

It is important to know the frequency range over which the AODs can be used without significantly dropping in power, since this determines the position range over which the particles can be moved without losing them due to insufficient strength of the trapping potential. It is not only given by the diffraction efficiency of the AODs, because the driving frequency of the AODs also spatially shifts the laserbeam (see Chapter 4.1.2) which can in turn lead to a power change inside the traps due to an imperfect alignment or due to the limited aperture of optical components along the beam path.

To determine the effect of the AOD driving frequencies on the trap depth, we trapped two particles and measured their frequencies while also scanning the RF tone frequencies. The particle frequencies relate to the trapping power according to eq. 22. The characterization measurement is done with two particles in order to have the same conditions as during an experiment. They are moved simultaneously, while the optical interaction is minimized by choosing the polarization of the traps to be aligned with the particle connection axis, such that frequency changing effects that might occur due to e.g trap interference or standing waves inside the tweezer are already accounted for. The two AOD tone frequencies are shifted symmetrically from the center position of 73 MHz. In order to ensure that the particles are not lost, the measurement starts at the frequencies $\omega_A = 72$ MHz and $\omega_B = 74$ MHz, moving the particles apart from each other until $\omega_A = 69$ MHz and $\omega_B = 77$ MHz in steps of 150 kHz, with $\omega_C = \omega_A$ and $\omega_D = \omega_B$ (see Chapter 4.1.2). Figure 25 shows the resulting particle frequencies. The x-axis corresponds to the frequency used in the horizontal

AOD for the respective trap. We observe, that if the traps are very close together ($\Delta\omega_{AOD} \leq 4$ MHz), the particle frequencies start to decrease rapidly since interference effects between the traps start to arise as the particle distance comes close to the trap size ($w_0 \approx 1$ μm). However, for separations $\Delta\omega_{AOD} \geq 4$ MHz, the particles frequencies stayed approximately constant, with a deviation $\Delta\Omega_p < 10\%$. We thus know that positioning the particles at a distance that corresponds to an AOD drive interval between $\Delta\omega_{AOD} = (4\text{ MHz}, 8\text{ MHz})$ will create stable traps of similar power.

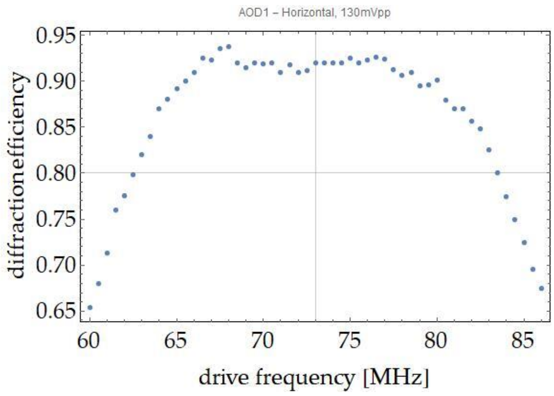

(a) First order diffraction efficiency of the horizontally aligned AOD as a function of the AOD driving frequency.

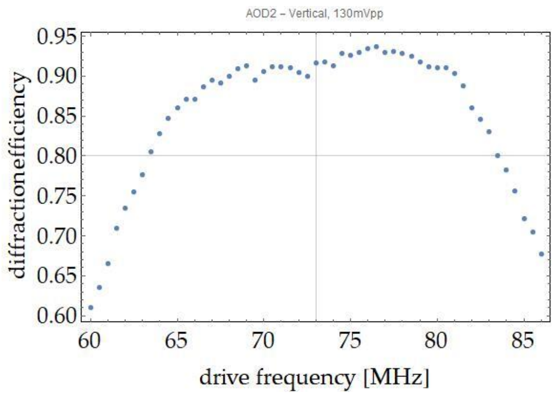

(b) First order diffraction efficiency of the vertically aligned AOD as a function of the AOD driving frequency.

Figure 23: First order diffraction efficiency for both AODs measured separately at maximal RF powers as a function of driving frequency.

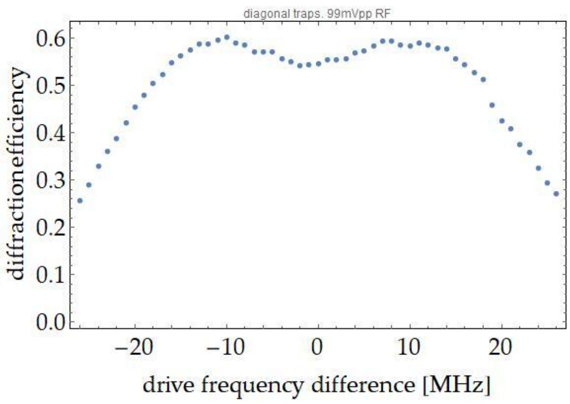

Figure 24: First order diffraction efficiency for the combined (horizontally + vertically oriented) AOD system. Note that the overall diffraction efficiency is lower than the product of the measurement efficiencies for the individual AODs (see Figure 23) because the RF power was reduced in order to obtain the maximally possible diffraction efficiency when running the AODs with two tones each (as explained in the text).

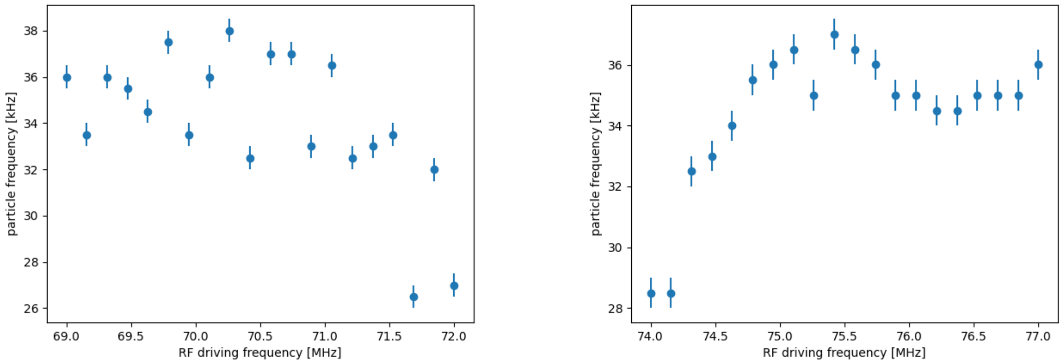

(a) Particle frequency in trap 1 as a function of AOD-H drive frequency.

(b) Particle frequency in trap 2 as a function of AOD-H drive frequency.

Figure 25: Particle frequency as a function of AOD drive frequency while two particles are trapped. The particle frequencies where obtained by taking the maximum of the PSD of the particle signals. The errorbars correspond to the resolution bandwith (RBW = 500 Hz) that was used to calculate the PSDs. The left Figure corresponds to trap 1 and the right Figure to trap 2. The x-axis labels the frequency in the horizontal AOD used to create the respective trap. The frequency of the vertical AOD is shifted symmetrically around the center frequency $\omega_{AOD,c} = 73$ MHz. The sharp drop off in particle frequency close to $\omega_{AOD,c}$ can be attributed to interference between the traps, since the distance between the particles becomes similar to the trap size.

4.2.2 Distance calibration

In Chapter 4.1.2, the mechanism used for tuning the distance between the traps is explained heuristically. However, relying only on the means of ray tracing to obtain the distance between the two traps as a function of the RF frequencies ω_A and ω_B that displace the input beam will most likely not give us a correct answer. This is due to the fact that precise alignment of all optical components is merely impossible as each lens that isn't aligned into a perfect telescope introduces an error. Therefore, a different method for determining the distance between the traps is needed.

We chose to calibrate the position of the traps as a function of the RF driving frequency by the interference of the light scattered from the two particles. We positioned a camera at a vacuum chamber window allowing us to monitor the trap in a 90° angle with respect to the optical axis, as can be seen in Figure 14. From this point of view, one cannot distinguish between having trapped one or two particles, since they are exactly behind each other. However, when the tweezer light is not polarized in direction of the camera (x-direction), tuning the distance between the particles now changes the intensity of the light hitting the camera sensor. This is a result of the coherent dipole radiation of the two particles interfering with each other, as is sketched in Figure 26, and can thus be used to calibrate the distance between the particles. The intensity of the combined field is of the form

$$
\begin{aligned}
I(x) \propto& |E_1 + E_2|^2 = |E_{0,1}e^{i(kx_1+\phi_1)} + E_{0,2}e^{i(kx_2+\phi_2)}|^2 \\
=& I_1 + I_2 + 2\sqrt{I_1 I_2}\cos(kR + \phi),
\end{aligned}
\tag{105}
$$

where I_1, I_2 correspond to the individual intensities of the particles dipole radiations in x-direction, $R = x_2 - x_1$ is the distance between the two particles, $\phi = \phi_2 - \phi_1$ is the optical phase difference between the two traps.

By recording the intensity on the camera while changing the frequencies of the AOD drivers in small enough steps, we obtain a sinusoidal interference pattern, as can be seen in Figure 27. We extract the frequency difference between two maxima of this pattern by fitting it with eq. 105 and setting

$$kR = 2\beta\Delta f, \tag{106}$$

where Δf corresponds to the frequency difference of one of the two AOD drives in MHz, β is a calibration factor relating the change in RF drive frequency to a change in intensity. The factor of 2 has been included since the frequency change in one tone only corresponds to half of the total frequency change as we change the frequencies in both of them simultaneously. This is done, because we wanted to simulate distance changes we perform when taking measurements, where we always move symmetrically around the center frequency of the AODs (73 MHZ) in order to ensure maximum and symmetric diffraction efficiencies in both traps. Figure 27 shows the normalized total brightness of the camera images as a function of frequency difference of the two tones driving each AOD. The frequency in RF tone one was moved between 69 MHz and 71.5 MHz in steps of 10 kHz, the frequency of RF tone 2 between 77 MHz and 74.5 MHz. The resulting calibration factor β of the fit takes the value

$$\beta = (1.75 \pm 0.01)\,\mathrm{MHz}^{-1}, \tag{107}$$

$$\longrightarrow R = \frac{\beta \cdot \lambda}{\pi} = (592 \pm 3) \cdot 10^{-9} \frac{\mathrm{m}}{\mathrm{MHz}}. \tag{108}$$

As can be observed from Figure 27, the data points don't give a perfect sinusoidal pattern due to aberrations that become stronger the closer one moves to the center. We attribute this to Airy rings around the traps created by cutting the beam on the aperture of the trapping lens. The Airy rings then interfere with the other trap and thus slightly modify the trapping potential. Additionally, for very close distances, the coupling between the particles becomes very strong and significantly shifts their equilibrium position.

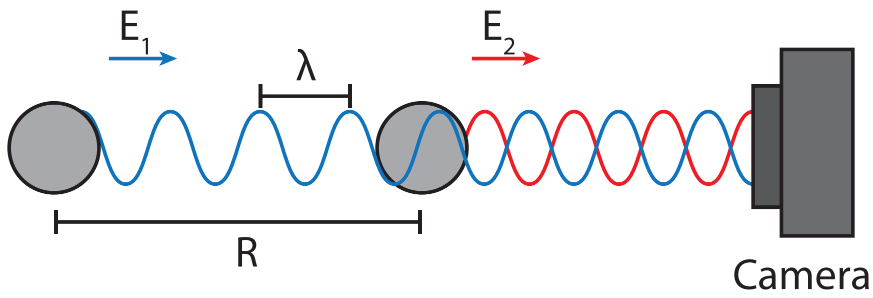

Figure 26: Sketch of the fields radiated by the two particles in direction of the camera. Both particles coherently radiate light of the same frequency and phase as their optical trap, causing the fields to interfere. The brightness of the light detected by the camera is therefore dependent on the phase of their radiated light. It can be used to calibrate the distance between the particles as a function of the frequencies driving the AODs.

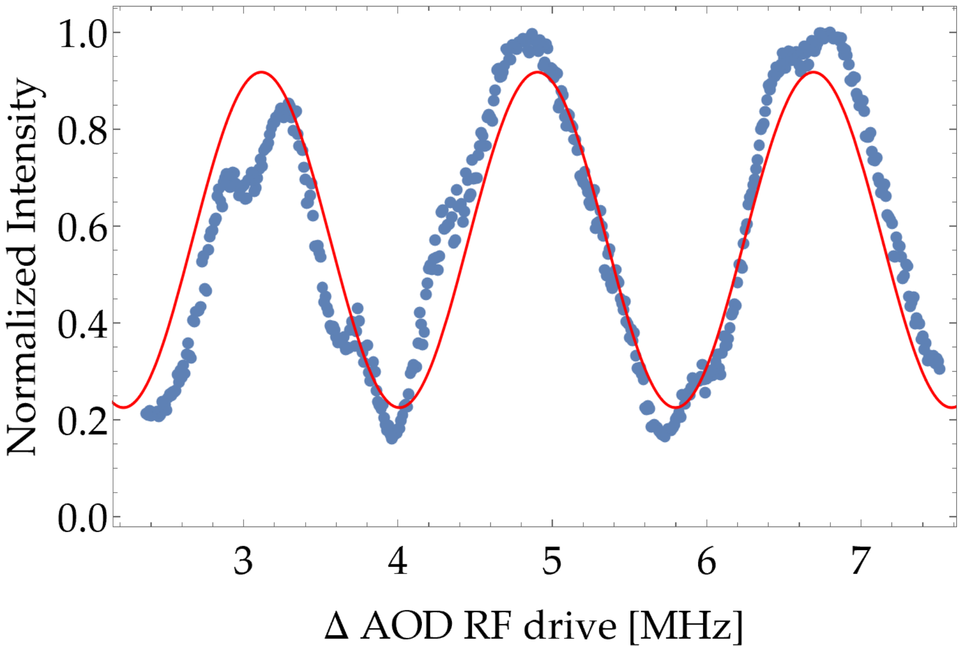

Figure 27: (Blue) Normalized intensity of the radiation captured with a camera as a function of AOD drive frequency difference. (Red) Fit of the interference pattern.

4.2.3 Detection characterization

The general detection scheme is implemented as described in Chapter 4.1.3. Two things have to be considered to assure an optimal detection of the particles signal:

- Phase locking between the particle signal and the local oscillator
- Minimal crosstalk of the two particle signals in their individual detections

Phaselocking between the local oscillator and the signal beam is necessary in order to obtain the maximum signal amplitude in the first harmonic of the particles motion (see Chapter 4.1.3). Without the use of a PID (proportional integral derivative) controller, the phase difference between our signal and local oscillator $\phi = \phi_{signal} - \phi_{LO}$ is not constant. Figure 15 shows the electronic path build to ensure a phase locked balanced homodyne detection. By applying a voltage to the piezo in our local oscillator path, it changes its length which in turn changes the optical path length l of the LO which relates to its phase by

$$\Delta\phi_{LO} = \frac{2\pi\Delta l}{\lambda}. \tag{109}$$

By locking to a certain phase θ, the PID drives the piezo with a correction voltage such that by changing the path length of the local oscillator, the overall phase $\phi_{tot}\phi_{sig} + \phi_{LO} = \theta$. We characterize the quality of the lock by monitoring the error signal.

Figure 29a shows the error signal (above) and the PSD of the detected signals (below) from homodyne 1 (left) and homodyne 2 (right) when a particle is trapped in trap 1 while performing a phase sweep of the trap phase in 5° steps. Homodyne 1 corresponds to the homodyne detection set up for a particle in trap 1 and equivalently homodyne 2 corresponds to the detection of trap 2. Figure 29b shows the respective plots for a particle trapped in trap 2. The trap difference here is 6 MHz which corresponds to a distance $R \approx 12.5\mu$m. Since this data was taken in a previous alignment of the setup, it doesn't correspond to the distance per MHz obtained in Chapter 4.2.2.

For each phase step a 1s time chunk was evaluated. This shows us if the phases can stay locked for time periods that are sufficiently long to take measurement as well as for abrupt changes in the initial conditions for the lock. The sampling interval SI $= 5.6 \cdot 10^{-8}$ s and the spectrum was averaged until a resolution bandwith of RBW $= 1$ kHz was reached.

From the error signal in Figure 29a we see, that homodyne 1 stayed locked during the whole measurement. The spectrum shows a strong peak at $\omega = \omega_0 \approx 29$ kHz as well as a weaker peak at $\omega = 3 \cdot \omega_0 \approx 87$ kHz. These peaks correspond to the frequency of the particles motion and its third harmonic in z-direction, respectively. The second harmonic $\omega = 2 \cdot \omega_0 \approx 58$ kHz is barely visible, which implies that the correct phase for locking has been chosen. The right side of Figure 29a shows the error signal and PSD for the detection of trap 2. Since there was no particle present in trap 2, the only signal detected is light radiated from the particle in trap 1 into detector 2 due to imperfect separation of the two signals in the detection path. Since the signal is very low, the PID wasn't able to phase lock the local oscillator to the particles signal during the whole measurement period. This is made visible by the non-constant error signal and results in a change in amplitude of the particles harmonics.

Figure 28 shows the same measurement for a particle trapped in trap 2. This data has been taken using imperfect locking parameters, resulting in an occasional loss of phase lock between the local oscillator and the signal beam in the detection of trap 2. From this measurement we can see that as soon as the overall phase falls out of lock, the amplitude of the first and third harmonic declines, while the second harmonic becomes visible. Knowing that the change in amplitude of the first harmonic and the change in error signal strongly correlates made us decide to neglect time trace parts where the error signals average deviates from zero when taking data in order to ensure that any amplitude changes detected during the measurement are only due to coupling effects.

Figure 29 shows detection 1 and 2 for a particle trapped in trap 2 after optimizing the locking parameters. The detection of trap 2 now stayed locked during the whole 72 s measurement duration.

Additionally, from Figure 29 we can make some statements about the crosstalk between the two detection arms. The PSDs taken from both trap detections are set to the same scale. The distance roughly corresponds to the distance in which the measurements in Chapter 5 were done. We can see, that there is a small signal present in the detection of the trap in which no particle is present. However, the difference between the peak and the maximal crosstalk is

$$I_s - I_{ct} \approx 30dB. \tag{110}$$

This means, that the detection of the particle interaction is limited by this background.

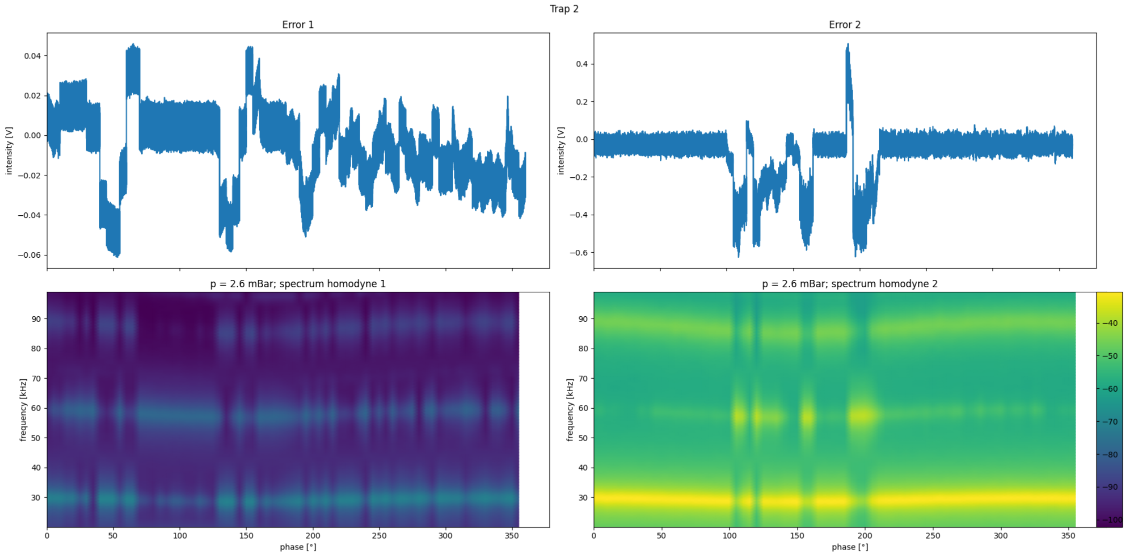

Figure 28: Particle trapped in trap 2. Top: Error signal of the PID lock for trap 1 detection (left) and trap 2 detection (right). Bottom: PSD of the particles signal detected in trap 1 detection (left) and trap 2 detection (right) while performing a phase scan of the tweezer field in steps of 5°, one second per step with **unstable lock**. Whenever the error signal deviates from its mean value the amplitudes of the first and third harmonics of the particles motion decrease while the amplitude of the second harmonic increases.

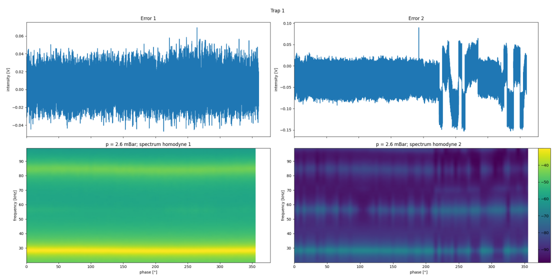

(a) Particle trapped in trap 1. Top: Error signal of the PID lock for trap 1 detection (left) and trap 2 detection (right). Bottom: PSD of the particles signal detected in trap 1 detection (left) and trap 2 detection (right).

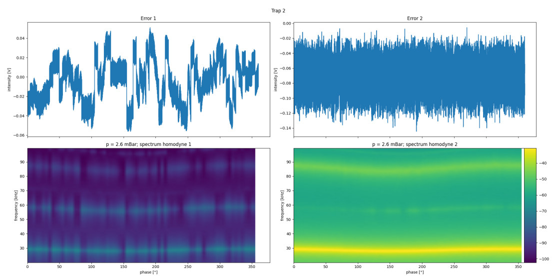

(b) Particle trapped in trap 2. Top: Error signal of the PID lock for trap 1 detection (left) and trap 2 detection (right). Bottom: PSD of the particles signal detected in trap 1 detection (left) and trap 2 detection (right).

Figure 29: Error signal and PSD of the two detections for a particle trapped in trap 1 (left) and trap 2 (right) while performing a phase scan of the tweezer field in steps of 5°, one second per step with **stable lock**. The error signal is now constant on the side on which a particle is trapped, leading to a constant amplitude in all of the harmonics of the particles motion.

4.3 Intensity noise reduction

The motional frequencies of optically trapped particles depend on the power in the optical traps (see Chapter 2.2.3). Therefore, in order to have a stable system in which a change in frequencies can be traced back to a change in the system dynamics one has to assure that the overall optical power used for trap creation stays constant. This is not a given, since the precise output power of our laserhead is temperature dependent. Furthermore, the focus point of the beam put out by the laserhead is also temperature dependent, causing the coupling efficiency to the fiber connecting the beam preparation stage and the trap generation stage to change.

To overcome this issue, an isolating box was build to shield the beam preparation stage from external temperature fluctuations. To monitor the effect of this box, we placed a thermometer on top of the laserhead to measure the correlations between the power fluctuations after the fiber and temperature change with and without box over many hours. From Figure 30 we observe, that the temperature in the lab fluctuates over the range of at least 1°C and that the power fluctuations after the fiber strongly correlate with these fluctuation. In fact, the relative power fluctuation after the fiber is $(P_{max} - P_{min})/P_{avg} = \Delta P/P_{avg} \approx \%40$.
Figure 31 shows the same measurement after implementing the box. The time span over which the measurement was taken is shorter since the storage on the SD card of the powermeter was full after a couple of hours. However, one can already see a great improvement of the temperature stability, with fluctuations in a range of ≈ 0.2°C. Also, the temperature and the power after the fiber are no longer correlated. The relative power fluctuation after the fiber in this measurement is $(P_{max} - P_{min})/P_{avg} = \Delta P/P_{avg} \approx 6\%$.
To remove the remaining intensity fluctuations, an intensity locking scheme using an AOM and a PID box was implemented. The basic idea behind this locking scheme is to modulate the RF power driving the AOM that then modulates the power in the first diffraction order such that the power in the zeroth order is kept constant (see e.g. [46]).
The AOM is placed at the beginning of the beam preparation stage, just after the Faraday isolator (see Figure 14). After the beam enters the trap generation stage, a fraction of it is split off and sent to a photodetector. The output signal of the photodetector is then sent to the PID box. The output signal of the PID box is put through a 1 kHz lowpass filter and sent to an RF driver (FlexDDS), that drives the AOM at its center frequency (110 MHz). The RF driver is programmed such that the power with which the AOM is driven depends on the output of the PID box but has a minimal diffraction efficiency of 10%, since AOMs have a very flat response with respect to the input power at low input powers, and a maximal diffraction efficiency of 20%. The upper limit is set such that there will never be too much power dumped inside the beam preparation stage that heats up the box. The laser amplifier is set to output 10 W, corresponding to 1 W for minimal and 2 W for maximal modulation in the first diffraction order.
Figure 32 shows a measurement of the voltage on a photodetector in the trap generation path, proportional to laser intensity in front of the trap, as well as the particles frequency along the optical axis without intensity lock, taken over 60s. We observe, that apart from the fast oscillations there is also a slow downwards drift in intensity that is mimicked by the particles frequency. Figure 33 shows the same measurement with the intensity lock turned on. The fast oscillations are still present, though from the average (orange line) we see, that they've become less pronounced. However, the slow drift, is surpressed, meaning that the average trap frequencies will be constant with time, as can be seen from the lower three plots of 33. Unfortunately, the phase between signal and local oscillator has not been locked during this measurement, which leads to variation in the

detection sensitivity. This affects the ability of the script to correctly detect the central frequency, which causes these sharp occasional drop offs in frequency. Therefore, the histogram also doesn't seem Gaussian anymore as it is not symmetric around its maximum, but has its mean value shifted towards the low frequency regime. In Figure 32 the standard deviation is $\sigma = 0.16$ kHz. In Figure 33, when neglecting the incidences with the three lowest frequencies, the distribution becomes more Gaussian looking and has a standard deviation of $\sigma = 0.12$ kHz.

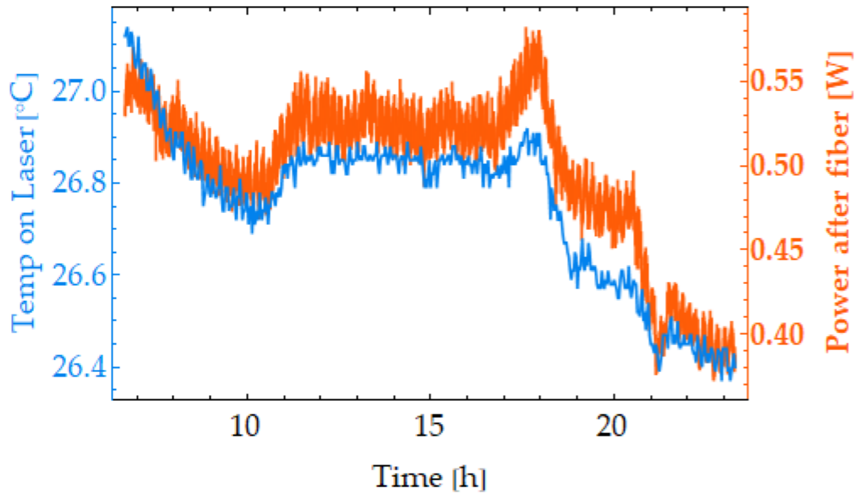

Figure 30: Temperature measured on top of the laserhead (blue) and power detected after the fiber connecting the beam preparation stage and the trap creation stage (orange) as a function of time **without isolation box**.

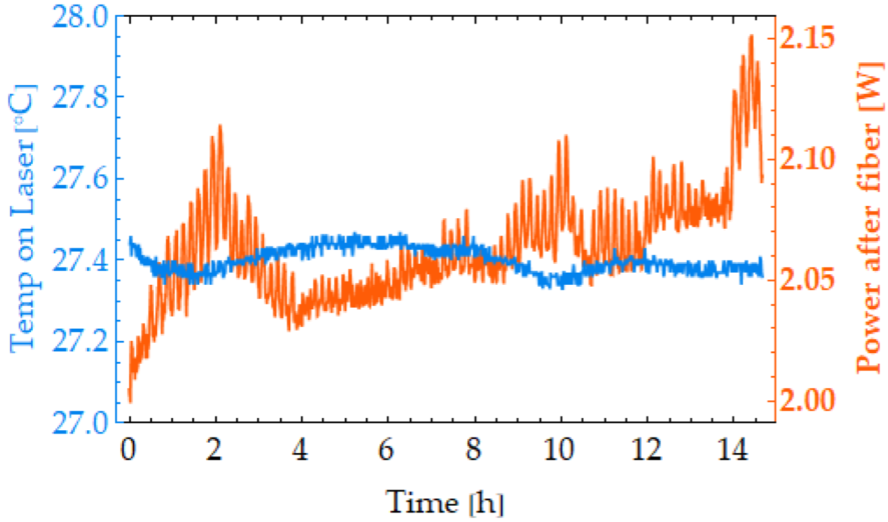

Figure 31: Temperature measured on top of the laserhead (blue) and power detected after the fiber connecting the beam preparation stage and the trap creation stage (orange) as a function of time **with isolation box**.

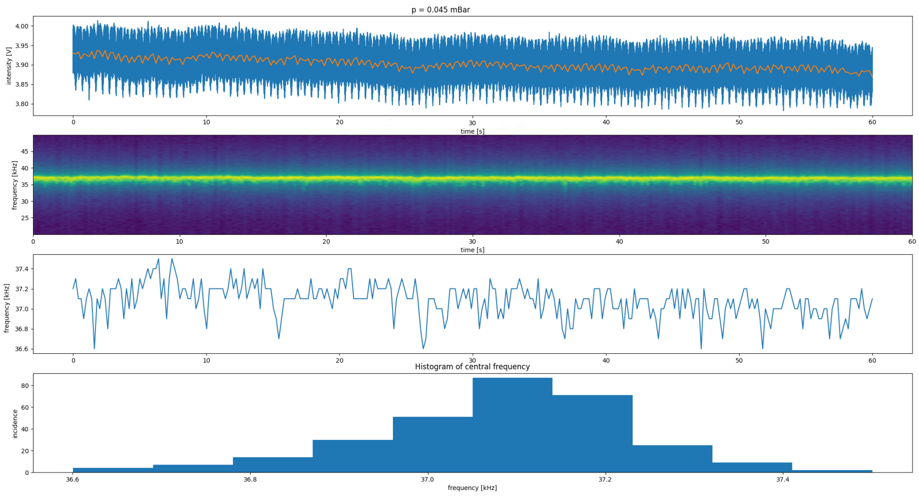

Figure 32: Data taken with intensity **not locked**. From Top to Bottom: (1) Voltage corresponding to laser intensity (blue), with averaged intensity (orange) as a function of time. (2) PSD of the z-motion of a trapped particle as a function of time. (3) Maximal frequency in z-direction as a function of time. (4) Histogram of (3).

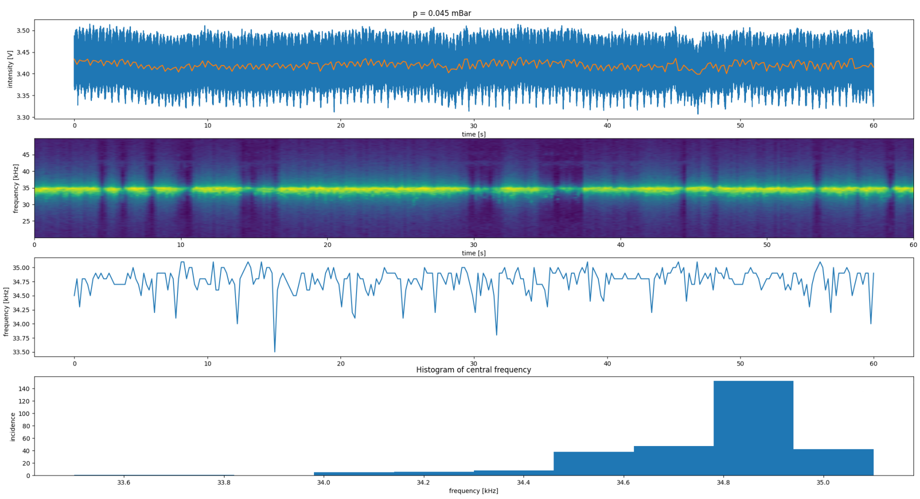

Figure 33: Data taken with intensity **locked**. From Top to Bottom: (1) Voltage corresponding to laser intensity (blue), with averaged intensity (orange) as a function of time. (2) PSD of the z-motion of a trapped particle as a function of time. (3) Maximal frequency in z-direction as a function of time. (4) Histogram of (3).

5 Observation of the optical interaction between two nanoparticles

In this Chapter we will present the experimental results that verify some of the theoretical considerations made in Chapter 3.3. We trap particles of radius r = 105 nm levitated in a tightly focused Gaussian beam of wavelength $\lambda = 1064$ nm at pressures p $\approx$ 2 mbar. In order to observe the avoided crossing present when we test the conservative system dynamics, it is important that the pressure is sufficiently low such that our coupling rate $g > \gamma/2$. For very small pressures however, the non conservative coupling starts driving the particles far into the nonlinear regime due to the lack of gas damping and we risk losing our particles if they are not cooled in order to reduce their motion. That is why we have settled for the above mentioned pressure.

We first probe the system dynamics in absence of optical interactions in order to check that there are no charges present on our particles that cause our particles to strongly couple via electrostatic forces (see Chapter 3.2) which could be mistaken for optical interaction. Then, we probe the conservative forces between two optically coupled nanoparticles. Finally, we try to minimize the conservative interaction in order to probe the system dynamics in the presence of non-conservative and maximally non-reciprocal interaction. Note that all of the results have been taken in a previous alignment of the setup and thus the distance between the particles as a function of RF drive frequency does not correspond to the results obtained in Chapter 4.2.2.

5.1 Non-interacting particles

Since the orientation of the dipole radiation depends on the trapping light polarization, one can fully suppress any optical interaction between the two particles by choosing the polarization to coincide with the particles joint axis. In this case the particles don't radiate any light towards each other (see eq. 85). Figure 34c shows the PSD of the detected particle signals both individually and combined for horizontal polarization and hence full suppression of the optical interaction at a pressure of $p = 2$ mbar. An amplitude scan of the RF tones driving the AODs was performed at a particle distance R $\approx 13\,\mu$m, subsequently increasing the amplitude of one RF tone in the first AOD, while decreasing the amplitude of the second tone. The RF tones of the second AOD are left unchanged. This way, the amplitude of trap 1 increases while it decreases for trap 2. Each measurement changed the voltage of the RF tone by $\approx$ 1% (which can be assumed to roughly correspond to a linear change in power as well, since the total voltage change $\Delta V \ll V$, meaning that the change in RF power $\Delta P \propto \Delta V^2$ can be assumed as $\Delta P/P \propto \Delta V/V$). The response of the optical power to a change in RF power inside the AODs will further also assumed to be linear, which again is a fair assumption for small changes with respect to the total power.

Figure 34 shows the resulting change in mechanical frequencies, behaving like predicted from the dynamics of a single, optically trapped particle (see eq. 22). From Figure 34a and 34b we see that we are able to have fully separate detections of our two particles motion. For the fitting of Figure 34c, first the z-frequency peak of each individual spectrum was fitted using eq. 43 which correspond to the blue and orange points for particle 1 and particle two, respectively. Eq. 95 with $k_1 = k_2 = 0$ was used to fit the frequency changes as a function of measurement number, where each measurement was taken a different trap amplitude ratio. The resulting fit functions corresponds to the dashed lines in Figure 34c. The frequency at the crossing Ω and the relative trap amplitude at the point of crossing η_m obtained through the fit are

$$\Omega = 27.94 \pm 0.02, \qquad \eta_m = 0.01 \pm 0.01, \tag{111}$$

where the error of Ω comes from the fit and the error of η corresponds to the measurement step size.

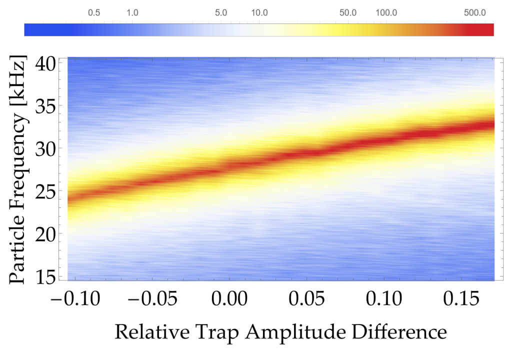

(a) PSD of particle 1 as a function of trap depth.

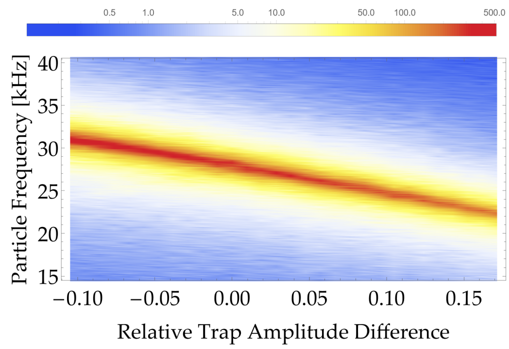

(b) PSD of particle 2 as a function of trap depth.

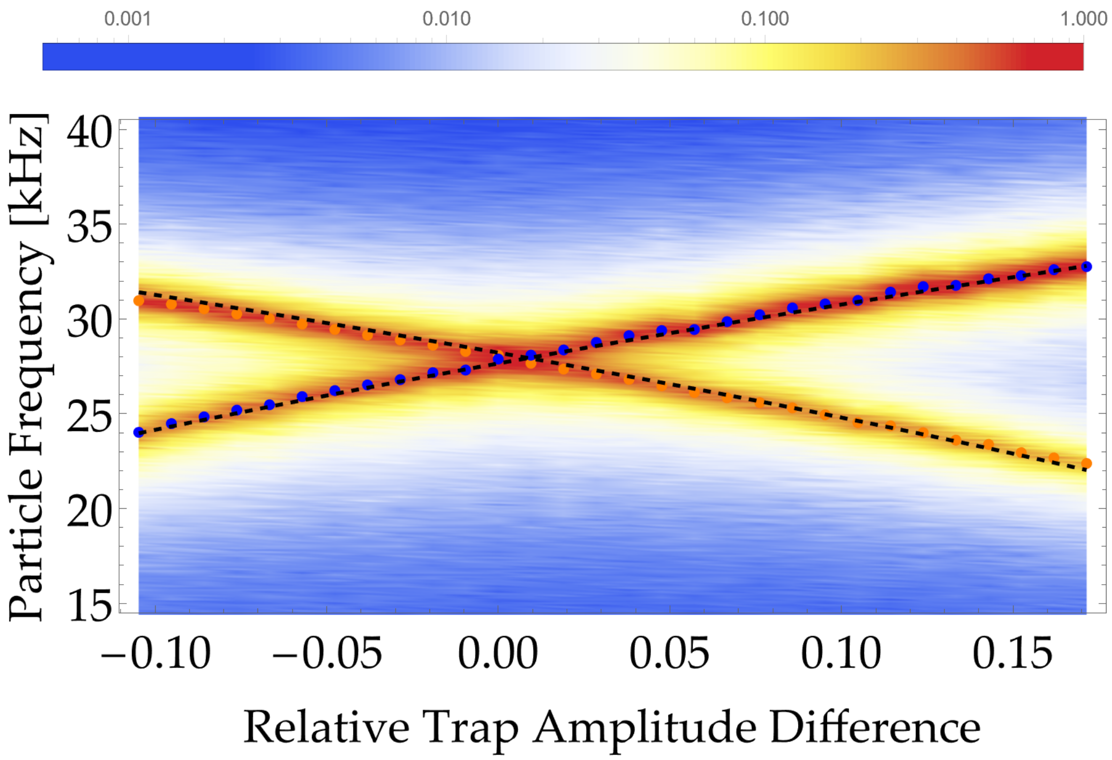

(c) PSD of combined detection as well as fit as a function of trap depth (dashed line). The blue (Orange) points correspond to the motional z-frequency of particle 1 (2) obtained by fitting the individual spectra.

Figure 34: PSD (in arbitrary units) of the particles motion as a function of trap amplitude **without optical interaction** at distance $\mathrm{R} \approx 13\ \mu\mathrm{m}$ and pressure $\mathrm{p} = 2$ mbar. Figures (a,b) show the PSDs of the individual particle detections which show no visible crosstalk, demonstrating our capability to individually detect each particle. Figure (c) shows the superimposed spectra of Figures (a,b). For each measurement, the trap amplitude was increased for the trap of particle 1 while it was decreased for the trap of particle 2 by the same, constant amount. This also caused a linear change of peak height with amplitude due to the linear change in signal strength.

5.2 Conservative interaction

As a next step, we changed the trap polarization maximize the optical interaction. In order to see strong, conservative coupling we tried to position the particles at a multiple of the wavelength λ, as this maximizes the conservative coupling rate $k_1 \propto \cos(kR_0)\cos(\phi_0)/R_0$ while it suppresses the non-conservative coupling rate $k_2 \propto \sin(kR_0)\sin(\phi_0)/R_0$ as can be seen from eq. 85. The particles were positioned at a distance R $\approx$ 13 μm (same configuration as in Chapter 5.1). We tuned the phase difference in the optical traps by changing the phase of one of the RF tones driving the AODs (see Chapter 4.1.2) to find the position of maximal splitting. This is important, since zero phase difference in the RF tones driving the AODs doesn't necessarily correspond to zero phase difference in the trapping fields since the path length of the two traps will never be completely equal due to alignment imprecisions. After finding the optimal phase values for the RF tones, the amplitude of the traps was scanned again by modulating the amplitude of the RF tones driving the AODS in analogy to Chapter 5.1.

The blue and orange points in Figure 35c show the z-frequencies of particle 1 and 2, respectively. They are obtained by fitting the PSDs of the individual measurements with eq. 43. For the fit in Figure 35c (black dashed lines), eq. 95 was used as a fitting function with $k_2 = 0$. In this fit, a linear change in trap power with RF power was assumed again, which is a fair assumption for small changes. The center of mass frequency Ω and coupling constant g extracted from the fitting function take the values

$$\Omega = (28.14 \pm 0.06)\ \text{kHz}, \tag{112}$$

$$g = (0.94 \pm 0.05)\ \text{kHz}, \tag{113}$$

$$\frac{g}{\Omega} = 0.033 \pm 0.002. \tag{114}$$

The errors here correspond to the fitting errors. Figure 35 show the measured spectrum of particle 1 (35a), particle 2 (35b) and the combined spectra together with the fit obtained as described above (35c). Comparing with 5.1, we can see how the eigenfrequencies of the individual particles now split into the two normal modes when the frequencies of the two particles come close together, creating the characteristic avoided crossing due to their optical interaction.

In case of minimal splitting ($\eta = \eta_m$), the normal modes correspond to the center of mass mode, moving with the sum of the two particles motions ($z_1 + z_2$) and the breathing mode, moving with their difference ($z_1 - z_2$) (see Chapter 3.1). By taking the sum and difference of the time traces obtained for the measurement taken at $\eta \approx 0$, one can thus reconstruct the normal modes of the system, as can be seen in Figure 36. The breathing mode Ω_{BM} is lower in frequency and thus energy, than the center of mass mode Ω_{CM}, which means that this measurement was done at a point of negative coupling.

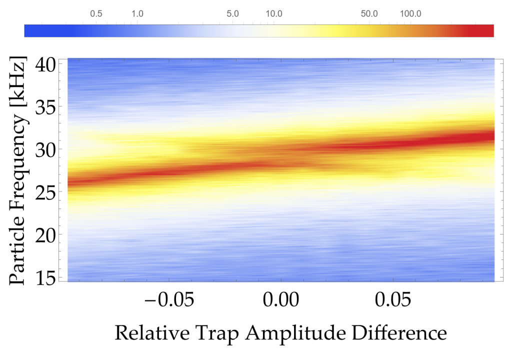

(a) PSD of particle 1 as a function of trap depth.

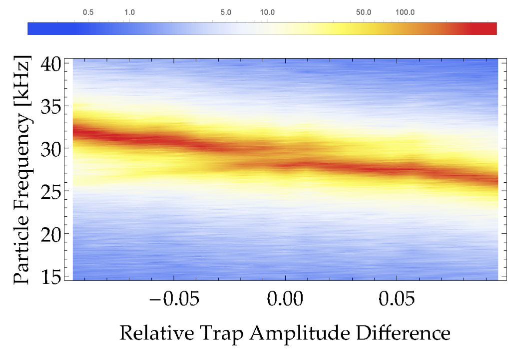

(b) PSD of particle 2 as a function of trap depth.

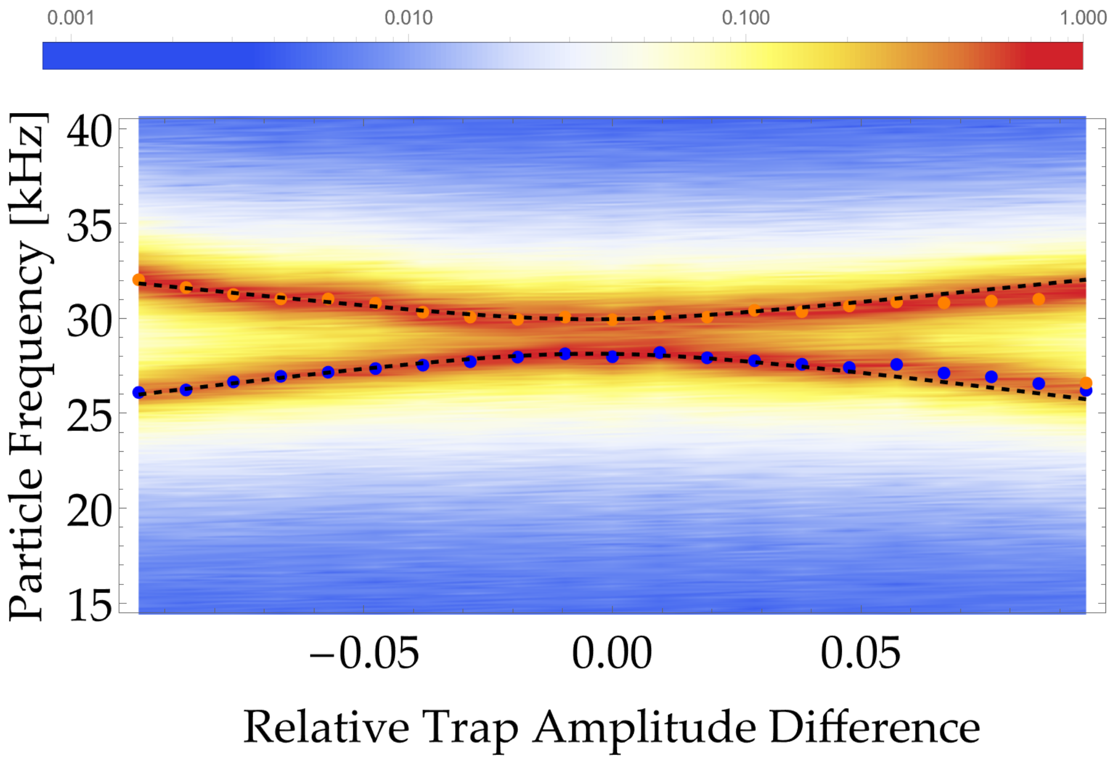

(c) PSD of combined detection as well as fit as a function of trap depth (dashed line). The blue (Orange) points correspond to the motional z-frequency of particle 1 (2) obtained by fitting the individual spectra.

Figure 35: PSD (in arbitrary units) of the particles motion as a function of trap amplitude **with optical interaction** at distance R $\approx$ 13 μm and pressure p = 2.2 mbar. Figures (a,b) show the PSDs of the individual particle detections. At the point of minimal splitting ($\eta_m = 0$) there is exactly equal mixing of the two normal modes in each particle motion. Figure (c) shows the superimposed spectra of Figures (a,b) showing an avoided crossing due to the optical interaction. For each measurement, the trap amplitude was increased for the trap of particle 1 while it was decreased for the trap of particle 2 by the same, constant amount.

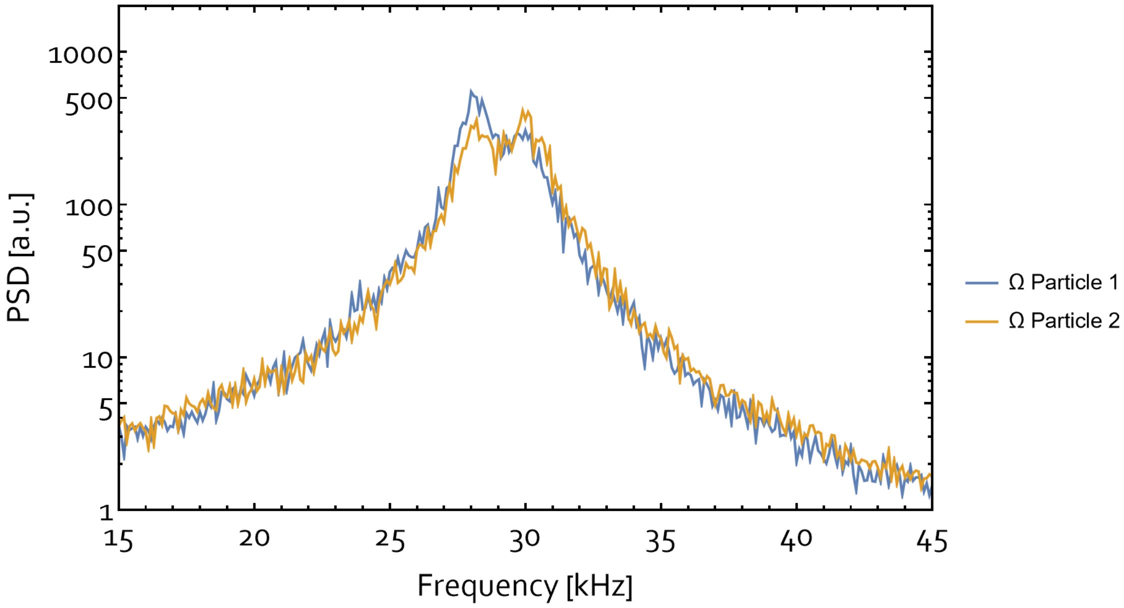

(a) PSD of the two particle motions.

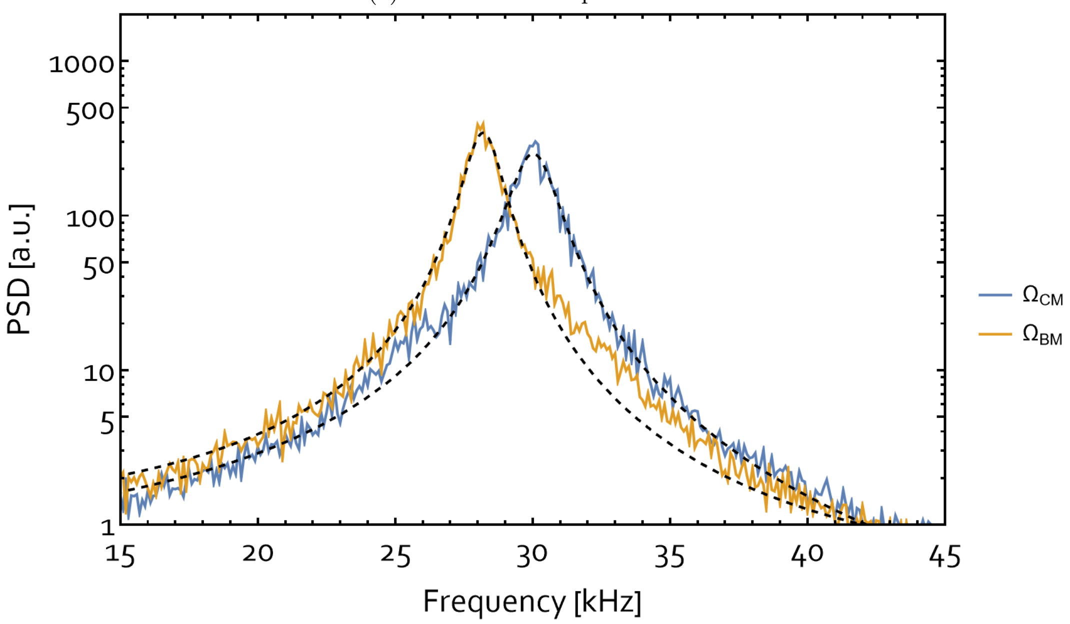

(b) PSD of the normal modes.

Figure 36: PSD (in arbitrary units) obtained from the time traces of the two particles at minimal splitting ($\eta_m = 0$). (Top) PSD of the individual traces, corresponding to the individual particle motions. (Bottom) PSD of the added and subtracted traces, corresponding to the center of mass and breathing mode, respectively. The dashed lines are fits of the PSD using eq. 43.

5.3 Non-conservative interaction

Next, we tried to probe the non-conservative interaction between the particles given by $k_2 \propto \sin(kR_0)\sin(\phi_0)/R_0$. Moving the particles away from the position were we have found maximal conservative interaction by $\lambda/4$ minimizes the conservative interaction $k_1 \propto \cos(kR_0)\cos(\phi_0)/R_0$ while maximizing $\sin(kR_0)$ of the non-conservative interaction. Afterwards, we again tuned the phase of one of the traps in order to find the position of maximal non-conservative coupling. Figure 37 shows an amplitude scan at this position, performed in the same manner as in Chapter 5.2 and 5.1. Figures 37a and 37b prove that $k_2 > k_1$, since there is no avoided crossing present and the eigenfrequencies are degenerate for a range of values of η (see Chapter 3.3.2). Due to the non-conservative nature of the interaction, the amplitude of particle 1 is increased in that period, while the amplitude of particle 2 is mostly decreased.

Figure 38 shows a spectrum of particle 1 (left) and particle 2 (right) in which the eigenfrequencies are degenerate. It corresponds to the slice of Figure 37 where the relative trap amplitude difference takes the value $\eta = -0.048$. In Figure 38a one can clearly see, that on top of the "usual" Lorentzian peak there is a second Lorentzian with increased amplitude and decreased linewidth due to the optical driving of the motion of particle 1 with the coherently scattered light of particle 2. The green and red line correspond to fits of the spectrum of particle 1, where the data points around the peak have been removed for the green fit and all the other data points have been removed for the red fit. The linewidth and peak amplitude obtained from the green fit $\gamma_{1,g}, S_{xx,g}(\Omega_1)$, and the red fit $\gamma_{1,r}, S_{xx,}(\Omega_1)$ are

$$\gamma_{1,g} = (3.06 \pm 0.08)\ \text{kHz}, \qquad S_{xx,g}(\Omega_1) \approx 115\,\frac{\text{V}^2}{\text{kHz}},$$

$$\gamma_{1,r} = (0.35 \pm 0.08)\ \text{kHz}, \qquad S_{xx,r}(\Omega_1) \approx 950\,\frac{\text{V}^2}{\text{kHz}}.$$

The peak amplitudes have been obtained by taking the value of the function fit were Ω corresponds to the peak frequency Ω_1 obtained through the fit. The numerical value of $S_{xx}(\Omega)$ is dependent on the voltage measured on the oscilloscope and hence doesn't correspond to the optical power per Hertz but is only proportional to it. Furthermore, a different voltage measured in the two detection paths doesn't necessarily imply a different PSD but can also be due to alignment differences. Therefore, we will in the following only compare the amplitude ratios detected in the same detection arm.

The linewidth of the amplified peak is reduced by $\gamma_r/\gamma_g \approx 0.11 \approx 1/9$. Furthermore, the amplitude ratio at the peaks is increased by $S_{xx,r}(\Omega_1)/S_{xx,g}(\Omega_1) \approx 8.3$. The linewidth and peak amplitude $\gamma_{2,r}, S_{xx,r}(\Omega_2)$ of the peak obtained through the fit in Figure 37b are equal to

$$\gamma_{2,r} = (3.6 \pm 0.2)\ \text{kHz}, \qquad S_{xx,r}(\Omega_2) \approx 18\,\frac{\text{V}^2}{\text{kHz}}.$$

To better understand how the linewidth and amplitude of the spectrum of the two particles change with respect to the uncoupled case, a fit of the spectra in the first slice of Figure 37a ($\gamma_{1,0}$) and

37b ($\gamma_{2,0}$) is used for comparison. Here, the fitted parameters are

$$\gamma_{1,0} = (2.20 \pm 0.04)\ \text{kHz}, \qquad S_{xx,0}(\Omega_1) \approx 207\,\frac{\text{V}^2}{\text{kHz}},$$

$$\gamma_{2,0} = (2.21 \pm 0.05)\ \text{kHz}, \qquad S_{xx,0}(\Omega_2) \approx 147\,\frac{\text{V}^2}{\text{kHz}}.$$

The linewidths $\gamma_{1,0}$ and $\gamma_{2,0}$ are equal within the margin of error. The amplitude ratio between the two measurements at the central frequencies of particle 1 is $S_{xx,r}(\Omega_1)/S_{xx,0}(\Omega_1) \approx 4.6$ and for particle to its $S_{xx,r}(\Omega_2)/S_{xx,0}(\Omega_2) \approx 0.12$. Comparing this with the theory obtained in Chapter 3.3.2 one could interpret the two linewidths of particle 1 as the two normal modes of the system, where the real part of the eigenfrequencies is degenerate and the imaginary part corresponds to a damping factor. This damping factor would thus increase the linewidth of one of the normal modes while it decreases it for the second one. However, it is unclear why this behaviour is not reproduced for the second particle. If one looks closely at Figure 38b, one can see a small peak on top of the fitted Lorentzian but the peak size is not comparable to Figure 38a. However, the increased amplitude also means that the linear approximation made for the force calculation in Chapter 3.3 is no longer valid, since the condition $|z_1 - z_2| \ll \lambda$ is not satisfied anymore. Therefore, a more extensive theory is needed to fully describe the system dynamics in case of $k_2 \gg k_1$.

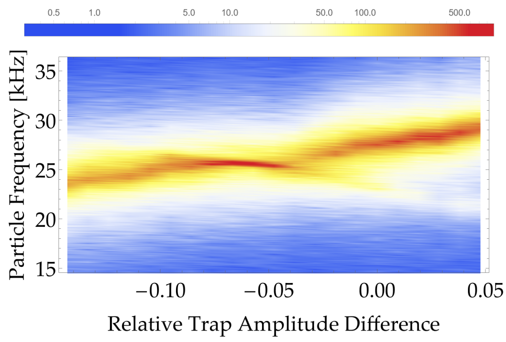

(a) PSD of particle 1 as a function of trap depth.

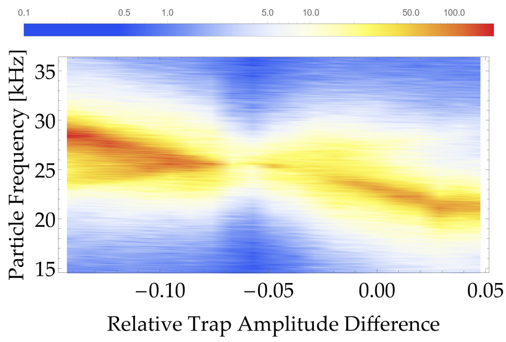

(b) PSD of particle 2 as a function of trap depth.

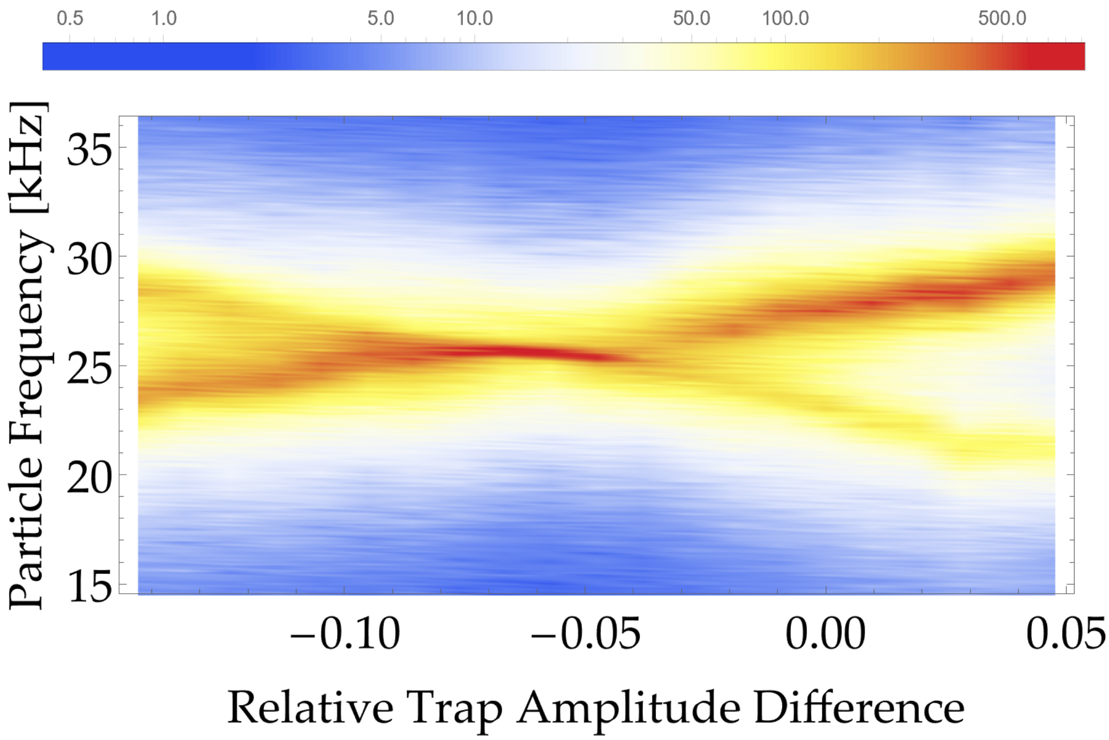

(c) PSD (arbitrary units) of combined detection + fit as a function of trap depth.

Figure 37: PSD (in arbitrary units) of the particles motion as a function of trap amplitude **with non-reciprocal optical interaction** at distance R $\approx 12.7\ \mu$m and pressure p $= 2.2$ mbar. The upper Figures show the individual particle detections and the lower one shows them combined. For each measurement, the trap amplitude was increased for the trap of particle 1 while it was decreased for the trap of particle 2 by the same, constant amount.

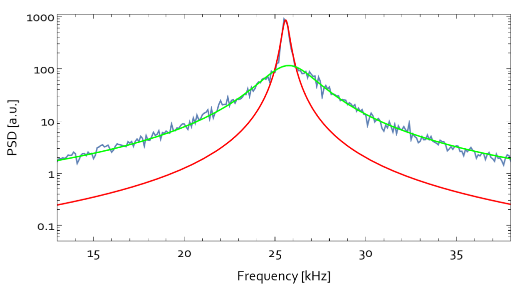

(a) PSD and fits of PSD for particle 1.

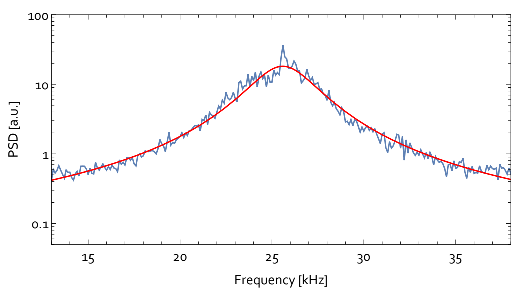

(b) PSD and fit of PSD for particle 2.

Figure 38: Measured and fitted PSD (in arbitrary units) of the particles motion at a point of degenerate eigenfrequencies (η = -0.048). (Left) PSD of particle 1, fitted with two different Lorentzians. (Right) PSD of particles 1, fitted with one Lorentzian.

6 Conclusion and Outlook

We have theoretically described the optical interaction between nanoparticles significantly smaller than the laser wavelength (Rayleigh regime) trapped in distinct optical tweezers. We assume a fully tunable system, where we are able to change the optical phases as well as the interparticle distance. For the special case of far-field inter-particle distances as well as small motional amplitudes with respect to the wavelength, we set up the linear equations of motion of the coupled system and analyzed them for different system parameters. We are able to recover the simple optical binding dynamics [7], as well as non-conservative coupling rates for certain system parameters. The main contribution of the non-reciprocal forces along the particle connection axis (x-axis) decreases with $1/R$ and stems from the distance change between them due to their oscillations along their connection axis, which creates a non-reciprocal force between the two oscillators if the phase difference in their respective traps is non-zero. The main contribution along the optical axis (z-axis) however, comes from the phase change along the optical axis inside a focused Gaussian beam, causing this force to also be proportional to $1/R$ if one takes into account the particles oscillations in z-direction.

We built and characterized the experimental setup for trapping arrays of levitated nanoparticles. We tune the coupling by changing the distance between the particles, the phase difference and the angle of polarization between the two traps which allows us to tune not only the strength of the interaction but also the type between conservative to non-conservative. Conservative coupling of $g/\Omega = 0.033 \pm 0.002$ at a pressure of 2.2 mbar and inter-particle distance $R \approx 13\,\mu$m has been shown. For a different measurement at distance $R \approx 12.7\,\mu$m and equal pressure, we demonstrate the dominant non-conservative coupling rates. However, the linearized theory developed in the scope of this thesis fails to fully describe the system dynamics in case of strong non-conservative interaction, which increases the system energy and thus the particles motional amplitude. This not only changes the form of the non-conservative force acting on the particles but also causes the particles to explore parts of the trapping potential that are not described well by a harmonic oscillator anymore. The nonlinearities present in the system however, could lead to enhanced sensing performances [47, 48] which can be used on the search of new forces going beyond the standard model [49].

Furthermore, optically interacting nanoparticles could be used to study collective optomechanical effects such as phononic metamaterials or the investigation of topological phases [50, 51] as well as probing the validity of local and global master equations in the strong and ultra-strong coupling regime [52]. Turning off the optical interaction might allow for the probing of and entanglement via other, short-range forces, such as Coulumb or Casimir-Polder interaction [39].

The setup also allows for probing of various effects arising from the particles interaction that have not been explored in this thesis, like the engineering of (non)-reciprocal phonon transport between the two particles by detuning their scattered light by their frequency of oscillation and creating resonant Rabi-oscillations in their energy. [35, 53].

References

[1] Markus Aspelmeyer, Tobias J. Kippenberg, and Florian Marquardt. "Cavity optomechanics". In: *Rev. Mod. Phys.* 86 (4 Dec. 2014), pp. 1391–1452. DOI: 10.1103/RevModPhys.86.1391. URL: https://link.aps.org/doi/10.1103/RevModPhys.86.1391.

[2] Uroš Delić et al. "Cooling of a levitated nanoparticle to the motional quantum ground state". In: *Science* 367.6480 (Feb. 2020), pp. 892–895. DOI: 10.1126/science.aba3993. URL: https://doi.org/10.1126%5C%2Fscience.aba3993.

[3] Lorenzo Magrini et al. "Real-time optimal quantum control of mechanical motion at room temperature". In: *Nature* 595.7867 (2021), pp. 373–377. DOI: 10.1038/s41586-021-03602-3. URL: https://doi.org/10.1038/s41586-021-03602-3.

[4] F Tebbenjohanns et al. "Quantum control of a nanoparticle optically levitated in cryogenic free space". In: *Nature* 595 (July 2021), pp. 378–382. DOI: 10.1038/s41586-021-03617-w. URL: https://doi.org/10.1038/s41586-021-03617-w.

[5] Alexandr Jonas and Pavel Zemanek. "Light at work: The use of optical forces for particle manipulation, sorting, and analysis". In: *Electrophoresis* 29 (Feb. 2009), pp. 4813–51. DOI: 10.1002/elps.200800484.

[6] Michael M. Burns, Jean-Marc Fournier, and Jene A. Golovchenko. "Optical binding". In: *Phys. Rev. Lett.* 63 (12 Sept. 1989), pp. 1233–1236. DOI: 10.1103/PhysRevLett.63.1233. URL: https://link.aps.org/doi/10.1103/PhysRevLett.63.1233.

[7] Kishan Dholakia and Pavel Zemánek. "Colloquium: Gripped by light: Optical binding". In: *Rev. Mod. Phys.* 82 (2 June 2010), pp. 1767–1791. DOI: 10.1103/RevModPhys.82.1767. URL: https://link.aps.org/doi/10.1103/RevModPhys.82.1767.

[8] Yoshihiko Arita, Ewan M. Wright, and Kishan Dholakia. "Optical binding of two cooled micro-gyroscopes levitated in vacuum". In: *Optica* 5.8 (Aug. 2018), pp. 910–917. DOI: 10.1364/OPTICA.5.000910. URL: http://opg.optica.org/optica/abstract.cfm?URI=optica-5-8-910.

[9] Michael M. Burns, Jean-Marc Fournier, and Jene A. Golovchenko. "Optical Matter: Crystallization and Binding in Intense Optical Fields". In: *Science* 249.4970 (1990), pp. 749–754. DOI: 10.1126/science.249.4970.749. eprint: https://www.science.org/doi/pdf/10.1126/science.249.4970.749. URL: https://www.science.org/doi/abs/10.1126/science.249.4970.749.

[10] F Dapasse and J -M Vigoureux. "Optical binding force between two Rayleigh particles". In: *Journal of Physics D: Applied Physics* 27.5 (May 1994), pp. 914–919. DOI: 10.1088/0022-3727/27/5/006. URL: https://doi.org/10.1088/0022-3727/27/5/006.

[11] Kayn A. Forbes, David S. Bradshaw, and David L. Andrews. "Optical binding of nanoparticles". In: *Nanophotonics* 9.1 (2020), pp. 1–17. DOI: doi:10.1515/nanoph-2019-0361. URL: https://doi.org/10.1515/nanoph-2019-0361.

[12] Anna S. Zelenina, Romain Quidant, and Manuel Nieto-Vesperinas. "Enhanced optical forces between coupled resonant metal nanoparticles". In: *Opt. Lett.* 32.9 (May 2007), pp. 1156–1158. DOI: 10.1364/OL.32.001156. URL: http://opg.optica.org/ol/abstract.cfm?URI=ol-32-9-1156.

[13] Vassili Demergis and Ernst-Ludwig Florin. "Ultrastrong Optical Binding of Metallic Nanoparticles". In: *Nano Letters* 12.11 (2012). PMID: 23035835, pp. 5756–5760. DOI: 10.1021/nl303035p. eprint: https://doi.org/10.1021/nl303035p. URL: https://doi.org/10.1021/nl303035p.

[14] Fan Nan et al. "Dissipative Self-Assembly of Anisotropic Nanoparticle Chains with Combined Electrodynamic and Electrostatic Interactions". In: *Advanced Materials* 30.45 (), p. 1803238. DOI: https://doi.org/10.1002/adma.201803238. eprint: https://onlinelibrary.wiley.com/doi/pdf/10.1002/adma.201803238. URL: https://onlinelibrary.wiley.com/doi/abs/10.1002/adma.201803238.

[15] A. Ashkin. "Acceleration and Trapping of Particles by Radiation Pressure". In: *Phys. Rev. Lett.* 24 (4 Jan. 1970), pp. 156–159. DOI: 10.1103/PhysRevLett.24.156. URL: https://link.aps.org/doi/10.1103/PhysRevLett.24.156.

[16] J. E. Bjorkholm et al. "Observation of Focusing of Neutral Atoms by the Dipole Forces of Resonance-Radiation Pressure". In: *Phys. Rev. Lett.* 41 (20 Nov. 1978), pp. 1361–1364. DOI: 10.1103/PhysRevLett.41.1361. URL: https://link.aps.org/doi/10.1103/PhysRevLett.41.1361.

[17] W. H. Wright, G. J. Sonek, and M. W. Berns. "Parametric study of the forces on microspheres held by optical tweezers". In: *Appl. Opt.* 33.9 (Mar. 1994), pp. 1735–1748. DOI: 10.1364/AO.33.001735. URL: http://opg.optica.org/ao/abstract.cfm?URI=ao-33-9-1735.

[18] K Svoboda and S M Block. "Biological Applications of Optical Forces". In: *Annual Review of Biophysics and Biomolecular Structure* 23.1 (1994). PMID: 7919782, pp. 247–285. DOI: 10.1146/annurev.bb.23.060194.001335. URL: https://doi.org/10.1146/annurev.bb.23.060194.001335.

[19] A. Ashkin. "Forces of a single-beam gradient laser trap on a dielectric sphere in the ray optics regime". In: *Biophysical Journal* 61.2 (1992), pp. 569–582. ISSN: 0006-3495. DOI: https://doi.org/10.1016/S0006-3495(92)81860-X. URL: https://www.sciencedirect.com/science/article/pii/S000634959281860X.

[20] Lukas Novotny and Bert Hecht. *Principles of Nano-Optics*. 2nd ed. Cambridge University Press, 2012. DOI: 10.1017/CBO9780511794193.

[21] Yasuhiro Harada and Toshimitsu Asakura. "Radiation forces on a dielectric sphere in the Rayleigh scattering regime". In: *Optics Communications* 124.5 (1996), pp. 529–541. ISSN: 0030-4018. DOI: https://doi.org/10.1016/0030-4018(95)00753-9. URL: https://www.sciencedirect.com/science/article/pii/0030401895007539.

[22] E. Wolf and Dennis Gabor. "Electromagnetic diffraction in optical systems - I. An integral representation of the image field". In: *Proceedings of the Royal Society of London. Series A. Mathematical and Physical Sciences* 253.1274 (1959), pp. 349–357. DOI: 10.1098/rspa.1959.0199. eprint: https://royalsocietypublishing.org/doi/pdf/10.1098/rspa.1959.0199. URL: https://royalsocietypublishing.org/doi/abs/10.1098/rspa.1959.0199.

[23] B. Richards, E. Wolf, and Dennis Gabor. "Electromagnetic diffraction in optical systems, II. Structure of the image field in an aplanatic system". In: *Proceedings of the Royal Society of London. Series A. Mathematical and Physical Sciences* 253.1274 (1959), pp. 358–379. DOI: 10.1098/rspa.1959.0200. eprint: https://royalsocietypublishing.org/doi/pdf/10.1098/rspa.1959.0200. URL: https://royalsocietypublishing.org/doi/abs/10.1098/rspa.1959.0200.

[24] T.A Nieminen, H Rubinsztein-Dunlop, and N.R Heckenberg. “Multipole expansion of strongly focused laser beams”. In: *Journal of Quantitative Spectroscopy and Radiative Transfer* 79-80 (June 2003), pp. 1005–1017. ISSN: 0022-4073. DOI: 10.1016/s0022-4073(02)00335-7. URL: http://dx.doi.org/10.1016/S0022-4073(02)00335-7.

[25] Jan Gieseler. “Dynamics of optically levitated nanoparticles in high vacuum”. PhD thesis. UPC, Institut de Ciències Fotòniques, Feb. 2014. URL: http://hdl.handle.net/2117/95281.

[26] Max Born and Emil Wolf. *Principles of Optics: 60th Anniversary Edition.* 7th ed. Cambridge University Press, 2019. DOI: 10.1017/9781108769914.

[27] Kirstine Berg-Sørensen and Henrik Flyvbjerg. “Power spectrum analysis for optical tweezers”. In: *Review of Scientific Instruments* 75.3 (2004), pp. 594–612. DOI: 10.1063/1.1645654. eprint: https://doi.org/10.1063/1.1645654. URL: https://doi.org/10.1063/1.1645654.

[28] B.D. Hauer, J. Maciejko, and J.P. Davis. “Nonlinear power spectral densities for the harmonic oscillator”. In: *Annals of Physics* 361 (Oct. 2015), pp. 148–183. ISSN: 0003-4916. DOI: 10.1016/j.aop.2015.05.031. URL: http://dx.doi.org/10.1016/j.aop.2015.05.031.

[29] Fernando Monteiro et al. “Force and acceleration sensing with optically levitated nanogram masses at microkelvin temperatures”. In: *Physical Review A* 101.5 (May 2020). DOI: 10.1103/physreva.101.053835. URL: https://doi.org/10.1103%5C%2Fphysreva.101.053835.

[30] M Brunelli et al. “Out-of-equilibrium thermodynamics of quantum optomechanical systems”. In: *New Journal of Physics* 17.3 (Mar. 2015), p. 035016. DOI: 10.1088/1367-2630/17/3/035016. URL: https://doi.org/10.1088%5C%2F1367-2630%5C%2F17%5C%2F3%5C%2F035016.

[31] Mario A. Ciampini et al. *Experimental nonequilibrium memory erasure beyond Landauer's bound.* 2021. DOI: 10.48550/ARXIV.2107.04429. URL: https://arxiv.org/abs/2107.04429.

[32] Alireza Seif et al. “Thermal management and non-reciprocal control of phonon flow via optomechanics”. In: *Nature communications* 9 (Mar. 2018). DOI: 10.1038/s41467-018-03624-y.

[33] Abhishodh Prakash, J. H. Pixley, and Manas Kulkarni. “Universal spectral form factor for many-body localization”. In: *Phys. Rev. Research* 3 (1 Feb. 2021), p. L012019. DOI: 10.1103/PhysRevResearch.3.L012019. URL: https://link.aps.org/doi/10.1103/PhysRevResearch.3.L012019.

[34] Henning Rudolph et al. *Force-gradient sensing and entanglement via feedback cooling of interacting nanoparticles.* 2022. DOI: 10.48550/ARXIV.2204.13684. URL: https://arxiv.org/abs/2204.13684.

[35] A. B. Shkarin et al. “Optically Mediated Hybridization between Two Mechanical Modes”. In: *Physical Review Letters* 112.1 (Jan. 2014). ISSN: 1079-7114. DOI: 10.1103/physrevlett.112.013602. URL: http://dx.doi.org/10.1103/PhysRevLett.112.013602.

[36] Gilles Dolfo and Jacques Vigué. “Damping of coupled harmonic oscillators”. In: *European Journal of Physics* 39.2 (Feb. 2018), p. 025005. DOI: 10.1088/1361-6404/aa9ec6. URL: https://doi.org/10.1088/1361-6404/aa9ec6.

[37] Lukas Novotny. "Strong coupling, energy splitting, and level crossings: A classical perspective". In: *American Journal of Physics* 78.11 (2010), pp. 1199–1202. DOI: 10.1119/1.3471177. eprint: https://doi.org/10.1119/1.3471177. URL: https://doi.org/10.1119/1.3471177.

[38] Martin Frimmer et al. "Controlling the net charge on a nanoparticle optically levitated in vacuum". In: *Phys. Rev. A* 95 (6 June 2017), p. 061801. DOI: 10.1103/PhysRevA.95.061801. URL: https://link.aps.org/doi/10.1103/PhysRevA.95.061801.

[39] T. Weiss et al. "Large Quantum Delocalization of a Levitated Nanoparticle Using Optimal Control: Applications for Force Sensing and Entangling via Weak Forces". In: *Phys. Rev. Lett.* 127 (2 July 2021), p. 023601. DOI: 10.1103/PhysRevLett.127.023601. URL: https://link.aps.org/doi/10.1103/PhysRevLett.127.023601.

[40] Yoshihiko Arita, Ewan M. Wright, and Kishan Dholakia. "Optical binding of two cooled micro-gyroscopes levitated in vacuum". In: *Optica* 5.8 (Aug. 2018), pp. 910–917. DOI: 10.1364/OPTICA.5.000910. URL: http://opg.optica.org/optica/abstract.cfm?URI=optica-5-8-910.

[41] Tomáš Čižmár et al. "Multiple optical trapping and binding: New routes to self-assembly". In: *Journal of Physics B: Atomic, Molecular and Optical Physics* 43 (Apr. 2010), p. 102001. DOI: 10.1088/0953-4075/43/10/102001.

[42] Guillaume Gauthier et al. "Dynamic high-resolution optical trapping of ultracold atoms". In: *Advances In Atomic, Molecular, and Optical Physics*. Elsevier, 2021, pp. 1–101. DOI: 10.1016/bs.aamop.2021.04.001. URL: https://doi.org/10.1016%5C%2Fbs.aamop.2021.04.001.

[43] "Quantum Noise: Basic Measurements and Techniques". In: *A Guide to Experiments in Quantum Optics*. John Wiley & Sons, Ltd, 2004. Chap. 8, pp. 200–231. ISBN: 9783527619238. DOI: https://doi.org/10.1002/9783527619238.ch8. eprint: https://onlinelibrary.wiley.com/doi/pdf/10.1002/9783527619238.ch8. URL: https://onlinelibrary.wiley.com/doi/abs/10.1002/9783527619238.ch8.

[44] Felix Tebbenjohanns, Martin Frimmer, and Lukas Novotny. "Optimal position detection of a dipolar scatterer in a focused field". In: *Physical Review A* 100.4 (Oct. 2019). DOI: 10.1103/physreva.100.043821. URL: https://doi.org/10.1103%5C%2Fphysreva.100.043821.

[45] M. Minsky. "Memoir on inventing the confocal scanning microscope". In: *Scanning* 10.4 (1988), pp. 128–138. DOI: https://doi.org/10.1002/sca.4950100403. eprint: https://onlinelibrary.wiley.com/doi/pdf/10.1002/sca.4950100403. URL: https://onlinelibrary.wiley.com/doi/abs/10.1002/sca.4950100403.

[46] Yu Wang et al. "Reduction of laser intensity noise over 1 MHz band for single atom trapping". In: *Opt. Express* 28.21 (Oct. 2020), pp. 31209–31215. DOI: 10.1364/OE.405002. URL: http://opg.optica.org/oe/abstract.cfm?URI=oe-28-21-31209.

[47] Alexander McDonald and Aashish A. Clerk. "Exponentially-enhanced quantum sensing with non-Hermitian lattice dynamics". In: *Nature Communications* 11.1 (Oct. 2020). DOI: 10.1038/s41467-020-19090-4. URL: https://doi.org/10.1038%5C%2Fs41467-020-19090-4.

[48] Tomás Manzaneque et al. *Resolution Limits of Resonant Sensors with Duffing Non-Linearity.* 2022. DOI: 10.48550/ARXIV.2205.11903. URL: https://arxiv.org/abs/2205.11903.

[49] David C Moore and Andrew A Geraci. “Searching for new physics using optically levitated sensors”. In: *Quantum Science and Technology* 6.1 (Jan. 2021), p. 014008. DOI: 10.1088/2058-9565/abcf8a. URL: https://doi.org/10.1088%5C%2F2058-9565%2Fabcf8a.

[50] V. Peano et al. “Topological Phases of Sound and Light”. In: *Physical Review X* 5.3 (July 2015). DOI: 10.1103/physrevx.5.031011. URL: https://doi.org/10.1103%5C%2Fphysrevx.5.031011.

[51] Sebastian D. Huber. “Topological mechanics”. In: *Nature Physics* 12 (July 2016), pp. 621–623. DOI: 10.1038/nphys3801. URL: https://doi.org/10.1038/nphys3801.

[52] Michael Konopik and Eric Lutz. “Local master equations may fail to describe dissipative critical behavior”. In: *Physical Review Research* 4.1 (Mar. 2022). DOI: 10.1103/physrevresearch.4.013171. URL: https://doi.org/10.1103%5C%2Fphysrevresearch.4.013171.

[53] Shengyan Liu, Zhang-qi Yin, and Tongcang Li. “Prethermalization and Nonreciprocal Phonon Transport in a Levitated Optomechanical Array”. In: *Advanced Quantum Technologies* 3.3 (Jan. 2020), p. 1900099. DOI: 10.1002/qute.201900099. URL: https://doi.org/10.1002%2Fqute.201900099.

[54] Jakob Rieser et al. *Observation of strong and tunable light-induced dipole-dipole interactions between optically levitated nanoparticles.* 2022. DOI: 10.48550/ARXIV.2203.04198. URL: https://arxiv.org/abs/2203.04198.

Appendix A.1: Force between two levitated dipoles

Putting particle 2 into the coordinate origin, we'll use the following definitions:

$$\boldsymbol{R} = \boldsymbol{r}_1 - \boldsymbol{r}_2 = -\boldsymbol{r}_1 = (R\sin(\varphi)\sin(\theta),\ R\cos(\varphi)\sin(\theta),\ R\cos(\theta)), \qquad R = \sqrt{x^2+y^2+z^2}, \tag{115}$$

$$\boldsymbol{\varphi} = (\cos(\varphi), -\sin(\varphi),\ 0), \qquad \varphi = \arctan\left(\frac{x}{y}\right), \tag{116}$$

$$\boldsymbol{\theta} = (\sin(\varphi)\cos(\theta), \cos(\varphi)\cos(\theta), -\sin(\theta), \qquad \theta = \arccos\left(\frac{z}{r}\right). \tag{117}$$

The incident field is a Gaussian beam propagating in z-direction of the form:

$$\boldsymbol{E}^{I_1} = E_{0,1}\boldsymbol{e}_y e^{i(\omega t+(k-1/z_0)z)}, \qquad \boldsymbol{E}^{I_2} = E_{0,2}\boldsymbol{e}_y e^{i(\omega t+(k-1/z_0)z+\phi_0)},$$

where $\boldsymbol{k} = k\boldsymbol{e}_z$, $E_{0,i}$ are the local fields amplitudes and $\phi_0 = \phi_{2,0} - \phi_{1,0}$ is the phase difference between the two incident fields at the focus.
The total force acting on dipole 1 is

$$\begin{aligned}\langle F_i(\boldsymbol{r}_1)\rangle = \frac{1}{2}\mathrm{Re}\left\{d_j^*\partial_i E_j(\boldsymbol{r_1})\right\} = \frac{1}{2}\mathrm{Re}\Big\{ &\underbrace{\alpha^* E_j^{I_1*}(\boldsymbol{r}_1)\partial_i^1 E_j^{I_1}(\boldsymbol{r}_1)}_{F_i^{OP}} + \underbrace{(\alpha^*)^2 G_{jk}^* E_k^{I_2*}(\boldsymbol{r}_2)\partial_i^1 E_j^{I_1}(\boldsymbol{r}_1)}_{F_i^{int,1}} \\ &+ \underbrace{|\alpha|^2 E_j^{I_1*}(\boldsymbol{r}_1)\partial_i^1(G_{jk})E_k^{I_2}(\boldsymbol{r}_2)}_{F_i^{int,2}}\Big\},\end{aligned} \tag{118}$$

with

$$G_{ij}(R) = \frac{1}{4\pi\varepsilon_0\varepsilon_m R^3}e^{ikR}\left[\left(3-3ikR-k^2R^2\right)\frac{R_iR_j}{R^2} + (k^2R^2+ikR-1)\delta_{ij}\right]. \tag{119}$$

Since the leading order of the gradient acting on the electric field in eq. 118 comes from the derivative of the exponential function of the greens tensor as well as the phase of the incident fields [54], we will in the following assume the field amplitudes $E_{0,i}$ to be constant in this calculations. Note that this yields the right result for the force in z-direction in the far-field but only accounts for a plane wave potential orthogonal to the optical axis. However, the extension to a Gaussian potential is straight forward by changing the electric field amplitude to that of eq. 1 and calculating the edditional force term in $F_{x,y}^{int,1}$, corresponding to a gradient force. Lets start with the Force in $z-$direction. The abbreviation $k - 1/z_0 = \tilde{k}$ has been used in the following calculations, as well as the relation $\phi \approx (k-1/z_0)(z_2-z_1)+\phi_0$.

$$\langle F_z^{OP}(\boldsymbol{r}_1)\rangle = \frac{1}{2}\mathrm{Re}\left\{\alpha^*|E_{0,1}|^2\tilde{k}\right\} = \frac{1}{2}\tilde{k}\alpha''|E_{0,1}|^2, \tag{120}$$

$$\begin{aligned}
\langle F_z^{int,1}(\boldsymbol{r}_1)\rangle &= \frac{1}{2}\mathrm{Re}\left\{(\alpha^*)^2E_{0,1}E_{0,2}i\tilde{k}G^*_{yy}e^{-i\phi}\right\}\\
&= \frac{1}{2}\mathrm{Re}\left\{\frac{(\alpha^*)^2\tilde{k}E_{0,1}E_{0,2}e^{-i(kR+\phi)}}{4\pi\varepsilon_0\varepsilon_m R^3}\left[\left(3i-3kR-ik^2R^2\right)\cos^2(\varphi)\sin^2(\theta)+ik^2R^2+kR-i\right]\right\}\\
&= \frac{E_{0,1}E_{0,2}\tilde{k}}{8\pi\varepsilon_0\varepsilon_m R^3}\mathrm{Re}\Big\{(\alpha'^2-\alpha''^2-2i\alpha'\alpha'')(\cos(kR+\phi)-i\sin(kR+\phi))\\
&\cdot\left[\left(3i-3kR-ik^2R^2\right)\cos^2(\varphi)\sin^2(\theta)+ik^2R^2+kR-i\right]\Big\}\\
&= \frac{E_{0,1}E_{0,2}\tilde{k}}{8\pi\varepsilon_0\varepsilon_m R^3}\Big[\left(kR-3kR\cos^2(\varphi)\sin^2(\theta)\right)\left(\left(\alpha'^2-\alpha''^2\right)\cos(kR+\phi)-2\alpha'\alpha''\sin(kR+\phi)\right)\\
&+\left(\left(3-k^2R^2\right)\cos^2(\varphi)\sin^2(\theta)+k^2R^2-1\right)\left(2\alpha'\alpha''\cos(kR+\phi)+\left(\alpha'^2-\alpha''^2\right)\sin(kR+\phi)\right)\Big]\\
&\approx \frac{E_{0,1}E_{0,2}}{8\pi\varepsilon_0\varepsilon_m R}\left[\tilde{k}k^2\left(1-\cos^2(\varphi)\sin^2(\theta)\right)\left(2\alpha'\alpha''\cos(kR+\phi)+\left(\alpha'^2-\alpha''^2\right)\sin(kR+\phi)\right)\right],
\end{aligned}\tag{121}$$

$$\begin{aligned}
\langle F_z^{int,2}(\boldsymbol{r}_1)\rangle &= \frac{1}{2}\mathrm{Re}\left\{|\alpha|^2E_{0,1}E_{0,2}e^{i\phi}\partial_z^1(G_{yy})\right\}\\
&= \frac{1}{2}\mathrm{Re}\left\{\frac{|\alpha|^2E_{0,1}E_{0,2}}{4\pi\varepsilon_0\varepsilon_m}e^{i\phi}\partial_z\left[\frac{e^{ikR}}{R^3}\left[\left(3-3ikR-k^2R^2\right)\frac{y^2}{R^2}+k^2R^2+ikR-1\right]\right]\right\}\\
&= \frac{1}{2}\mathrm{Re}\Bigg\{\frac{|\alpha|^2E_{0,1}E_{0,2}}{4\pi\varepsilon_0\varepsilon_m}e^{i(kR+\phi)}\cdot\Bigg[\left(\frac{ikz}{R^4}-\frac{3z}{R^5}\right)\cdot\left[\left(3-3ikR-k^2R^2\right)\frac{y^2}{R^2}+k^2R^2+ikR-1\right]\\
&-\frac{2zy^2}{R^7}\left(3-3ikR-k^2R^2\right)+\frac{1}{R^3}\left[\left(-\frac{3izk}{R}-2zk^2\right)\frac{y^2}{R^2}+2zk^2+\frac{izk}{R}\right]\Bigg]\Bigg\}\\
&= \frac{|\alpha|^2E_{0,1}E_{0,2}}{8\pi\varepsilon_0\varepsilon_m}\Bigg[\cos(kR+\phi)\left(-\frac{2zk^2}{R^3}+\frac{3z(2k^2y^2-1)}{R^5}+\frac{3zy^2(zk^2-5)}{R^7}\right)\\
&+\sin(kR+\phi)\left(-\frac{zk^3}{R^2}+\frac{zy^2k^3}{R^4}-\frac{6zy^2k}{R^6}\right)\\
&= \frac{|\alpha|^2E_{0,1}E_{0,2}}{8\pi\varepsilon_0\varepsilon_m}\Bigg[\cos(kR+\phi)\left(-\frac{2\cos(\theta)k^2}{R^2}-\frac{3\cos(\theta)\left(1-\cos^2(\varphi)\sin^2(\theta)(2k^2R^2+\cos(\theta)-5)\right)}{R^4}\right)\\
&+\sin(kR+\phi)\left(-\frac{\cos(\theta)k^3}{R}+\frac{\cos(\theta)\cos^2(\varphi)\sin^2(\theta)k^3}{R}-\frac{6\cos(\theta)\cos^2(\varphi)\sin^2(\theta)k}{R^3}\right)\\
&\approx \frac{|\alpha|^2E_{0,1}E_{0,2}k^2}{8\pi\varepsilon_0\varepsilon_m R}\cos(\theta)k\sin(kR+\phi)\left(\cos^2(\varphi)\sin^2(\theta)-1\right).
\end{aligned}\tag{122}$$

In the last line of $\langle F_z^{int,1}(\boldsymbol{r}_1)\rangle$ and $\langle F_z^{int,2}(\boldsymbol{r}_1)\rangle$ all terms of order $\mathcal{O}\left(\frac{1}{R^2}\right)$ have been neglected

due to the far-field limit.
The optical force F^{OP} as well as $F^{int,1}$ in x- and y-direction are zero, since the derivative of E^I is only non-zero in z-direction. Hence, the only force left to calculate is $F^{int,2}$:

$$
\begin{aligned}
\langle F_x^{int,2}(\boldsymbol{r}_1)\rangle &= \frac{1}{2}\mathrm{Re}\left\{|\alpha|^2 E_{0,1}E_{0,2}e^{i\phi}\partial_x G_{yy}\right\}\\
&= \frac{1}{2}\mathrm{Re}\left\{\frac{|\alpha|^2 E_{0,1}E_{0,2}}{4\pi\varepsilon_0\varepsilon_m}e^{i\phi}\partial_x\left[\frac{e^{ikR}}{R^3}\left[\left(3-3ikR-k^2R^2\right)\frac{y^2}{R^2}+k^2R^2+ikR-1\right]\right]\right\}\\
&= \frac{1}{2}\mathrm{Re}\Bigg\{\frac{|\alpha|^2 E_{0,1}E_{0,2}}{4\pi\varepsilon_0\varepsilon_m}e^{i(kR+\phi)}\cdot\Bigg[\left(\frac{ikx}{R^4}-\frac{3x}{R^5}\right)\cdot\left[\left(3-3ikR-k^2R^2\right)\frac{y^2}{R^2}+k^2R^2+ikR-1\right]\\
&-\frac{2xy^2}{R^7}\left(3-3ikR-k^2R^2\right)+\frac{1}{R^3}\left[\left(-\frac{3ixk}{R}-2xk^2\right)\frac{y^2}{R^2}+2xk^2+\frac{ixk}{R}\right]\Bigg]\Bigg\}\\
&= \frac{|\alpha|^2 E_{0,1}E_{0,2}}{8\pi\varepsilon_0\varepsilon_m}\Bigg[\cos(kR+\phi)\left(-\frac{2xk^2}{R^3}+\frac{3x(2k^2y^2-1)}{R^5}+\frac{3xy^2(xk^2-5)}{R^7}\right)\\
&+\sin(kR+\phi)\left(-\frac{xk^3}{R^2}+\frac{xy^2k^3}{R^4}-\frac{6xy^2k}{R^6}\right)\\
&= \frac{|\alpha|^2 E_{0,1}E_{0,2}}{8\pi\varepsilon_0\varepsilon_m}\Bigg[\cos(kR+\phi)\Bigg(-\frac{2\sin(\varphi)\sin(\theta)k^2}{R^2}\\
&-\frac{3\sin(\varphi)\sin(\theta)\left(1-\cos^2(\varphi)\sin^2(\theta)(2k^2R^2+R\sin(\varphi)\sin(\theta)-5)\right)}{R^4}\Bigg)\\
&+\sin(kR+\phi)\left(-\frac{\sin(\varphi)\sin(\theta)k^3}{R}+\frac{\sin(\varphi)\sin(\theta)\cos^2(\varphi)\sin^3(\theta)k^3}{R}-\frac{6\sin(\varphi)\sin(\theta)\cos^2(\varphi)\sin^2(\theta)k}{R^3}\right)\\
&\approx \frac{|\alpha|^2 E_{0,1}E_{0,2}k^2}{8\pi\varepsilon_0\varepsilon_m R}\sin(\varphi)\sin(\theta)\Bigg[k\sin(kR+\phi)\left(\cos^2(\varphi)\sin^2(\theta)-1\right)\\
&+\frac{2}{R}\cos(kR+\phi)\left(3\cos^2(\varphi)\sin^2(\theta)-1\right)\Bigg],
\end{aligned}
\tag{123}
$$

$$
\begin{aligned}
\langle F_y^{int,2}(\boldsymbol{r}_1)\rangle &= \frac{1}{2}\mathrm{Re}\left\{|\alpha|^2 E_{0,1}E_{0,2}e^{i\phi}\partial_y G_{yy}\right\} \\
&= \frac{1}{2}\mathrm{Re}\left\{\frac{|\alpha|^2 E_{0,1}E_{0,2}}{4\pi\varepsilon_0\varepsilon_m}e^{i\phi}\partial_y\left[\frac{e^{ikR}}{R^3}\left[\left(3-3ikR-k^2R^2\right)\frac{y^2}{R^2}+k^2R^2+ikR-1\right]\right]\right\} \\
&= \frac{1}{2}\mathrm{Re}\Bigg\{\frac{|\alpha|^2 E_{0,1}E_{0,2}}{4\pi\varepsilon_0\varepsilon_m}e^{i(kR+\phi)}\cdot\Bigg[\left(\frac{iky}{R^4}-\frac{3y}{R^5}\right)\cdot\left[\left(3-3ikR-k^2R^2\right)\frac{y^2}{R^2}+k^2R^2+ikR-1\right] \\
&+\left(\frac{2y}{R^5}-\frac{2y^3}{R^7}\right)\left(3-3ikR-k^2R^2\right)+\frac{1}{R^3}\left[\left(-\frac{3iyk}{R}-2yk^2\right)\frac{y^2}{R^2}+2yk^2+\frac{iyk}{R}\right]\Bigg]\Bigg\} \\
&= \frac{|\alpha|^2 E_{0,1}E_{0,2}}{8\pi\varepsilon_0\varepsilon_m}\Bigg[\cos(kR+\phi)\left(-\frac{4yk^2}{R^3}+\frac{3y(2k^2y^2+1)}{R^5}+\frac{3y^3(yk^2-5)}{R^7}\right) \\
&+\sin(kR+\phi)\left(-\frac{yk^3}{R^2}+\frac{yk(y^2k^2+6)}{R^4}-\frac{6y^3k}{R^6}\right) \\
&= \frac{|\alpha|^2 E_{0,1}E_{0,2}}{8\pi\varepsilon_0\varepsilon_m}\Bigg[\cos(kR+\phi)\Bigg(-\frac{4\cos(\varphi)\sin(\theta)k^2}{R^2} \\
&+\frac{3\cos(\varphi)\sin(\theta)(R\cos^3(\varphi)\sin^3(\theta)k^2+1+\cos^2(\varphi)\sin^2(\theta)(2k^2R^2-5))}{R^4}\Bigg) \\
&+\sin(kR+\phi)\left(-\frac{\cos(\varphi)\sin(\theta)k^3}{R}+\frac{\cos(\varphi)\sin(\theta)k(R^2\cos^2(\varphi)\sin^2(\theta)k^2-6\cos^2(\varphi)\sin^2(\theta)+6)}{R^3}\right) \\
&\approx \frac{|\alpha|^2 E_{0,1}E_{0,2}k^2}{8\pi\varepsilon_0\varepsilon_m R}\cos(\varphi)\sin(\theta)\Bigg[k\sin(kR+\phi)\left(\cos^2(\varphi)\sin^2(\theta)-1\right) \\
&+\frac{2}{R}\cos(kR+\phi)\left(3\cos^2(\varphi)\sin^2(\theta)-2\right)\Bigg].
\end{aligned}
\tag{124}
$$

In eq. 123 and eq. 124 terms of the order $\mathcal{O}\left(\frac{1}{R^3}\right)$ have been neglected. In order to have a more intuitive understanding of the forces involved, one can now change to polar coordinates, using eq. 115 and eq. 116 and for simplicity assuming $\theta = 0$, meaning that the particles are positioned somewhere in the $x-y$ plane, orthogonal to the optical axis:

$$
\langle F_r(\boldsymbol{r}_1)\rangle = \langle F_x(\boldsymbol{r}_1)\rangle\sin(\varphi)+\langle F_y(\boldsymbol{r}_1)\rangle\cos(\varphi),
\tag{125}
$$

$$
\langle F_\varphi(\boldsymbol{r}_1)\rangle = \langle F_x(\boldsymbol{r}_1)\rangle\cos(\varphi)-\langle F_y(\boldsymbol{r}_1)\rangle\sin(\varphi).
\tag{126}
$$

This then results in a radial force of the form $\langle F_r(\boldsymbol{r}_1)\rangle$

$$
\begin{aligned}
\langle F_r(\boldsymbol{r}_1)\rangle &= \frac{|\alpha|^2 E_{0,1}E_{0,2}k^2}{8\pi\varepsilon_0\varepsilon_m R}\Bigg[\sin^2(\varphi)\left(k\sin(kR+\phi)\left(\cos^2(\varphi)-1\right)+\frac{2}{R}\cos(kR+\phi)\left(3\cos^2(\varphi)-1\right)\right) \\
&+\cos^2(\varphi)\left(k\sin(kR+\phi)\left(\cos^2(\varphi)-1\right)+\frac{2}{R}\cos(kR+\phi)\left(3\cos^2(\varphi)-2\right)\right)\Bigg] \\
&= \frac{|\alpha|^2 E_{0,1}E_{0,2}k^2}{8\pi\varepsilon_0\varepsilon_m R}\left[k\sin(kR+\phi)\left(\cos^2(\varphi)-1\right)+\frac{2}{R}\cos(kR+\phi)\left(2\cos^2(\varphi)-1\right)\right],
\end{aligned}
\tag{127}
$$

and angular force $\langle F_\varphi(\boldsymbol{r}_1)\rangle$

$$\langle F_\varphi(\boldsymbol{r}_1)\rangle = \frac{|\alpha|^2 E_{0,1}E_{0,2}k^2}{8\pi\varepsilon_0\varepsilon_m R}\sin(\varphi)\cos(\varphi)\Big[k\sin(kR+\phi)\left(\cos^2(\varphi)-1\right)$$

$$+\frac{2}{R}\cos(kR+\phi)\left(3\cos^2(\varphi)-1\right) - k\sin(kR+\phi)\left(\cos^2(\varphi)-1\right)$$

$$-\frac{2}{R}\cos(kR+\phi)\left(3\cos^2(\varphi)-2\right)\Big]$$

$$= \frac{|\alpha|^2 E_{0,1}E_{0,2}k^2}{8\pi\varepsilon_0\varepsilon_m R}\sin(\varphi)\cos(\varphi)\frac{2}{R}\cos(kR+\phi)$$

$$= \frac{|\alpha|^2 E_{0,1}E_{0,2}k^2}{8\pi\varepsilon_0\varepsilon_m R^2}\sin(2\varphi)\cos(kR+\phi). \tag{128}$$

In the same manner, the force on particle 2 can be calculated. However, when comparing these two forces one needs to keep in mind that putting particle 1 in the coordinate origin (as is done for $\boldsymbol{F}(\boldsymbol{r}_2)$) changes the sign of the distance vector $\boldsymbol{R} \to -\boldsymbol{R}$ w.r.t $\boldsymbol{F}(\boldsymbol{r}_1)$ as $(\varphi(\boldsymbol{r}_1), \theta(\boldsymbol{r}_1)) = -(\varphi(\boldsymbol{r}_2), \theta(\boldsymbol{r}_2))$. The sign of the phase difference ϕ in the exponential function changes for $\boldsymbol{F}(\boldsymbol{r}_2)$ according to eq. 71. Therefore, one obtains:

$$\langle F_z^{OP}(\boldsymbol{r}_2)\rangle = \frac{1}{2}\mathrm{Re}\left\{\alpha^*|E_{0,2}|^2 i\tilde{k}\right\} = \frac{1}{2}\tilde{k}\alpha''|E_{0,2}|^2, \tag{129}$$

$$\langle F_z^{int,1}(\boldsymbol{r}_2)\rangle = \frac{1}{2}\mathrm{Re}\left\{(\alpha^*)^2 E_{0,2}E_{0,1} i\tilde{k}G_{yy}^* e^{i\phi}\right\}$$

$$\approx \frac{E_{0,1}E_{0,2}}{8\pi\varepsilon_0\varepsilon_m R}\tilde{k}k^2\left(1-\cos^2(\varphi)\sin^2(\theta)\right)\left[2\alpha'\alpha''\cos(kR-\phi) + \left(\alpha'^2 - \alpha''^2\right)\sin(kR-\phi)\right], \tag{130}$$

$$\langle F_z^{int,2}(\boldsymbol{r}_2)\rangle = \frac{1}{2}\mathrm{Re}\left\{|\alpha|^2 E_{0,2}E_{0,1}e^{-i\phi}\partial_z G_{yy}\right\}$$

$$\approx \frac{|\alpha|^2 E_{0,1}E_{0,2}k^2}{8\pi\varepsilon_0\varepsilon_m R}\cos(\theta)\Big[k\sin(kR-\phi)\left(\cos^2(\varphi)\sin^2(\theta)-1\right)$$

$$+\frac{2}{R}\cos(kR-\phi)\left(3\cos^2(\varphi)\sin^2(\theta)-1\right)\Big], \tag{131}$$

$$\langle F_x^{int,2}(\boldsymbol{r}_2)\rangle = \frac{1}{2}\mathrm{Re}\left\{|\alpha|^2 E_{0,2}E_{0,1}e^{-i\phi}\partial_x G_{yy}\right\}$$

$$\approx \frac{|\alpha|^2 E_{0,1}E_{0,2}k^2}{8\pi\varepsilon_0\varepsilon_m R}\sin(\varphi)\left[k\sin(kR-\phi)\left(\cos^2(\varphi)-1\right) + \frac{2}{R}\cos(kR-\phi)\left(3\cos^2(\varphi)-1\right)\right], \tag{132}$$

$$\langle F_y^{int,2}(\boldsymbol{r}_2)\rangle = \frac{1}{2}\mathrm{Re}\left\{|\alpha|^2 E_{0,2}E_{0,1}e^{-i\phi}\partial_y G_{yy}\right\}$$

$$\approx \frac{|\alpha|^2 E_{0,1}E_{0,2}k^2}{8\pi\varepsilon_0\varepsilon_m R}\cos(\varphi)\left[k\sin(kR-\phi)\left(\cos^2(\varphi)-1\right) + \frac{2}{R}\cos(kR-\phi)\left(3\cos^2(\varphi)-2\right)\right]. \tag{133}$$

Leading to radial and azimuthal forces $\langle F_r(\boldsymbol{r}_2)\rangle$, $\langle F_\varphi(\boldsymbol{r}_2)\rangle$:

$$\langle F_r(\boldsymbol{r}_2)\rangle = \frac{|\alpha|^2 E_{0,1}E_{0,2}k^2}{8\pi\varepsilon_0\varepsilon_m R}\left[k\sin(kR-\phi)\left(\cos^2(\varphi)-1\right)+\frac{2}{R}\cos(kR-\phi)\left(2\cos^2(\varphi)-1\right)\right], \quad (134)$$

$$\langle F_\varphi(\boldsymbol{r}_2)\rangle = \frac{|\alpha|^2 E_{0,1}E_{0,2}k^2}{8\pi\varepsilon_0\varepsilon_m R^2}\sin(2\varphi)\cos(kR-\phi). \quad (135)$$

The above equations give a good overview of the contributing system dynamics. However, in order to better understand the behaviour of two coupled nanoparticles trapped in an optical tweezer, lets change to a coordinate system that monitors the relative motion between the two particles if trapped orthogonal to the axis of polarization at some distance R_0 and oscillating around their equilibrium position, such that their distance R can be written as:

$$R = \sqrt{(R_0+x_2-x_1)^2+(y_2-y_1)^2+(z_2-z_1)^2} \qquad \text{with} \qquad R_0 \gg |x_2-x_1|,\ |y_2-y_1|,\ |z_2-z_1|. \quad (136)$$

The force in z-direction approximated to first order for $\pi/2-\theta \ll 1$ then takes the form

$$\langle F_z^{int}(\boldsymbol{r}_1)\rangle \approx \frac{E_{0,1}E_{0,2}k^2}{8\pi\varepsilon_0\varepsilon_m R}\sin^2(\varphi)\Bigg[\left[\tilde{k}\left(2\alpha'\alpha''\cos(kR+\phi)+\left(\alpha'^2-\alpha''^2\right)\sin(kR+\phi)\right)\right]$$
$$-|\alpha|^2\frac{z_1-z_2}{R_0}\left[k\sin(kR+\phi)+\frac{2}{R}\cos(kR+\phi)\right]\Bigg], \quad (137)$$

where $\theta \approx \pi/2-(z_1-z_2)/R_0$ was used (see Figure 8). Neglecting all terms of order $\mathcal{O}(1/R^2)$ as well as assuming that the dissipative part of α is small and hence $\alpha \approx \alpha'$ leaves

$$\langle F_z^{int}(\boldsymbol{r}_1)\rangle \approx \frac{E_{0,1}E_{0,2}\tilde{k}k^2}{8\pi\varepsilon_0\varepsilon_m R}\alpha^2\sin^2(\varphi)\sin(kR+\phi). \quad (138)$$

One can then expand the force acting on each particle around its equilibrium position, which will here be done only for the force in $z-$ direction, since this is the spatial dimension that will be monitored in the experimental part of this thesis. Using

$$R \approx R_0 + \frac{\sqrt{(z_2-z_1)^2}}{R_0} \quad (139)$$

as well as the fact that the phase in an Gaussian beam changes faster than in a planewave (see eq. 4)

$$\phi(z) = \phi_2(z_2)-\phi_1(z_1) \approx \phi_0 + \underbrace{\left(k-\frac{1}{z_0}\right)}_{\tilde{k}}(z_2-z_1), \quad (140)$$

yields up to $\mathcal{O}\left((z_2-z_1)^2\right)$

$$\langle F_z^{int}(\boldsymbol{r}_1)\rangle\Big|_{z_1\approx z_2} \approx \frac{E_{0,1}E_{0,2}k^2\tilde{k}\alpha^2}{8\pi\varepsilon_0\varepsilon_m R_0}\sin^2(\varphi)\left(\sin(kR_0+\phi_0)) + \tilde{k}\cos(kR_0+\phi_0)(z_2-z_1)\right), \tag{141}$$

$$\langle F_z^{int}(\boldsymbol{r}_2)\rangle\Big|_{z_2\approx z_1} \approx \frac{E_{0,1}E_{0,2}k^2\tilde{k}\alpha^2}{8\pi\varepsilon_0\varepsilon_m R_0}\sin^2(\varphi)\left(\sin(kR_0-\phi_0)) + \tilde{k}\cos(kR_0-\phi_0)(z_1-z_2)\right). \tag{142}$$

One obtains a constant displacement term and a term dependent on the distance and phase between the two particles in z-direction. Neglecting the constant force term, the final force acting on each particle due to the optical interaction with the second particle can be separated into a conservative and a non-nonservative force term, taking the form

$$\langle F_z^{int}(\boldsymbol{r}_1)\rangle \approx \frac{E_{0,1}E_{0,2}k^2\tilde{k}^2\alpha^2}{8\pi\varepsilon_0\varepsilon_m R_0}\sin^2(\varphi)\left(\cos(kR_0)\cos(\phi_0) - \sin(kR_0)\sin(\phi_0)\right)(z_2-z_1), \tag{143}$$

$$\langle F_z^{int}(\boldsymbol{r}_2)\rangle \approx \frac{E_{0,1}E_{0,2}k^2\tilde{k}^2\alpha^2}{8\pi\varepsilon_0\varepsilon_m R_0}\sin^2(\varphi)\left(\cos(kR_0)\cos(\phi_0) + \sin(kR_0)\sin(\phi_0)\right)(z_1-z_2). \tag{144}$$